Quantum Interface between an Atom and a Photon

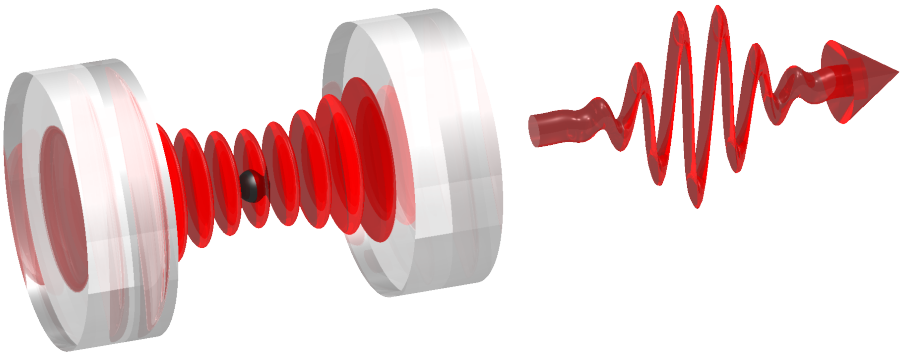

Tatjana Wilk

MPQ 320 **February 2008**

Abstract: A single atom strongly coupled to a high-finesse optical-cavity is a versatile tool for quantum information processing. Utilized as a single-photon source, it allows one to generate single photons very efficiently in a well defined spatio-temporal mode. In a first experiment, polarization-control over the photons is shown. A time-resolved two-photon interference experiment proves the indistinguishability of these photons - required in various quantum information processing schemes. Moreover, in a second experiment, entanglement between the polarization of the emitted photon and the population of the atomic Zeeman levels is created. Subsequent state mapping of the atomic state onto another photon results in a pair of polarization-entangled photons emitted one after the other from the cavity. Although these schemes are in principle possible in free space, the cavity boosts the efficiency by several orders of magnitude.

Keywords: single photons, entanglement, cavity quantum electrodynamics

Kurzfassung: Ein Atom, stark gekoppelt an einen optischen Hochfinesse Resonator, ist ein vielseitiges Werkzeug zur Quanteninformationsverarbeitung. Es erlaubt die effiziente Erzeugung eines Einzelphotons in eine wohl definierte raum-zeitliche Mode. In einem ersten Experiment wird die Kontrolle über die Polarisation der emittierten Photonen gezeigt. Ihre Ununterscheidbarkeit, die von vielen Schemata der Quanteninformationsverarbeitung verlangt wird, belegt eine zeitaufgelöste Zweiphotoneninterferenz. Zudem wurde in einem zweiten Experiment Verschränkung zwischen der Polarisation des emittierten Photons und der Population der Zeeman-Zustände eines Atoms erzeugt. Der anschließende Zustandstransfer des atomaren Zustands auf ein weiteres Photon resultiert in einem Paar polarisationsverschränkter Photonen, die nacheinander den Resonator verlassen. Obgleich diese Schemata im Prinzip auch im Freiraum möglich wären, so steigert der Resonator die Effizienz um mehrere Größenordnungen.

Schlagwörter: Einzelphotonen, Verschränkung, Resonator-Quantenelektrodynamik

Contents

Chapter 1

Introduction

Quantum effects do not appear *naturally* in everyday life. We see the world through classically-colored glasses, and that is why people find quantum mechanics surprising, unintuitive, bizarre, but also fascinating. In contrast to the classical world, where a system can have only one value (of a number of exclusive values) for a given property, in the quantum world a system can incorporate all values of this property at the same time. However, such a superposition state can never be directly observed on a single system. A measurement on a quantum system will always result in one of the eigenstates of the measurement operator (1). Since the choice of the measurement basis is arbitrary, it is rarely the case that one of these eigenstates coincides with the state under observation. The measurement process projects the system's state onto the result, such that repeated measurements will always give the same result. Therefore, only very little knowledge is gained from a single measurement about the original state. This *non-classical* quantum phenomenon is most evident in the prominent example of quantum entanglement between two objects (2; 3), illustrated here by the example of two particles A and B in a certain spin-entangled state. When observing these particles separately, the measurement results appear random in every measurement basis, which is consistent with each particle being in a completely mixed state. But, considering the measurement results of both particles, the measurements are perfectly correlated, i.e. particle A and particle B are always found in orthogonal spin states in all measurement bases even if they are spatially separated.
In the last decades a new field in physics emerged from these quantum phenomena: the field of quantum information processing. For an overview see (4; 5; 6). In addition to quantum information theory (7) this new direction of research explores possible applications such as quantum cryptography (8) and quantum computation (9; 10).

Quantum computers are based on the principle of quantum parallelism. Using a two-level quantum system to store information similar to a classical bit, namely in a qubit (11), information can be processed for any superposition of these levels. The idea of building a quantum machine similar to a classical computer was first mentioned by Benioff (12), and Feynman proposed to simulate quantum physics with such a device consisting of a well-controlled quantum system (13). Deutsch extended this idea to a universal quantum computer (14; 15). It has been shown that its implementation on a physical system at most requires to manipulate two qubits at a time (16). That means performing single-qubit rotations combined with two-qubit operations, e.g. CNOT gates, or with teleportation (17) is sufficient to run arbitrary quantum gates. Being a generalization of its classical counterpart, a quantum computer can run all classical algorithms. Moreover, the ability to process superposition states allows to find algorithms that reduce the complexity of certain problems compared to classical algorithms. The first such algorithm - to tell whether a function is constant or balanced - was reported by Deutsch and Jozsa (18). Solutions for more important problems followed, such as the data-base search (19; 20) and the number factorization (21), which is the key to decrypt classical cryptography protocols.
Many different approaches are currently pursued to implement these ideas of a quantum computer. The requirements a system has to meet are summarized in the DiVincenzo criteria (22). Systems using nuclear magnetic resonance (NMR) of molecules (23) were the first to experimentally demonstrate a full quantum algorithm on a set of up to five qubits (24; 25). However, this method is not scalable to more than tens of qubits. In solid state systems one idea is to use electron spins in quantum dots (26; 27; 28), another method is to use super-conducting qubits (29; 30; 31; 32). The idea to operate a quantum computer with single photons and linear optics only (33; 34) raised attention in the last years. Qubits are encoded in beam lines and the effect of two-photon interference (35; 36) is utilized to perform two-qubit gates. Therefore, it requires indistinguishable single photons, beam splitters, wave plates and single-photon detectors. Simple gates were demonstrated by various groups (37; 38; 39).
One of the most advanced approaches so far is quantum computing with trapped single ions using laser or microwave transitions to do single-qubit rotations and a phonon bus to perform two-qubit gates (40; 41). Based on these proposals different groups implemented such gates and realized algorithms based on a few qubits (42; 43; 44; 45), also including error correction (46). These systems are very well controlled and allow to deterministically entangle up to 8 ions in one trap (47; 48; 49; 50). However, in an ion trap system scalability is a problem. To face this challenge large trap architectures with many interaction and storing regions, with the possibility to shuttle small subsets of ions between these areas, were proposed (51). Ion traps with segmented electrodes have been realized that allow to transport

the ions between different trapping regions (52; 53; 54).
A more general approach to solve the scalability problem is to interface registers of stationary qubits (nodes) with flying qubits in a quantum network. This will allow distributed quantum information processing involving many nodes. Photons are perfectly suited to transmit information between distant nodes, as shown in many quantum cryptography protocols.

Quantum cryptography was first proposed by Wiesner (55) and can assure secure communication by quantum key distribution (56; 57). Functionality based on first principles has been shown over long distances (more than 100 km), in fibers as well as in free space (58; 59; 60; 61). To elongate the reachable distances even further a chain of quantum repeaters (62) can be used. Thus, even if quantum computers are at a stage where they can decrypt common classical cryptography protocols by factorization of large numbers, quantum mechanics itself offers a fundamental solution for secure communication.
Quantum cryptography is based on the *no cloning theorem* (63), which states that a quantum state can not be copied exactly. Hence, any attempt of eavesdropping can be detected by the two communicating parties through the fact that a measurement changes the quantum state. The fundamental prerequisite in these protocols is therefore that information is coded in single qubits only. This makes single-photon sources an essential ingredient for quantum communication. Single photon sources have been realized in many systems (64), e.g. using single nitrogen-vacancies (65; 66), single quantum dots (67; 68), single molecules (69), single trapped atoms (70; 71; 72; 73) and strongly-coupled atom-cavity systems (74; 75; 76; 77; 78). In principle, atom-cavity systems can generate single photons deterministically into a well defined mode which is easy to detect, making them much more efficient than other sources. Another unique feature of these systems is the possibility to control the spatio-temporal mode of the emitted photons and even their polarization (79), as will be explored in this thesis. The ability to emit single-photon wave-packets with a symmetric envelope is essential for a reversable state transfer (80), which allows the efficient absorbtion of photons (81) by other nodes in a quantum network.

Quantum networks are the key to scalable quantum information processing. They have to accomplish the task to combine the computational skills of a quantum register with the feature of receiving and sending quantum information between distant parties. Therefore, the ability to transfer a stationary qubit onto a flying qubit and vice versa is inevitable.
Amongst other proposals, such an interface was suggested for the realization with atomic ensembles (82; 83). Different groups in the field demonstrated state mapping from an atomic ensemble onto a single photon (84)

as well as teleportation of the state of a coherent light pulse onto an atomic ensemble (85). Entanglement between light and the atomic ensemble has been observed (86) and entanglement between distant atomic ensembles was achieved (87). However, schemes based on single photons and atomic ensembles suffer from their non-zero multi-photon component. Furthermore, until now atomic ensembles are unapt as a quantum memory since the qubit can only be stored up to tens of microseconds (88; 89).
In contrast, trapped atoms or ions have proven to have coherence times of several seconds (90; 91). In combination with their achievements performing quantum algorithms, they promise to be an ideal quantum memory. The ability to entangle a single trapped atom with an emitted photon in a probabilistic scheme has been shown (70; 72) as well as the conditioned entanglement between two atoms at a distance (92). However, in these free-space schemes the success probability is low. Since the strong atom-cavity coupling achievable in high-finesse cavities (93; 94; 95) allows one in principle to generate single photons with unity probability (75), they provide an intrinsically deterministic atom-photon interface (96) as reported here.
The possibility to channel the quantum information stored in internal atomic states into a photon emitted into a well-defined direction determined by the cavity is the key to multiple prospects, like the entanglement (97; 98; 99) and teleportation (100; 101) in a distributed quantum network. Most of these schemes, as well as linear optical quantum computing (33), require single photons to be indistinguishable. Even though it was demonstrated for a single quantum dot to deliver indistinguishable photons (102), so far, natural variations in the fabrication prohibit to produce indistinguishable photons from two different quantum dots. In contrast, this characteristic can naturally be delivered from sources based on the fundamental structure of single atoms (69; 73; 77; 103).

This thesis presents the realization of an essential building block for distributed quantum information processing, namely an atom-photon interface based on an atom-cavity system with the ability to generate single photons. In **chapter 2** the principle of the single photon source is introduced, the setup and changes necessary to enable the following experiments are described. In **chapter 3**, a first experiment demonstrates the capability of the new setup as a single photon source for polarized photons (79; 104). The mutual coherence of these photons is investigated in a time-resolved two-photon interference experiment. **Chapter 4** reports on a second experiment, where the atom-cavity system is used to entangle the atom with a first emitted photon and subsequently map the atomic state onto a second photon (96). This results in a pair of entangled photons, successively emitted from the cavity and characterized by tomography of their two-photon polarization state. An outlook to future experiments is given in **chapter 5**.

Chapter 2

A cavity-based single-photon source with Rubidium 87

The background of this thesis is the work of Markus Hennrich (105) and Thomas Legero (106), who together have build the photon pistol experiment. Markus Hennrich realized the "Controlled generation of single-photons in an optical high-finesse cavity" with ^{85}Rb and Thomas Legero extended this work by an investigation on the indistinguishability of the emitted photons by means of a "Time-resolved two-photon interference". In this thesis, the single-photon source has been converted to operate with a different isotope of Rubidium. The different energy level structure due to the different nuclear spin of ^{87}Rb (3/2 instead of 5/2 in ^{85}Rb) enables the major improvements on the photon pistol described in this work, i.e. the generation of polarized single photons (chapter 3) and the creation of atom-photon entanglement (chapter 4). In this chapter, the principle of the cavity-based single-photon source is summarized (section 2.1), more details can be found in (74; 107; 108). In section 2.2 the setup will be introduced, and finally, in section 2.3 the changes that were implemented into the system in order to work with ^{87}Rb are discussed.

2.1 Principle of the photon pistol

To illustrate the single-photon generation process, we consider a lambda-type three-level atom inside a high-finesse optical cavity as it is shown in Fig. 2.1. The atomic ground state $|u\rangle$ is coupled to the excited state $|e\rangle$ by a pump laser field with peak Rabi-frequency Ω_p that illuminates the system from the side. The other ground state $|g\rangle$ is coupled to the same exited state via the cavity with coupling constant $2g$. Both the cavity and the pump laser can be detuned from the excited state $|e\rangle$. But to drive the process efficiently they should be detuned by the same frequency Δ to be in Raman resonance. Then the effective Rabi frequency for the process is

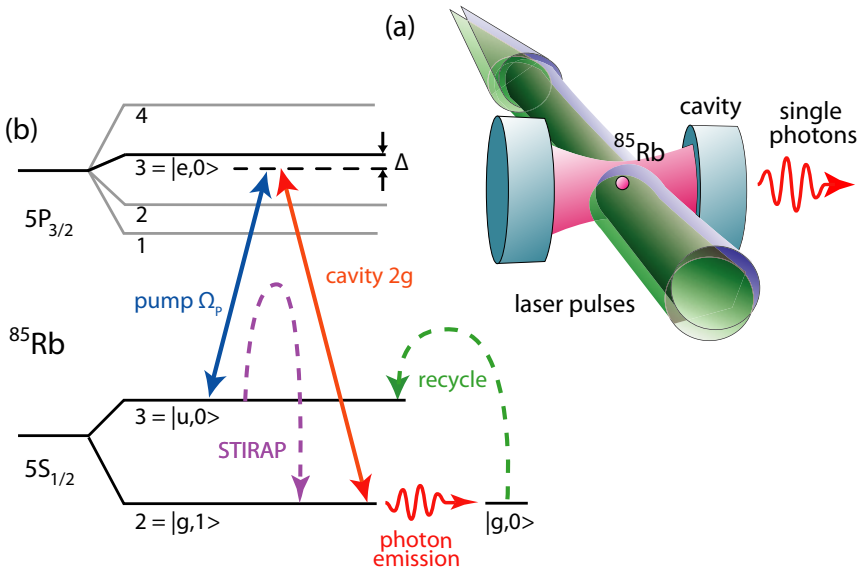

Figure 2.1: **Principle of the photon pistol.** (a) A lambda-type three-level atom is strongly coupled to the mode of a high-finesse resonator. Laser pulses illuminate the system from the side. (b) The system is initially prepared in state $|u, 0\rangle$. Together with the vacuum field of the cavity, the pump laser drives a STIRAP transition from state $|u, 0\rangle$ to $|g, 1\rangle$ and a photon is deposited into the cavity. When the cavity decays, the photon is released from the system and the system ends up in state $|g, 0\rangle$. Because this state is not excited by the laser, no further emission is possible. Only when the atom is brought back into the initial state by a repump process can another photon be generated.

given by $\Omega_{\text{eff}} \sim 2g\Omega/\Delta$.

The states of the combined atom-cavity system can be written as a superposition of product states $|i, n\rangle$ with $i \in \{u, g, e\}$ representing the atomic state and $n \in \mathbb{N}$ denoting the number of photons inside the cavity. Note that the cavity only couples product states of different photon numbers, whereas the interaction of the atom with the pump laser leaves the intra-cavity photon number unchanged. Initially the system is prepared in state $|u, 0\rangle$ with the atom coupled to the cavity field. To trigger a photon emission, the pump laser intensity, initially turned off, is increased slowly to drive a stimulated Raman adiabatic passage (STIRAP) (109) to the state $|g, 1\rangle$. In this process a photon is deposited in the cavity. Due to non-zero transmission of the cavity mirrors, the cavity state decays, and the photon is emitted from the system. The combined system ends up in state $|g, 0\rangle$ from where no further emission is possible. Only if the system is brought back to the initial state with the help of a repump laser, the emission of another photon can be triggered again by repeating the pulse sequence.

In the scheme with ^{85}Rb the two levels $|u\rangle$ and $|g\rangle$ are represented by the two

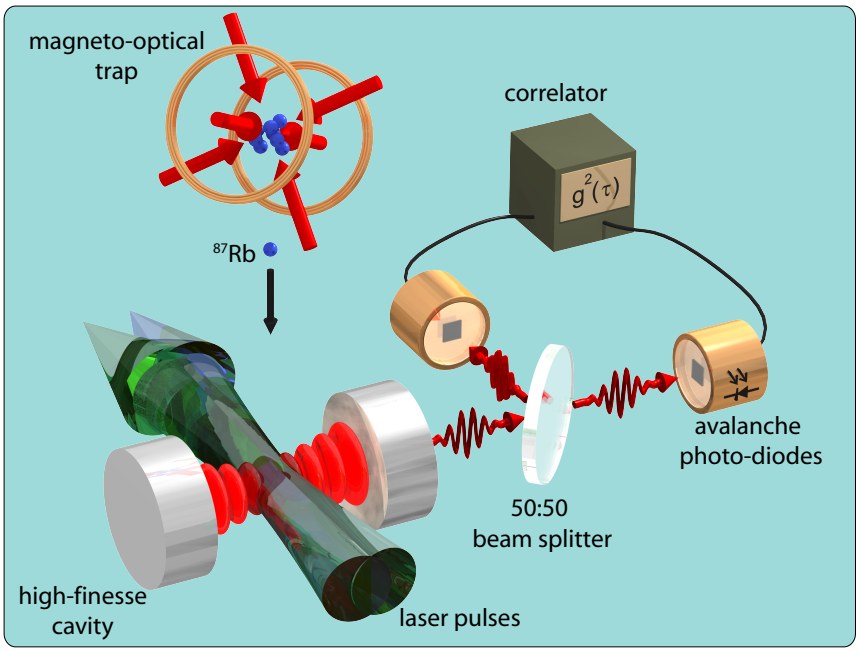

Figure 2.2: **Experimental setup.** A cloud of ^{85}Rb atoms prepared in a magneto optical trap (MOT) falls after release through the mode of an optical high finesse cavity. Together with the cavity, laser pulses illuminating the atoms from the side drive vacuum stimulated Raman transitions. The single photon source is investigated with a Hanbury Brown & Twiss detection scheme consisting of a beam splitter and one avalanche photo diode in each output port.

hyperfine ground states $F = 3$ and $F = 2$ of the $5S_{1/2}$ level, respectively. The excited state $|e\rangle$ is represented by the $F' = 3$ state of the electronically excited level $5P_{3/2}$ of the D_2 line. Of course, each of these levels in Rubidium consists of multiple Zeeman sublevels and transitions are driven between superposition states of these sublevels. Therefore the polarization of the emitted photons is undefined in the experiments that used this scheme for the photon production (74; 106; 110; 111).

2.2 Setup

A schematic of the setup is shown in Fig. 2.2. The setup resides in a vacuum chamber with two main chambers that are connected by a differential pumping stage. In the upper chamber, ^{85}Rb atoms are captured from background vapor in a magneto-optical trap (MOT) and cooled by an optical molasses to a few μK (112; 113). The cavity is located about 20 cm below the MOT in the lower lying chamber (10^{-9} mbar). When released from the MOT, the atomic cloud falls under gravity through the mode of the high finesse optical cavity. Pump laser pulses illuminating the atoms from the side trigger

the photon emission into the cavity mode. The single photon nature of the source is then characterized using a beam splitter and two detectors for a Hanbury Brown & Twiss measurement, in which the autocorrelation of the photon stream is investigated. For an ideal single photon source one will never find clicks in the two detectors at the same time.

2.2.1 High-finesse cavity

The heart of the experiment is the high-finesse optical cavity consisting of two spherical mirrors with radius of curvature of 50 mm that are separated by a distance of 0.98 mm. The Gaussian TEM_{00} mode has a waist of $w_C = 35\,\mu$m. Figure 2.3 shows a photo of the kind of cavity setup used in this experiment: The mirrors are glued to their aluminium holders and the piezo tube regulates the distance between them. The two mirrors have different transmission coefficients. One mirror has a transmission of $T_1 = 1.8$ ppm, whereas the other mirror was chosen to be the outcoupling mirror for the generated photons, therefore its transmission is much larger, $T_2 = 100$ ppm. With the higher transmissive outcoupling mirror the cavity has a finesse of 58,000, which is an order of magnitude less than other experiments with two mirrors of highest achievable reflectivity (93; 94; 95) designed to work deeper in the strong coupling regime ($g \gg \{\kappa, \gamma\}$). However, in a symmetric cavity the maximal outcoupling efficiency in one direction is limited to 50%. In contrast, together with the absorption losses in the mirrors, $L_1 + L_2 = 6.3$ ppm, the probability that a generated intracavity photon exits the cavity through this outcoupling mirror is $P_{out} = T_2/(T_1 + T_2 + L_1 + L_2) = 92.5\%$. The atom-cavity coupling in an antinode of the mode is well-approximated semiclassically to

$$g_{\max} = \sqrt{\frac{w_C}{2\epsilon_0 V \hbar}}\mu_{ge}, \tag{2.1}$$

where $\epsilon_0 = 8.85 \cdot 10^{-12}$ As/Vm is the vacuum permittivity, V is the mode volume and μ_{ge} is the dipole matrix element of the atomic transition from $|g\rangle$ to $|e\rangle$. For ^{85}Rb with the cavity tuned to the transition from $F = 2$ to $F' = 3$ an averaged atom cavity coupling of $g_{\max}/2\pi = 2.5$ MHz. With the cavity decay rate $\kappa/2\pi = 1.25$ MHz and the atomic polarization decay rate $\gamma/2\pi = 3$ MHz the cooperativity parameter is $C = g_{\max}^2/2\kappa\gamma = 0.83$. For transitions from $F = 1$ to $F' = 1$ in ^{87}Rb as used in the experiments described in chapter 3 and 4 the atom-cavity coupling is $g_{\max}/2\pi = 3.1$ MHz resulting in a cooperativity parameter $C = 1.28$. In both cases the system is operating on the edge of strong coupling ($C \approx 1, g_{\max} > (\kappa, \gamma)$).
The length of the cavity is stabilized on the transmission signal of a laser at the desired frequency. This laser is frequency modulated and the error signal is generated by a Lock-in amplifier as described in (105). While the atomic cloud from the MOT is falling through the cavity mode, the stabilization laser is switched off and the voltage of the cavity piezo is fixed by a sample

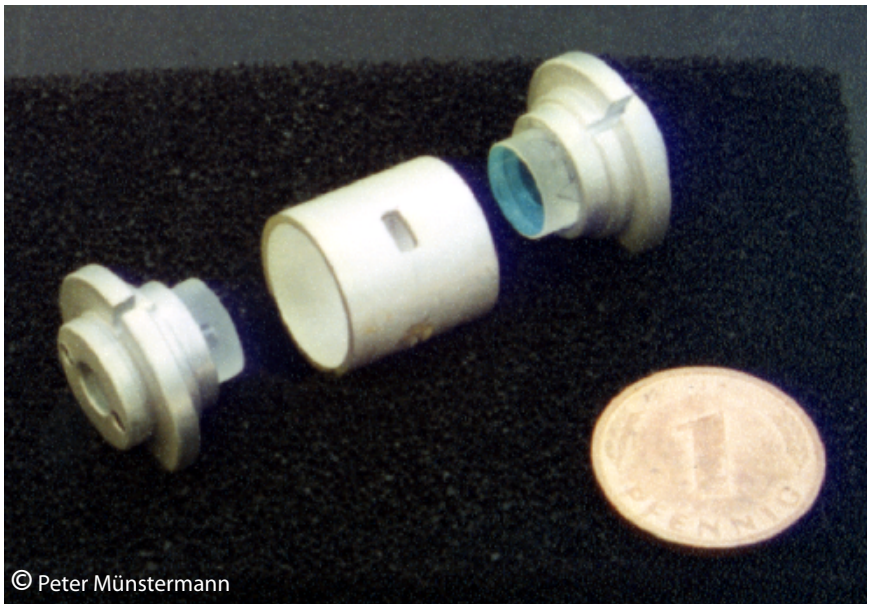

Figure 2.3: **High finesse-optical cavity** of the kind used in the setup, before building it into the vacuum setup. Shown are the two high reflecting mirrors glued to their aluminium holders and the piezo tube that regulates the distance between the mirrors. The piezo tube has holes for the passing atoms and for the laser beams that illuminate the atoms from the side. To get an idea of the dimensions of the cavity setup, a *Pfennig* is shown, the German currency before 2002. It has a slightly bigger diameter (16.50 mm) than the new European currency the *Euro-cent* (16.25 mm).

and hold technique. The cavity frequency drift is so slow that after a time of 30 ms the changes of frequency are smaller than the cavity linewidth and the stabilization can be recaptured again.

2.2.2 Experimental sequence

The whole experimental sequence runs with a repetition rate of about 1.7 Hz. During each cycle, first, the intensities of the lasers are checked and corrected, and it is verified that the cavity is still locked. If this is not the case, the computer control stops the sequence. If it is locked, the MOT is loaded for a variable time (about 50 ms), after a molasses phase without magnetic field, all MOT beams are turned off and the atoms are released. Since the cavity is located about 20 cm underneath the MOT, the atomic cloud falls about 200 ms until it reaches the cavity. Before the atoms enter the cavity, the stabilization laser is turned off, so that all photons have leaked out and the mode is in the vacuum state. Then the pump pulse sequence is started and repeated for about 5 ms. The photons emitted from the cavity are detected with avalanche photodiodes (APDs) and are recorded with a

transient recorder card *PCI.258* by *Spectrum*.

2.3 Conversion to Rubidium 87

Fortunately, changing the isotope of Rubidium did not require to open the vacuum system. The naturally occurring rubidium in the reservoir connected to the vacuum chamber is composed of the two stable isotopes, ^{85}Rb and ^{87}Rb with a relative abundance of 72.2% and 27.8%, respectively. The D_2 lines of the isotopes are only a few GHz apart, so that they are accessible by frequency tuning the same lasers. However, the laser setup was changed to a more convenient system with commercial diode lasers instead of the combination of two home-made low power diode lasers and a titanium-saphir solid-state laser pumped by an argon-ion gas-laser. In addition the experimental sequence has been optimized for longer measuring times and the data acquisition has been upgraded to allow for higher repetition rates.

2.3.1 Laser system

The new laser system consists of two commercial diode lasers from *Toptica Photonics*:

The DL100 diode laser is an extended cavity diode laser (ECDL) with a grating in Littrow configuration. It has an output power of about 100 mW. This laser serves all beams on the D_2-line that start from the $F = 1$ hyperfine ground state of ^{87}Rb. It is stabilized on the crossover resonance between the $F = 1$ to $F' = 1$ and $F' = 2$ resonances in a frequency modulated (FM) saturated absorption spectroscopy (114; 115; 116). All frequencies necessary in the experiments can be reached using acousto-optical modulators (AOMs). For the doppler-free absorption spectroscopy the laser is phase modulated at by an electro-optical modulator (EOM). From the spectroscopy signal the error signal is deduced by mixing with the local oscillator. Using a PID regulator, this error signal is fed back onto the laser in three different feedback loops. Long term stability is maintained by feedback onto the grating Piezo (bandwidth up to 1 kHz) and two separate short term stabilization feedback loops (ranging up to a few MHz) control the laser frequency directly by modulating the current of the diode. Details on the laser stabilization can be found in (117). With this technique the laser linewidth is reduced from about 1 MHz free-running to about 120 kHz when all feedback loops are turned on.

The DLX110 Rocksolid high power single mode diode laser consists of a tapered amplifier chip, where the emission on the back side is used for external feedback with a grating. This laser has an output power of

about 850 mW and serves as the light source for all beams starting from the $F = 2$ hyperfine ground state. These beams are for the MOT cooling beams, which is why the laser with the higher output power is used for this transition. The *DLX110* is also stabilized by FM saturated absorption spectroscopy directly to the crossover resonance from $F = 2$ to $F' = 1$ and $F' = 3$. Here, the frequency modulation is applied directly onto the laser current. Again fast and slow feedback onto the grating and the current are used to stabilize the laser frequency. A stability of the laser of a few 100 kHz is reached which is much lower than the atomic linewidth.

2.3.2 Speeding up the event rate

The measurements that were done for the quantum beat, Fig. 3 in (77), were very time consuming. It took a total time of three days to collect all the data needed with the time resolution and signal to noise ratio necessary. Each experimental cycle was about 600 ms long, but the actual measuring window in each cycle was only 5 ms long. Another time consuming factor was the data acquisition, which depended on the time resolution setting of the *PCI.258*-card. Both aspects, the short measuring time per cloud and the long data acquisition, have been improved as is described in the following paragraphs.

Temperature of the atomic cloud

To increase the measuring time per dropped atomic cloud, it is advantageous not to cool the atoms to too low temperatures T. The colder the atomic cloud, the smaller the velocity spread σ_v, following the relation

$$\frac{1}{2}k_B T = \frac{1}{2}m\sigma_v^2, \tag{2.2}$$

where $k_B = 1.38{\cdot}10^{-23}\,\mathrm{J/K}$ is the Bolzmann constant and $m = 1.43{\cdot}10^{-25}\,\mathrm{kg}$ is the mass of a ^{87}Rb atom. With a larger velocity spread σ_v the atomic cloud will expand faster after releasing it from the trap. Therefore, the whole cloud will need more time to pass through the cavity mode, as can be seen in a time-of-flight measurement. With this method we could increase the window for measurements by a factor of 4 from 5 ms to 20 ms, indicated in light blue and gray in Fig. 2.4, where a transit of the atomic cloud through the cavity is shown for improved conditions of MOT and molasses stage compared to the original experiment. Displayed are the number of detected photons as a function of time. The pump and recycling laser both are continuously turned on during the whole measurement to scatter as many photons as possible and many experimental cycles are accumulated. The curve is normalized, since only the width is of interest. As a reference the dark grey line shows the signal that is expected for an atomic cloud with a

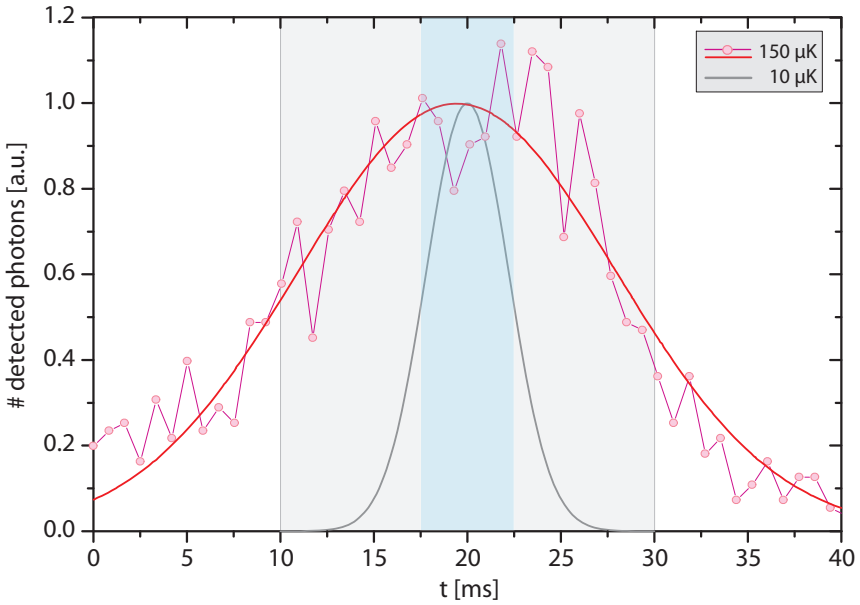

Figure 2.4: **Expansion of the atomic cloud.** The intensity and frequency of the optical molasses were optimized to have a longer interaction time for a more expanded cloud when it reaches the cavity. The measurement time-window for atoms passing the cavity has been increased from 5 ms to about 20 ms.

temperature of $T = 10\,\mu$K as it was observed in the experiments with ^{85}Rb. From the widths of the time-of-flight measurements τ_{tof} (half width at 1/e) the temperature of the atomic sample can be calculated. Here, we assume that the expansion of the cloud starting from the MOT is negligible. The distance from the MOT to the cavity is $z = 20\,$cm, therefore the mean velocity of the atoms in the cavity is $v_z = 2\,$m/s. The velocity spread is calculated as

$$\sigma_v = \frac{\tau_{\text{tof}} \cdot v}{t}, \tag{2.3}$$

and together with Eq. (2.2) we find a temperature of $T = 150\,\mu$K for the data in Fig. 2.4.

Naturally, with a more expanded cloud of atoms, the flux of atoms through the cavity will be reduced for a constant number of atoms in the cloud. To keep the flux constant, the loading time of the MOT simply has to be extended. Note that a hotter cloud does not mean that the position change of an atom in the cavity is faster and thus the atom-cavity coupling is as well defined as in previous experiments. A number of slits in the direction perpendicular to the falling atom selects only atoms that are cold in directions perpendicular to gravity.

To achieve a slightly hotter atomic sample than in the old experiments with ^{85}Rb, the configuration of intensities and detunings at the end of the MOT and optical molasses phase have been changed. While in the old experiments

the cooling laser intensity was lowered stepwise in the last 10 ms of the MOT and molasses phase, it is now set to zero in one step at the end of the molasses phase. We also changed the detuning of the cooling laser during the optical molasses. When the magnetic field is turned off 3 ms before releasing the cloud, the detuning of the cooling beams are switched to −46 MHz with respect to the cycling transition instead of −56 MHz in the old experiments.

Data acquisition

To increase the speed of data acquisition, we replaced the *PCI.258* transient recorder card with a *P7888* multi-event time digitizer card by *FAST ComTec*. While the transient recorder card stored a voltage value for every time-bit, the *P7888* card only stores the times of triggering events. For low event rates storing only event-times is favorable, since the amount of data that has to be handled is much lower.
With the exchange of the data acquisition card the duration of the sequence could be shortened from about 600 ms to 400 ms. Together with the extension of the measurement window per cloud these technical improvements lead to an increase in the repetition rate of the experiment of a factor of six. The original three days measuring time turned into half a day, making measurements on the system much more comfortable.

Chapter 3

Polarization-controlled single photons

In this chapter the photon-generation scheme described in chapter 2 is extended in such a way that single photons of well-defined polarization are emitted from a coupled atom-cavity system. In the previous work, Raman transitions between hyperfine states of a ^{85}Rb atom were used to generate single photons (74; 110; 118; 77), but the large number of accessible magnetic sublevels in ^{85}Rb meant that the polarization of these photons was undefined. Moreover, a repumping laser was necessary to re-establish the starting conditions after each photon emission. In this new scheme ^{87}Rb is used and transitions are now driven between the two Zeeman substates $|\pm 1\rangle$ of the $F = 1$ hyperfine ground state. A magnetic field is applied to lift the degeneracy of these states. With the frequency of the applied laser one can address either the transition from $|+1\rangle$ to $|-1\rangle$ which produces a σ^+ photon or the reverse transition while emitting a σ^- photon. By applying both pulses one after the other one can generate a stream of photons with alternating polarization. Thereby no repumper is necessary, since the final state of the forth process is the initial state of the back process and vice versa.
A detailed description of the scheme is given in section 3.1 and is supplemented by simulations of the photon generation process (107; 104; 117). In section 3.2, the experimental implementation of the scheme is described. Then in section 3.3 this new type of single-photon source is demonstrated and characterized (79). In section 3.4, the time-resolved two-photon interference experiment is discussed to show how well subsequent photons resemble each other and to what degree they are suitable for quantum information processing.

3.1 Theory and simulations

In this section, first the basic idea of the scheme for polarization controlled single photons is described in subsection 3.1.1. In subsection 3.1.2 simulations for an idealized three level atom are discussed that calculate the time evolution of these states. Finally, in subsection 3.1.3 this ideal case is adapted to a situation with a real ^{87}Rb atom.

3.1.1 Basic idea

To achieve polarization control of the photons emitted from the atom-cavity system the situation shown in Fig. 3.1 is investigated. Vacuum-stimulated Raman transitions are considered between the $m_F = \pm 1$ Zeeman substates of an $F = 1$ hyperfine state, e.g. in the electronic ground state of ^{87}Rb atoms. A magnetic field along the cavity axis lifts the degeneracy of the magnetic substates. If the frequency of the applied laser pulses is either red or blue detuned from the unperturbed transition by twice the B-field induced Zeeman shift, while the cavity frequency is in resonance with the unperturbed atomic transition, then the transition between the $m_F = +1$ and $m_F = -1$ levels is resonantly driven by laser and cavity, but with their roles changing as a function of the chosen laser detuning. In this way the Raman transition between the $m_F = \pm 1$ hyperfine states can be driven in one or the other direction by choosing a red or blue laser detuning, leading to an emission of either a σ^- or σ^+ photon, respectively. As can be seen in the level scheme shown in Fig. 3.1, this method requires the laser to be polarized perpendicularly to the cavity axis, so that it has equal contributions of σ^+ and σ^- polarization components with respect to the magnetic field direction. Only the σ^+ polarization component of the driving laser is used for the generation of a σ^- polarized photon and vice versa. The other polarization component of the laser pulse is always present, but it is out-of-resonance with all relevant atomic transitions and Raman processes.
As the cavity supports both polarization modes, alternating the laser frequency between the two possible resonances from pulse to pulse generates a sequence of single photons of alternating polarization. No repumping of the atom to its initial state is required from one photon to the next, since the final state reached with a σ^+ photon emission is at the same time the initial state for producing a σ^- photon with the subsequent driving laser pulse and vice versa.

3.1.2 The ideal three-level system

Consider an idealized atom with an $F = 1$ hyperfine ground state and an $F' = 0$ electronically excited state. The Zeeman shift induced by the

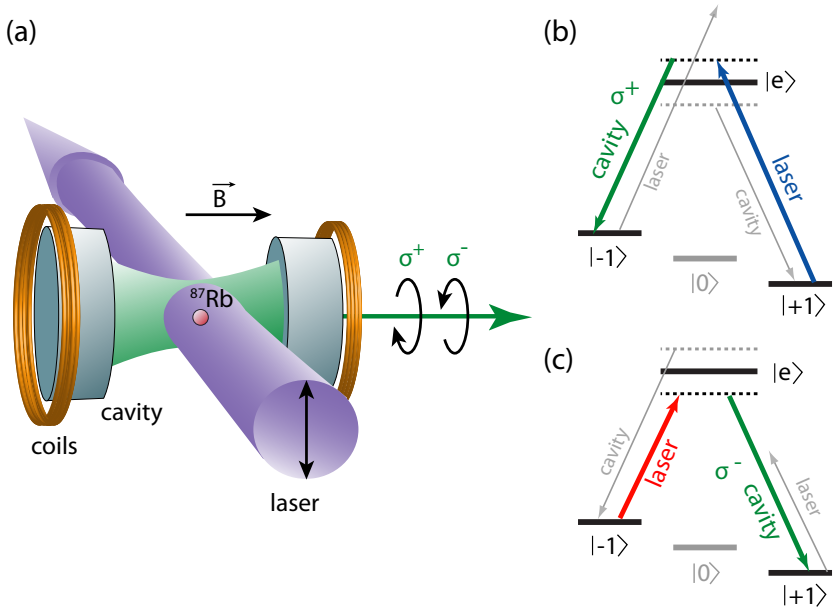

Figure 3.1: **Principle of the photon generation scheme.** A single atom is strongly coupled to an optical cavity, and a magnetic field acting along the cavity axis lifts the degeneracy of the Zeeman substates (a). Together with the cavity that provides σ^+ and σ^- modes, laser pulses from the side drive Raman transitions in the atom. The polarization of the laser is perpendicular to the cavity and B-field axis, so that it has equal σ^+ and σ^- components. The cavity is resonant with the unshifted atomic transition, but the laser pulse is red or blue detuned: A blue detuned laser pulse drives a Raman transition from $m_F = +1$ to $m_F = -1$ and generates a σ^+ polarized photon (b), while a red detuned laser pulse drives the transition in the opposite direction and generates a σ^- polarized photon (c).

magnetic field on the $m_F = \pm 1$ atomic ground states is

$$\Delta_B = \mp |g_L| \mu_B B, \tag{3.1}$$

where μ_B is the Bohr magneton and g_L the Landé factor for the atomic hyperfine state. In the following, the $m_F = \{-1, 0, +1\}$ Zeeman substates of the $F = 1$ ground state will be written as $|-\rangle$,$|0\rangle$ and $|+\rangle$, respectively, whereas the $F' = 0$ excited state is labelled $|e\rangle$. For geometric reasons the cavity supports only σ^+ and σ^- photons, which have identical frequencies if the relevant cavity modes are degenerate. The state of the coupled atom-cavity system can therefore be written as a superposition of product states $|i, n_+, n_-\rangle$, with i representing the atomic state, and $n_\pm$ denoting the number of $\sigma^\pm$ photons. Here, the number of photons in each mode is restricted to zero or one, since higher photon numbers are very unlikely. As mentioned already in section 2.1 the cavity couples only product states of different photon numbers, while the interaction of the atom with the pump laser leaves the intra-cavity photon number unchanged. The pump frequency ω_p and

the cavity resonance frequency ω_c are both close to the $|0\rangle$ to $|e\rangle$ transition frequency ω_{0e}. The states $|0, n_+, n_-\rangle$ are also disregarded, since $|0\rangle$ is decoupled from all other internal states. In this way an atomic three-level system in a Λ-configuration is obtained. Here, the energy of the excited state $|e, 0, 0\rangle$ is chosen to define the origin of the energy scale and the Hamiltonian of the system is divided into two parts,

$$\hat{H} = \hat{H}_{stat} + \hat{H}_{int}. \tag{3.2}$$

The stationary part $\hat{H}_{stat}$ includes the energy levels of atom and cavity, and $\hat{H}_{int}$ describes the interaction of the atom with pump laser and cavity. The system is examined in the interaction picture. In the rotating wave approximation, the stationary part of the Hamiltonian reads

$$\begin{aligned} \hat{H}_{stat} &= \hat{H}_{atom} + \hat{H}_{cavity} \\ &= \hbar\Big[(\Delta_p + \Delta_B) \left|-\right\rangle \left\langle-\right| + (\Delta_p - \Delta_B) \left|+\right\rangle \left\langle+\right| \Big] + \hbar\Delta_{cp} \left(\hat{a}^\dagger \hat{a} + \hat{b}^\dagger \hat{b} \right), \end{aligned} \tag{3.3}$$

where $\Delta_p \equiv \omega_p - \omega_{0e}$ is the detuning of the pump laser from the transition between $|0\rangle$ and $|e\rangle$ and $\Delta_{cp} \equiv \omega_c - \omega_p$ is the difference between cavity resonance and pump laser frequency. Here, $\hat{a}^\dagger$ and $\hat{a}$, or $\hat{b}^\dagger$ and $\hat{b}$, are the creation and annihilation operators of a photon in the σ^+ or σ^- polarized cavity mode, respectively. The interaction between atom and cavity is given by the interaction Hamiltonian

$$\begin{aligned} \hat{H}_{int} = \; & -\hbar\Big[g\big(\left|e\right\rangle \left\langle-\right| \hat{a} + \hat{a}^\dagger \left|-\right\rangle \left\langle e\right| \big) + g\big(\left|e\right\rangle \left\langle+\right| \hat{b} + \hat{b}^\dagger \left|+\right\rangle \left\langle e\right| \big) \\ & + \tfrac{1}{2}\Omega\big(\left|e\right\rangle \left\langle-\right| + \left|-\right\rangle \left\langle e\right| \big) + \tfrac{1}{2}\Omega\big(\left|e\right\rangle \left\langle+\right| + \left|+\right\rangle \left\langle e\right| \big) \Big], \end{aligned} \tag{3.4}$$

where g is the coupling constant of the atom to both cavity modes (assumed to be equal), and Ω is the Rabi frequency of the pump laser.
The cavity decay gives rise to the emission of photons from the cavity, which is a non-unitary process. Its effects on the density matrix can be expressed by the Liouville operator (119),

$$\hat{L}[\hat{\rho}] = \kappa \left(2\hat{a}\hat{\rho}\hat{a}^\dagger - \hat{a}^\dagger\hat{a}\hat{\rho} - \hat{\rho}\hat{a}^\dagger\hat{a} \right) + \kappa \left(2\hat{b}\hat{\rho}\hat{b}^\dagger - \hat{b}^\dagger\hat{b}\hat{\rho} - \hat{\rho}\hat{b}^\dagger\hat{b} \right). \tag{3.5}$$

The cavity field decay rate κ, here identical for both polarizations, should be fast with respect to the Raman process to ensure that the photon is emitted from the cavity before being reabsorbed by the atom. In this simple model the atomic decay from level $|e\rangle$ is omitted.
The time evolution of the system is then given by the master equation

$$\frac{d}{dt}\hat{\rho} = -\frac{i}{\hbar}[\hat{H}, \hat{\rho}] + \hat{L}[\hat{\rho}]. \tag{3.6}$$

The initial state of the system is set to $|\Psi_{start}\rangle = |+, 0, 0\rangle$ and realistic parameters are chosen, $(g; \kappa; \Delta_B)/2\pi = (2.7; 1.25; 15)$ MHz. This corresponds

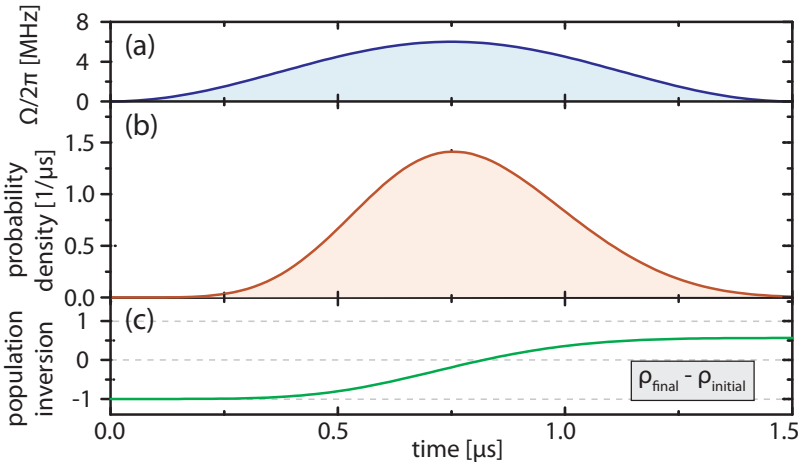

Figure 3.2: **Time evolution of an idealized three-level atom** with parameters $(g;\kappa;\Delta_B)/2\pi = (2.7;\,1.25;\,15)\,\mathrm{MHz}$. Time evolution of the system: (a) Pump laser Rabi-frequency $\Omega/2\pi$ follows a $\sin^2(\pi t/1.5\,\mu\mathrm{s})$-pulse amplitude, with a peak value of 6 MHz. (b) The probability density for generating a photon per μs is shown. Integrating over the whole pulse gives an emission probability of 78% per pulse. (c) Accordingly, the population transfer between the atomic state, defined by the difference in population of the final and initial state, ends up at an inversion of 0.56.

to the experimental situation of a ^{87}Rb atom in the $5S_{1/2}\,|F=1, m_F=+1\rangle$ hyperfine ground state and excitation of the D_2-line, inside a cavity like in subsection 2.2.1 and a magnetic field of 21.4 G. The cavity is in resonance with the $|0\rangle$ to $|e\rangle$ transition, (i.e. $\omega_c = \omega_{0e}$), and in order to resonantly drive the Raman transition from $|+,0,0\rangle$ to $|-,1,0\rangle$, the pump laser has to have a detuning of $\Delta_p = +2\Delta_B$. The pump-laser Rabi frequency follows a $\sin^2(\pi t/1.5\,\mu\mathrm{s})$-pulse amplitude with a peak value of $\Omega/2\pi = 6\,\mathrm{MHz}$ for each polarization, as shown in Fig. 3.2. The probability density for emitting a photon varies as a function of time, and reflects the envelope of the generated single-photon wave packet. Note that the shape of the photon depends on the driving field. Changing the shape of the pump pulse or its peak value has a direct impact on the emission probability. The photon can therefore be shaped in many desired ways. The integral of the probability density over the whole photon duration gives the overall emission probability of a photon, in this case 78%. The lower part of Fig. 3.2 illustrates the population inversion between the states $|-\rangle$ and $|+\rangle$, i.e. the population difference between the final and the initial atomic state. The inversion starts from -1 at $t = 0$ and increases until it reaches $+0.56$. Note that any losses from the system (except for cavity decay) have been omitted in this simplified model, therefore population which is not transferred into the other ground state simply stays in the initial state. Under these conditions, the emission

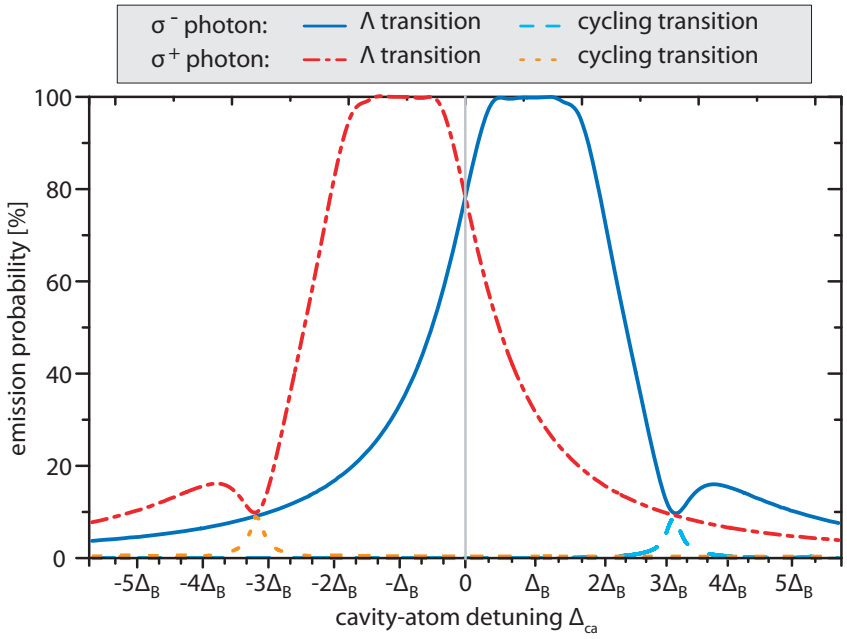

Figure 3.3: **Photon production probability for the ideal three-level atom** as a function of the cavity-atom detuning Δ_{ca}. The pump laser is always tuned to the desired Raman resonance: For σ^- photons $\Delta_{cp} = -2\Delta_B$, for σ^+ photons $\Delta_{cp} = +2\Delta_B$. Bluish lines stand for the probability for generating σ^- photons, reddish lines for σ^+ photons. Shown are the probabilities for the desired Λ-type transition and for the cycling transitions, starting and ending in the same state.

probability equals the fraction of transferred population. This is not the case in general, since other loss channels than the cavity exist.
During the population transfer from the state $|+,0,0\rangle$ to $|-,1,0\rangle$, the single photon state of the cavity decays. Since the time constant 2κ is much faster than the duration of the pump pulse, the photon leaks out of the cavity during its generation. Once the atom has reached the state $|-,0,0\rangle$, it will be very unlikely to undergo another Raman transition back to the initial state, since the back transition is detuned by $4\Delta_B$ (see Fig. 3.1 (b), grey lines) which is much larger than the cavity linewidth of 2κ. This means a second emission is suppressed and thus only a single σ^+ or σ^- photon is generated. The efficiency of the photon generation depends on many parameters. Here it is 78%, but it can rise up to 100% with increasing pump power or with a stronger atom-cavity coupling. For a larger Zeeman splitting the emission probability would decrease.
Exactly the same photon generation efficiency and photon envelope are obtained when the initial state is $|-,0,0\rangle$ and the detuning of the pump laser frequency is $\Delta_p = -2\Delta_B$. Then Raman resonance is fulfilled for the Λ-type transition shown in Fig. 3.1 (c) and a σ^- photon is generated. Both cases are

similar, since the cavity frequency has been chosen to be on the unshifted transition from $F = 1$ to $F' = 0$, leading to an atom-cavity detuning of $\pm\Delta_B$ with respect to the atomic resonances from $|+\rangle$ to $|e\rangle$ and $|-\rangle$ to $|e\rangle$. This symmetry is only broken when the cavity is detuned. In Fig. 3.3, the photon generation efficiencies are plotted as a function of the cavity-atom detuning, $\Delta_{ca} \equiv \omega_c - \omega_{0e}$, with the pump frequency always chosen such that the laser and cavity are in Raman resonance with either the $|+\rangle$ to $|-\rangle$ or the $|-\rangle$ to $|+\rangle$ transition, i.e. $\Delta_{cp} = \pm 2\Delta_B$. Blueish lines indicate the probability to emit a σ^- photon and reddish lines a σ^+ photon. The blue solid and red dashed-dotted line give the efficiencies for the photon production within the desired Λ-type Raman transitions, i.e. starting in $|+\rangle$ and ending in $|-\rangle$ for σ^+ and vice versa for σ^- photons. Driving a Λ-type transition with a cavity-atom detuning around $\Delta_{ca} = -\Delta_B$ for σ^+ photons (red dashed-dotted line) or $\Delta_{ca} = +\Delta_B$ for σ^- photons (blue solid line) leads to 100% efficiency of the process. In both cases, the detuning of the cavity compensates the Zeeman shift and the Raman transition is driven via the atomic state $|e\rangle$. However, in the case of a fixed cavity detuning generation of σ^+ and σ^- polarized photons with the same probability, is only possible with a compromise, i.e. $\Delta_{ca} = 0$ with an emission probability reduced to 78%.

To verify whether no unwanted second photon will emerge from the system, the probability for a photon production from an atom starting in the wrong initial state has to be calculated, e.g. state $|-\rangle$ for σ^+ photons. If σ^+ photons can be generated in this case, the atom would undergo a cycling transition, since the initial and final state are the same. As indicated by the reddish dashed line (blueish dashed line for the analogous case with σ^- photons) in Fig. 3.3, the probability for such cycling transitions is essentially zero in the frequency range around $\Delta_{ca} = 0$, where the scheme for generating photons of alternating polarization works best, so no second photon will be emitted. Only when the pump laser is near an atomic resonance does the emission probability become non-negligible. However, this phenomenon is however an artefact of the simplified model considered here. The peaks are appearing because the spontaneous decay of the excited atomic state has been omitted. Consequently, once the atom is in the excited state it can only emit into the far-off resonant cavity mode. In a real atom, the spontaneous decay to other states would dominate the atom's behavior.

In summary, this simple model shows that, for $\Delta_{ca} = 0$, single-photon polarization control can be achieved by choosing the appropriate pump-laser frequencies. There is no need to alter the cavity frequency or the pump polarization. Moreover, the probability to emit two photons during the same pump pulse is vanishingly small.

3.1.3 Polarized photons from ^{87}Rb

To analyze the behavior of a coupled atom-cavity system under more realistic conditions, all relevant atomic levels and the spontaneous decay of the excited states of ^{87}Rb must be taken into account. The level scheme of ^{87}Rb can be found in Appendix A. The $5S_{1/2}$ ground state consists of two hyperfine states, $F = \{1; 2\}$, with $2\pi \times 6.8\,\mathrm{GHz}$ hyperfine splitting, while the $5P_{3/2}$ excited state has four hyperfine substates, $F' = \{0; 1; 2; 3\}$, with splittings of $2\pi\times(72;\ 157;\ 267)\,\mathrm{MHz}$. The two $5S_{1/2}(F = 1, m_F = \pm 1)$ states are the $|\pm\rangle$ states in our scheme, while the virtual excited level of the Raman transition is some superposition of $5P_{3/2}(m_{F'}{=}0)$ states. Note that the origin of our energy scale is chosen to coincide with $F' = 0$, and this state is still labelled $|e\rangle$. In the ground state, $F = 2$ is so far from resonance with pump and cavity that there is effectively no coupling. Therefore spontaneous emissions into $F = 2$ constitute an additional loss channel for the atom, but the state as such need not be considered. Moreover, we restrict ourselves to a situation where the cavity frequency is near resonant with the transitions from $F = 1$ to $F' = \{0; 1\}$. With a distance of $2\pi \times 157\,\mathrm{MHz}$ between $F' = 1$ and $F' = 2$, the latter state is far from resonance. In addition, the dipole-matrix elements for transitions between $F = 1$ and $F' = 2$ are smaller than those for the relevant transitions to $F' = \{0; 1\}$ such that the $F' = 2$ state can be neglected. We also omit the $F' = 3$ state, since it does not couple to $F = 1$.
The stationary part of the Hamiltonian now includes all involved atomic levels. It reads

$$\hat{H}_{stat} = \hbar \left(\sum_i \Delta_i |i\rangle\langle i| + \Delta_{cp} \left(\hat{a}^\dagger \hat{a} + \hat{b}^\dagger \hat{b} \right) \right). \tag{3.7}$$

Here, Δ_i stands for the energy of the respective atomic level in the rotating frame, including pump detuning and Zeeman shift with respect to the zero level of our calculation. The interaction part of the Hamiltonian can be written as

$$\begin{aligned} \hat{H}_{int} = \; -\hbar \textstyle\sum_{i,j} \Big[& g_{ij}^{+} \big(|i\rangle\langle j|\hat{a}^\dagger + |j\rangle\langle i|\hat{a} \big) + g_{ij}^{-} \big(|i\rangle\langle j|\hat{b}^\dagger + |j\rangle\langle i|\hat{b} \big) \\ & + \tfrac{1}{2}\Omega_{ij} \big(|i\rangle\langle j| + |j\rangle\langle i| \big) \Big], \end{aligned} \tag{3.8}$$

where i and j denote ground and excited states, respectively. Transitions between $|i\rangle$ and $|j\rangle$ are either driven by the pump with a Rabi frequency Ω_{ij}, or by the coupling of the atom to the $\sigma^\pm$ cavity modes, with the atom-cavity coupling constants $g_{ij}^{\pm}$. Both Ω_{ij} and $g_{ij}^{\pm}$ depend on the angular part $\mathcal{A}_{ij}$ of the dipole matrix elements listed in Tab. 3.1 (120; 121). We have to distinguish between σ^+ and σ^- cavity coupling constants. They read $g_{ij}^{\pm} = \mathcal{A}_{ij} \cdot g_0$, but g_{ij}^{+} is zero unless $\Delta m \equiv m_{F'} - m_F = +1$ and g_{ij}^{-} is zero

$\mathcal{A}_{ij}$	$\lvert F'=0, m_{F'}=0\rangle$	$\lvert 1,1\rangle$	$\lvert 1,0\rangle$	$\lvert 1,-1\rangle$
$\lvert F=1, m_F=+1\rangle$	$\sqrt{\frac{1}{6}}$	$\sqrt{\frac{5}{24}}$	$-\sqrt{\frac{5}{24}}$	-
$\lvert F=1, m_F=0\rangle$	$\sqrt{\frac{1}{6}}$	$\sqrt{\frac{5}{24}}$	-	$-\sqrt{\frac{5}{24}}$
$\lvert F=1, m_F=-1\rangle$	$\sqrt{\frac{1}{6}}$	-	$\sqrt{\frac{5}{24}}$	$-\sqrt{\frac{5}{24}}$

Table 3.1: The angular part of the dipole matrix elements $\mathcal{A}_{ij}$ for the transition between $|i\rangle$ and $|j\rangle$. With these numbers, the Rabi frequencies are $\Omega_{ij} = \mathcal{A}_{ij} \cdot \Omega_0$. For a transition with $\Delta m = +1$ the cavity coupling constant reads $g_{ij}^{+} = \mathcal{A}_{ij} \cdot g_0$. For transitions with $\Delta m = -1$ it is $g_{ij}^{-} = \mathcal{A}_{ij} \cdot g_0$, and $g_{ij}^{\pm} = 0$ in all other cases. The indices i and j refer to the states $|F, m_F\rangle$ and $|F', m_{F'}\rangle$. The electronic parts of the coupling constant and Rabi frequency are chosen to be $g_0/2\pi = 6.7\,\mathrm{MHz}$ and $\Omega_0/2\pi = 14.7\,\mathrm{MHz}$. Note that in our scheme only $\sigma^{\pm}$ transitions are accessible. The $\mathcal{A}_{ij}$ for the non-relevant π transitions are shown in grey.

unless $\Delta m = -1$. For the relevant transitions, the Rabi frequencies also read $\Omega_{ij} = \mathcal{A}_{ij} \cdot \Omega_0$. For our calculation, we have chosen realistic values for the electronic part of the atom-cavity coupling and of the peak Rabi frequency, i.e. $g_0/2\pi = 6.7\,\mathrm{MHz}$ and $\Omega_0/2\pi = 14.7\,\mathrm{MHz}$.
To include the spontaneous decay of the involved excited states, we extend the Liouville operator (3.5) to

$$\begin{aligned}\hat{L}[\hat{\rho}] = \; & \textstyle\sum_{i,j}\Big[\gamma_{ij}\Big(2|i\rangle\langle j|\hat{\rho}|j\rangle\langle i|\Big)\Big] - \sum_j \gamma_j\Big(|j\rangle\langle j|\hat{\rho} + \hat{\rho}|j\rangle\langle j|\Big) \\ & +\kappa\Big(2\hat{a}\hat{\rho}\hat{a}^\dagger - \hat{a}^\dagger\hat{a}\hat{\rho} - \hat{\rho}\hat{a}^\dagger\hat{a} + 2\hat{b}\hat{\rho}\hat{b}^\dagger - \hat{b}^\dagger\hat{b}\hat{\rho} - \hat{\rho}\hat{b}^\dagger\hat{b}\Big),\end{aligned} \tag{3.9}$$

where γ_{ij} is the transition strength of the decay channel from $|j\rangle$ to $|i\rangle$ and γ_j the total polarization decay rate of the excited state $|j\rangle$, including transitions to other levels, such as the $F = 2$ ground state.
The extension of the model makes the prediction of the emission probability more difficult. The influence of certain atomic bare states increases or decreases depending on their distance from the virtual excited level of the Raman transition. Only from a numerical simulation of the scheme, using the master equation Eq. (3.6) with the extended Hamiltonian and Liouvillian from Eq. (3.7-3.9), do we gain more insight into the physical processes.

In Fig. 3.4 the calculated emission probability is shown as a function of the cavity-atom detuning Δ_{ca}, with the blueish lines again showing emission probabilities for σ^- photons and reddish lines for σ^+ photons. Compared to Fig. 3.3, the symmetry around $\Delta_{ca} = 0$ is lost. At this frequency the probabilities for σ^+ and σ^- photon emissions differ from one another although the cavity is in resonance with an atomic transition. This can be qualitatively understood because the influence of the $F' = 1$ state becomes larger the

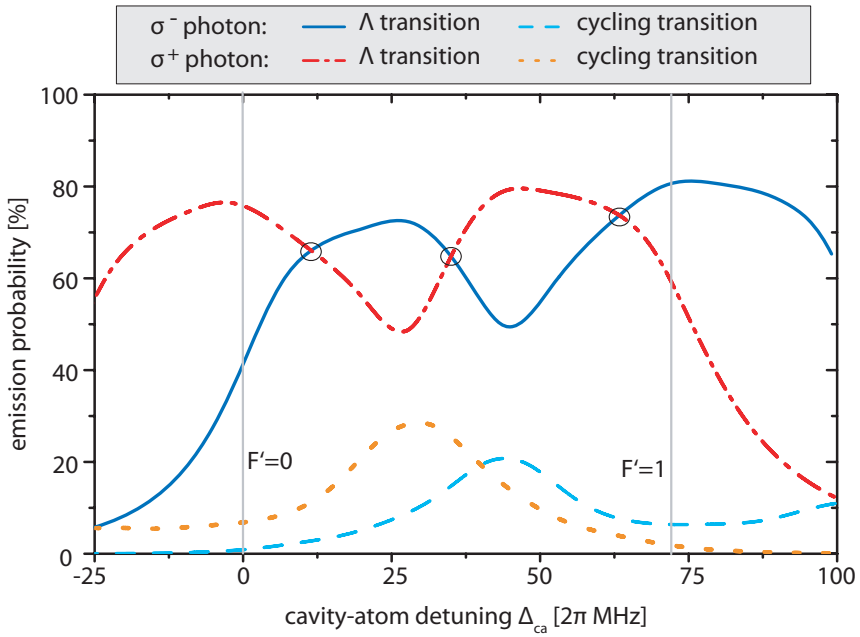

Figure 3.4: **Polarized photons from a ^{87}Rb atom: Photon emission probability** as a function of the cavity-atom detuning Δ_{ca} with respect to the transition from $|0\rangle$ to $|e\rangle$. The ground state $F = 1$ and the excited states $F' = 0$ and $F' = 1$ are incorporated in the simulation, as well as their spontaneous decay. The vertical grey lines indicate zero detuning to the transitions from $|F = 1, m_F = 0\rangle$ to $|F' = 0, m_{F'} = 0\rangle$ and $|F = 1, m_F = 0\rangle$ to $|F' = 1, m_{F'} = 0\rangle$, respectively. The probabilities for the generation of σ^+ and σ^- photons are equal for three values of the detuning. They now deviate from a symmetrical picture with respect to the atomic resonances (grey vertical lines) since the transition amplitudes via both excited states interfere.

closer the virtual exited level is to this state. For a cavity-atom detuning of $\Delta_{ca} = 0$, the virtual excited level is between $F' = 0$ and $F' = 1$ for the σ^+ process, but below the $F' = 0$ level for σ^-. Moreover, the detuning of the virtual level with respect to the atomic bare states determines the sign of the transition amplitudes. Therefore the two possible paths of the Raman transition (via $F' = 0$ and $F' = 1$) interfere either constructively or destructively.

Although the former symmetry is lost, three cavity-atom detunings Δ_{ca} are found where the efficiencies for σ^+ and σ^- photon production are equal. One is almost half-way between the two atomic resonances, and the other two are close to the $F = 1$ to $F' = 0$ and $F = 1$ to $F' = 1$ resonances. For the latter two cavity frequencies, the probability for generating a photon although the atom is starting from the wrong initial state is below 7% (Fig. 3.4, dashed lines). This is an upper limit for the probability of generating a second photon after a first emission, if the process is started from

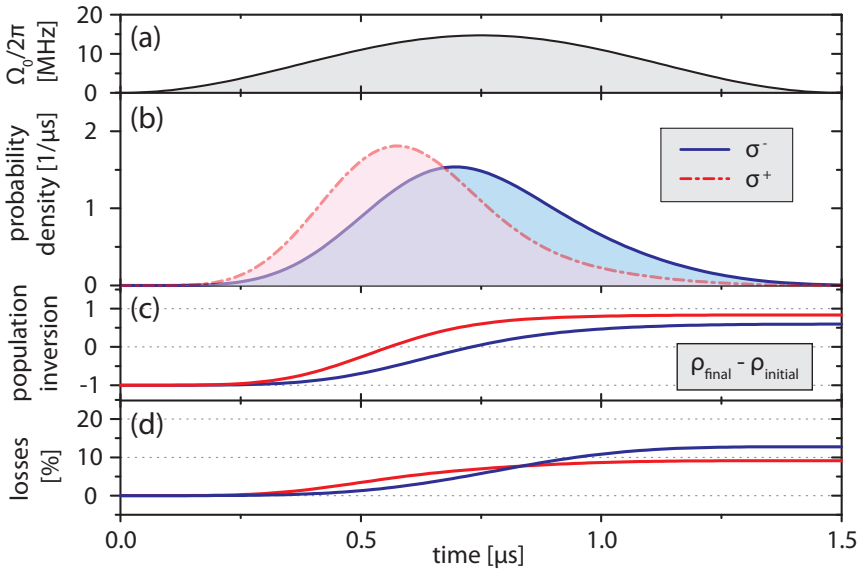

Figure 3.5: **Polarized photons from a ^{87}Rb atom: Time evolution of the system** at $\Delta_{ca}/2\pi = 63.2\,\mathrm{MHz}$: The probability density of the photon emission has a different shape for the emission of a σ^- photon (black) and σ^+ photon (grey). The final population inversion of the atomic state differs from 1 because of losses due to spontaneous emission into uncoupled states, i.e. $|F = 2\rangle$ and $|F = 1, m_F = 0\rangle$. This loss probability is about 10% per shot.

the correct initial state.
As an example, with $\Delta_{ca}/2\pi = 63.2\,\mathrm{MHz}$, the equal probabilities for σ^+ and σ^- photon emission reach a maximum of 74%. The time evolution of the system for this detuning is shown in Fig. 3.5. The atom is exposed to the same pump pulse (shape and amplitude) for both directions of the Raman process. Although the probabilities for σ^+ and σ^- photon emission are equal, the envelopes of the emitted photons differ, as can be seen in the probability-density plot. In fact, the virtual levels for the two transitions are not at the same energy and their transition amplitudes have different values.
Differences in the two processes can also be seen in the population transfer from the initial to the final state, see Fig. 3.5 (c). It is more successful for σ^+ photons, which indicates that the losses to non-coupled states are higher when a σ^- photon is generated. Note that these losses never exceed 15% see Fig. 3.5 (d). Furthermore, from the low probability of the wrong transition to take place (below 7% for cycling transition), we conclude that the starting conditions for a photon of opposite polarization are always met once a first photon has been emitted. Therefore generating a sequence of photons of alternating polarization seems feasible.
Now it is shown that one can address either the $|-\rangle$ to $|+\rangle$ or the $|+\rangle$ to $|-\rangle$

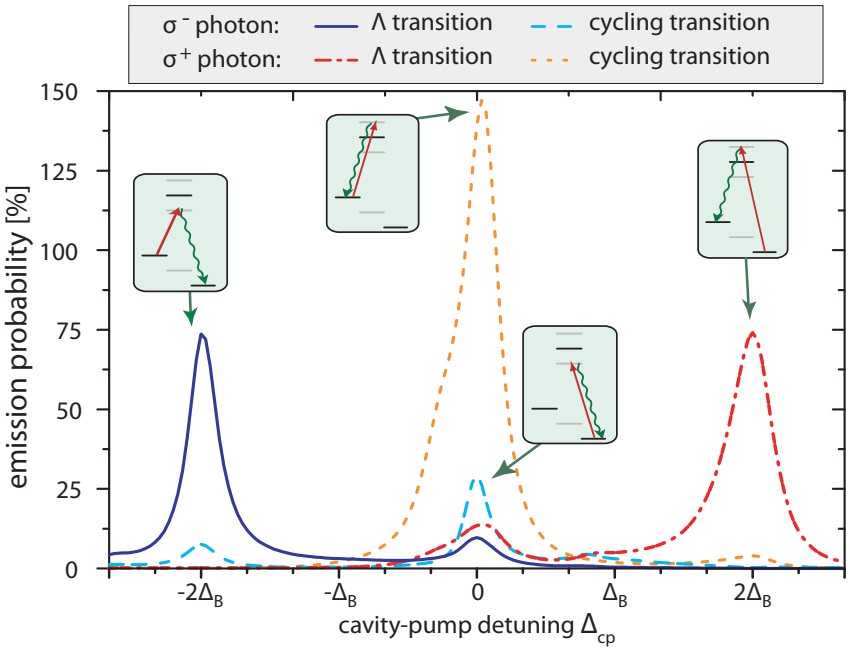

Figure 3.6: **Dependency of the photon emission probability on the frequency difference between pump laser and cavity.** The cavity-atom detuning is set to $\Delta_{ca}/2\pi = 63.2\,\mathrm{MHz}$. The Raman resonance of laser and cavity at $\pm 2\Delta_B$ leads to sharp peaks in the photon emission probability for Λ transitions while cycling processes are only visible around $\Delta_{cp} = 0$.

transition by choosing the appropriate pump laser frequencies. For a fixed cavity-atom detuning of $\Delta_{ca}/2\pi = 63.2\,\mathrm{MHz}$, Fig. 3.6 shows the calculated emission probabilities as a function of the cavity-pump detuning, Δ_{cp}. Again the pump laser Rabi frequency follows a $\sin^2(\pi t/1.5\,\mu\mathrm{s})$ pulse amplitude as shown in Fig. 3.5. As expected, maxima are found in the photon emission probability whenever Raman resonance conditions are met. Starting from state $|-\rangle$, the emission probability for σ^- photons shows a maximum at a pump laser detuning of $\Delta_{cp}/2\pi = -2\Delta_B = -30\,\mathrm{MHz}$, and similarly starting from state $|+\rangle$ a maximum is found in the emission probability of σ^+ photons for $\Delta_{cp}/2\pi = +2\Delta_B = +30\,\mathrm{MHz}$. The emission probability amounts to 74%, as discussed before. Note that the Rayleigh scattering peak at $\Delta_{cp} = 0$ dominates the spectrum. It exceeds 100% emission probability, since the pump laser hits the cavity resonance and the atom undergoes a cycling transition, see insets. For this reason, more than one photon per pulse can be emitted. These cycling transitions are more pronounced for σ^+ photons, since here the virtual excited level of the Raman transition is closer to a real atomic level ($\Delta_{ca}/2\pi = 63.2\,\mathrm{MHz}$ and $|F' = 1, m_{F'} = 0\rangle$ is at $2\pi \cdot 72\,\mathrm{MHz}$). To guarantee single-photon emission in our scheme, transitions where two photons are possibly emitted have to be avoided. Since the width

of the resonances depends on the cavity decay rate 2κ, the magnetic field has to be chosen high enough to ensure that the separation of the transition lines significantly exceeds 2κ. For the Zeeman splitting considered here, the Raman resonances are well resolved, see Fig. 3.6, and the scheme is not disturbed by cycling transitions.
In summary, with the pump frequency being switched from one pulse to the next in a way that the Raman transition is either driven from $m_F = +1$ to $m_F = -1$ or vice versa, a stream of photons with alternating polarization is expected from our atom-cavity system with ^{87}Rb. No time-consuming repumping will be needed, so that the photon-emission rate increases. The simulations show that equal efficiencies can be obtained for the production of σ^+ and σ^- photons when an appropriate cavity-atom detuning is used. The efficiency is 74% for a cavity resonance close to the $F = 1$ to $F' = 1$ transition frequency. The losses to other states are small, which guarantees that after a first emission, the atom is well prepared to produce a subsequent photon.

3.2 Setup

The scheme described above has been realized in our system (79). In Fig. 3.7 a schematic overview of the setup is given. As described in section 2.2, ^{87}Rb atoms are dropped from a magneto-optical trap (MOT) through the TEM_{00} mode of the high finesse optical cavity. A pair of current carryingcoils is used to produce a magnetic field pointing along the cavity axis. While falling through the resonator, the atoms are illuminated by laser pulses from the side, which together with the cavity drive Raman transitions between the $|+\rangle$ and $|-\rangle$ states. The σ^+ and σ^- photons that emerge from the cavity are rotated with a wave plate to H and V polarization, respectively. A polarizing beam splitter (PBS) then directs them into either a 3 m long or a 270 m long fiber both leading to the detection setup consisting of a non-polarizing beam splitter (NPBS) and an avalanche photo-diode (APD) in each output port. The cavity frequency has been fixed to the transition from $F = 1$ to $F' = 1$, that means $\Delta_{ca}/2\pi = 72\,\mathrm{MHz}$. This has historical reasons, since the experiment was actually done before the simulations. The relevant parameters for the system at these settings are $(g_{\max}, \kappa, \gamma)/2\pi = (3.1, 1.25, 3.0)\,\mathrm{MHz}$.
Details about the setup are given in the following subsections. First, in subsection 3.2.1, it is discussed what magnetic field strength is necessary to realize the scheme and how this field is applied to the atoms. Then, in subsection 3.2.2 the laser system is described. Subsection 3.2.3 explains the preparation of atoms in the $F = 1$ ground state and subsection 3.2.4 describes the detection setup.

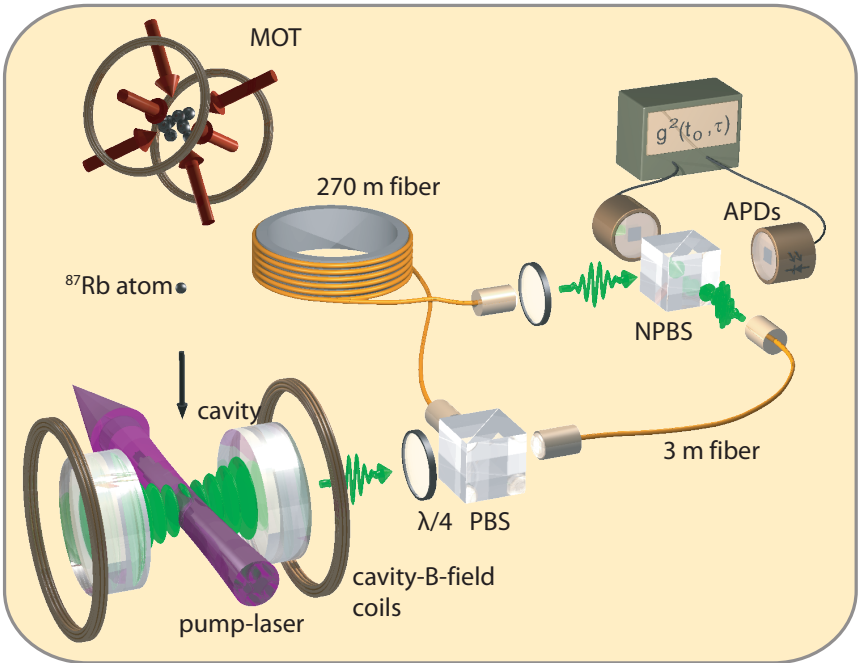

Figure 3.7: **Setup of the Zeeman photon pistol.** As atoms fall from a magneto-optical trap (MOT) through the cavity, they are illuminated with the pump laser from the side to generate photons. The photons are directed through one of two fibers by a polarizing beam splitter (PBS), the long 270m fiber acting as a delay line. Photons emerging from the fibers can interfere at a beamsplitter (NPBS), and are detected by a pair of avalanche photodiodes (APDs).

3.2.1 Magnetic field

To be able to separately address the individual transitions from $|-\rangle$ to $|+\rangle$ and vice versa without accidently driving other processes, the splitting of these levels has to be sufficiently large, i.e. much larger than the cavity linewidth. Here, we choose a Zeeman shift of 14 MHz, which is about the same magnitude as in the simulations. The energy shift of the Zeeman sublevels $|\pm 1\rangle$ is $\Delta_B = \mp |g_L| \mu_B B$, with $\mu_B = 9.27 \cdot 10^{24}$ J/T being the Bohr magneton and $g_L = -1/2$ being the Landé factor for the $F = 1$ hyperfine ground state of ^{87}Rb. This results in a frequency shift of the atomic levels of $\Delta_B / 2\pi\hbar = 0.7\,\mathrm{MHz/G} \cdot B$.
The magnetic field is produced by a pair of coils placed around the vacuum chamber. The coils consist of 2 mm thick copper wires and each coil has 58 windings. Because of the limited space, these coils could not be placed in Helmholtz configuration which would result in a more homogeneous field along the coil axis. The radius of the coils is 85 mm and they have a distance of 300 mm. The magnetic field expected in the center of the coils in the cavity region is $B = 1.03\,\mathrm{G/A} \cdot I$. With a current of 19.4 A, a magnetic

field of about 20 G results, thus inducing a splitting of the Zeeman levels of 14 MHz. Calculations of the field that builds up inside the coils show that, within the cavity volume, variation of the field is very small (117). The coils are placed directly on the big view ports of the cavity chamber, therefore missalignment of the axis relative to the cavity axis is expected to be minimal.
The magneto-optical trap (MOT) does not run properly with such a strong magnetic field in the cavity region. Therefore the cavity-B-field has to be switched on and off in each experimental cycle. With a P-MOSFET circuit the field can be switched in about 6 ms. Since the atoms need 200 ms to travel the distance from the MOT to the cavity, it is sufficient to turn the coils on only shortly before the atomic cloud arrives. After the cloud has passed the cavity, the coils are switched off again.

3.2.2 Laser system

As described in subsection 2.3.1 the main laser system of the experiment consists of two diode lasers from *Toptica*, see Fig. 3.8. The *DLX110* serves as light source for all transitions on the D_2 line of ^{87}Rb that start from the $F = 2$ hyperfine ground state. These beams are the MOT cooling beams as well as the optical pumping beam which prepares the atoms in the $F = 1$ ground state (details in subsection 3.2.3). To access both transitions easily the laser is stabilized on the crossover resonances in the saturated absorption signal of Rubidium which lies half-way in between the resonances from $F = 2$ to $F' = 1$ & $F' = 3$. Acousto-optical modulators (AOMs) are used to turn the beams on and off. Since one needs to detune the MOT beams by several linewidths with respect to the resonance $F = 2$ to $F' = 3$ during the optical molasses, a double-pass configuration ($\leq 2 \times 106$ MHz) is used[(i.)]. The frequency of the optical pump beam is not shifted during the experiment, it just needs to be turned on and off, therefore an AOM in single-pass configuration (1×54.9 MHz) is used.
The other diode laser *DL100* serves as light source for all transitions on the D_2 line of ^{87}Rb starting from the $F = 1$ hyperfine ground state. It is stabilized on the crossover resonance between the $F = 1$ to $F' = 1$ & $F' = 2$ resonances. This laser serves as repumper for the MOT, is used to stabilize the cavity and for the pump laser pulses. The MOT repumper does not need to be changed in frequency during the experiment, the ability to turn it on and off is sufficient. Therefore a single-pass AOM (1×78.6 MHz) is used. For the cavity and for the pump laser pulses one needs the ability to detune the frequency by a large value while the experiment is running. Therefore

[(i.)] In single-pass configuration the angle of the diffracted beam depends on the frequency of the acoustic wave, in a double-pass configuration this angle is equal and opposite in the second-path through the crystal and the beam always has the same pointing independent of the frequency of the acoustic wave.

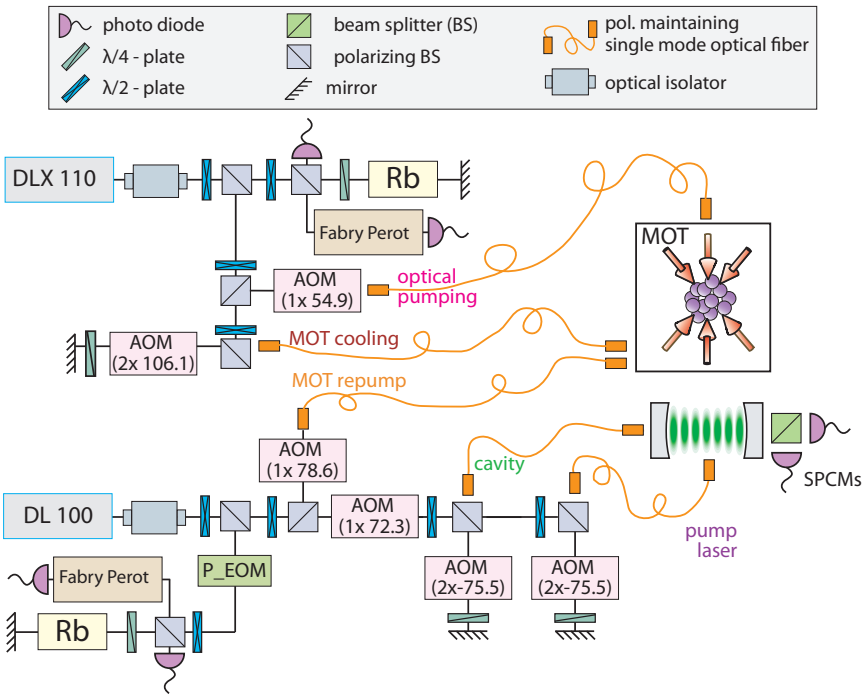

Figure 3.8: **Laser system.** The DLX laser covers all beams needed starting from the $F = 2$ and the DL100 all starting from the $F = 1$ level. The frequencies of the different beams are shifted by AOMs in single path ($1\times$) and double paths ($2\times$) configuration. More details are given in the text.

an AOM ($1 \times 72.3\,\mathrm{MHz}$) in a single-pass is used to shift the frequency such that the desired frequencies can now be reached with AOMs in double-pass configuration ($2 \times 75.5\,\mathrm{MHz}$). The pump laser is switched from pulse to pulse between $-2\Delta_B$ and $+2\Delta_B$. The switching is done with an RF switch contolled by a TTL signal.
To keep the alignment in the experiment independent of the AOM pointing, the laser beams are all fed into polarization maintaining fibers and sent to the experiment. The intensities of all beams are checked before each experimental cycle and are corrected if necessary.

3.2.3 Preparing the atoms

Atoms coming from the MOT and the optical molasses are typically in the $F = 2$ hyperfine ground state. Since the scheme relies on the fact that the atoms are either arriving in the $F = 1, m_F = +1$ or in the $F = 1, m_F = -1$ state, an optical pumping stage is added. The optical pumping beam illuminates the atoms from above - *vertically* - while they travel from the MOT to the cavity. The beam is elliptically polarized and drives the $F = 2$ to $F' = 1$ transition. Atoms are excited as long as they are in the

$F = 2$ hyperfine ground state, once they are in the $F = 1$ state they will no longer scatter photons. In the $F = 1$ hyperfine ground state the atoms are distributed among all magnetic sublevels.

3.2.4 Detection

The detection setup shown in Fig. 3.7 allows one to characterize the source. First, the single-photon nature is investigated when a fraction of photons is sent through only one fiber, while the other fiber is blocked. In this case a Hanbury Brown & Twiss setup allows for a measurement of the intensity correlation as well as the detection-time distribution of the emitted photons. Second, the mutual coherence of pairs of σ^+ and σ^- photons is characterized in a time-resolved two-photon interference experiment (77; 106), where both fibers are used. The long fiber then acts as a delay line for a first photon and the subsequently generated second photon is sent through the short fiber. Hence, the two photons arrive at the beam splitter simultaneously, and can interfere.
A similar setup has already been used in (77; 106) to do the first time resolved two-photon interference experiments. Since in this new scheme no repumping of the atom is necessary between photon emissions, the sequence of pump pulses can be applied more rapidly and so a shorter delay line is used. Therefore the whole setup was rebuilt in a black box on a movable table using detectors with a lower dark count rate.

Wave plates and the polarizing beam splitter

The photons emerging from the cavity should all have a well defined polarization of σ^+ or σ^-. After the cavity this circular polarization is rotated into linear polarization to be able to direct the two photons along different paths. To do so, in principle a $\lambda/4$ plate would be sufficient to adjust the circular polarization to any linear polarization. But a test with the cavity stabilization light that is transmitted through the cavity shows us that it is not that easy: Light that enters the vacuum chamber and the cavity with perfect circular polarization reaches the wave plate with elliptical polarization. Mirrors after the cavity are thought to be responsible for this polarization change. With a combination of a $\lambda/4$ plate (here: changes elliptically polarized light to linearly polarized light) and a $\lambda/2$ wave plate (here: rotates the linearly polarized light to linear H or V polarization), however, this effect can be compensated for. For the compensation the stabilization light is used, since it should be affected in the same way as the generated photons[(ii.)]. Then a polarizing beam splitter (PBS) can be used to direct

[(ii.)] The possibility that the polarization of the stabilization light is changed before it enters the cavity is very low since after a linear polarizer and a $\lambda/4$ plate it goes directly through a vacuum viewport onto the input mirror of the cavity.

them along different paths, according to their polarizations.

Towards the detection

The two different fiber paths are two polarization-maintaining single-mode optical fibers, one long (270 m), the other short (3 m). The long fiber acts as a delay line in a two-photon interference experiment where the two photons from one source are overlapped on a beam splitter. To perfectly overlap them, the pump pulse sequence has to perfectly match the delay introduced by the fiber, because only if the two photons arrive at the same time on the beam splitter can the two-photon interference occur. Here, the long fiber delays the photons by 1.34 μs with respect to the travelling time through the short fiber. This time is long enough to generate the next photon.
The transmission of the short fiber is 72% and the transmission of the long fiber is 61%. This includes the coupling efficiencies into the fiber and damping inside the fiber (-3.5 dB/km@780 nm). After each fiber a $\lambda/2$ wave plate and a linear polarizer[(iii.)] are used to adjust the polarization of photons after each of the fibers, so their polarization can be chosen to be parallel or perpendicular to each other.

Non-polarizing beam splitter

The output modes of the fibers are recombined at a 50:50 non-polarizing beam splitter (NPBS), and photons are then detected at each output port by avalanche photodiodes (APDs). When aligning the NPBS it is important to check that the reflection and transmission of the beam splitter is truly polarization independent for both inputs. The reflection and transmission of one polarization changes slightly for different incident angles on the cube. Equal refection (transmission) probability for all polarizations can be adjusted by changing the incidence angle of the beam by rotating the NPBS cube along a vertical axis. Typically, a perfect 50:50 separation of the beam cannot be achieved for all polarizations. In this setup a transmission of 47% and a reflection of 53% could be achieved. Losses in the cube can be regarded separately, they are about 2% on each input port and for each polarization.

Characterizing the interferometer

The above described interferometer with an imbalanced length of its two arms can be characterized with a second-order interference experiment, which is the interference of electro-magnetic fields (106). Since the two fibers define the spatial mode of the photons impinging on the beam splitter, one

[(iii.)] Polarcor polarizer from *Corning*, extinction better than 1/10000 and transmission about 90%.

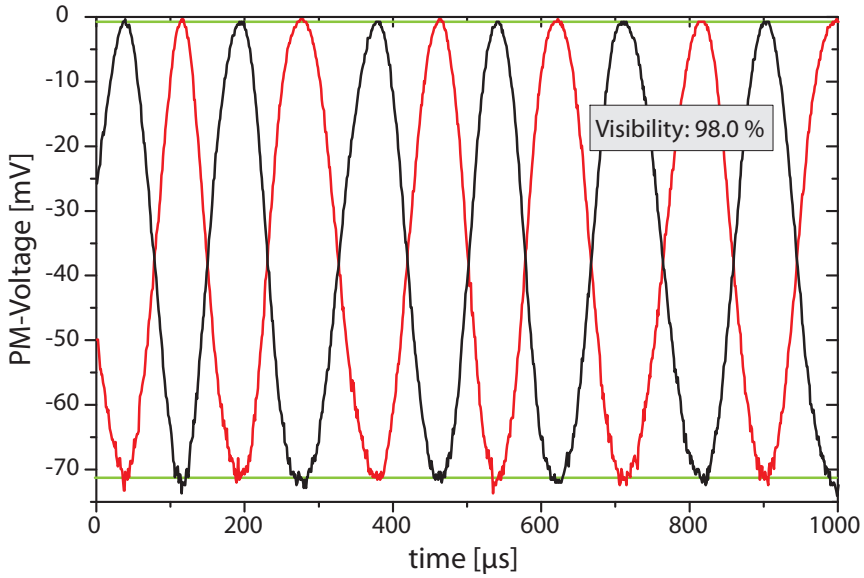

Figure 3.9: **Characterizing the interferometer setup with second order interference:** the visibility of the interference fringes on the two photo multiplier tubes is optimized. Both show a visibility of 98% which will result in a maximum contrast of 96% in the fourth order interference experiment.

can use a laser beam coupled into both fibers to adjust the interferometer. To monitor the overlap of the two beams coming from the two fibers, two photo multiplier tubes (PMT) are used: With flip mirrors in each output port of the NPBS the light is send onto the PMTs[(iv.)]. By scanning the frequency of the laser, the relative phase of the light leaving the two fibers changes as a function of time and one observes interference fringes on the PMTs. The goal is to optimize the visibility of these fringes for both PMTs to assure that the two beams are in the same spatial mode after the NPBS and are indistinguishable. As shown in Fig. 3.9 the second order fringes have a visibility of 98% in both PMTs. This value limits the fourth order interference (interference of electro-magnetic field intensities - photons) to a maximal possible visibility of 96% (106).

Photon detection and data acquisition

Single photon counter modules (SPCMs) of part number *AQR-16* from *Perkin & Elmer* are used to detect the single photons. These detectors have a high quantum efficiency of about 47% and a dark count rate that is lower than 25 counts/s. Such a low dark count rate is important for this

[(iv.)] In one arm the light is directly send onto the PMT after the NPBS, in the other arm after travelling a distance of about 1 m, which is much longer than the distance from the NPBS to the APDs.

experiment since it has a very low event rate. Most of the time no atom is present in the cavity and no photons are produced.
As mentioned in subsection 2.3.2, for data acquisition a *FAST ComTec P7888* multi-event time digitizer is used. This card has a time resolution of 1 ns when only two of the four input channels are used, otherwise the time resolution is 2 ns. Compared to the length of a typical single-photon wave packet produced from our source this is sufficient for analyzing the data. A third input channel is used to record the timing information: A trigger signal is sent from the function generator that runs the pump-pulse sequence.

3.3 Single photons

In this section the single photon properties of the system are tested. First, in subsection 3.3.1 it is shown that the magnetic field that has been applied is sufficiently large to individually address the transitions from $|+\rangle$ to $|-\rangle$ and vice versa. Then the experimental sequence for generating a stream of single photons with alternating polarizations is described in subsection 3.3.2. In subsection 3.3.3 the result of a photon correlation measurement is shown, proving the single-photon nature of the source. In subsection 3.3.4 the efficiency of the photon generation process is discussed.

3.3.1 Scanning the pump laser frequency

Here, we experimentally locate the Raman resonances for the transition from $|+\rangle$ to $|-\rangle$ and vice versa. The cavity is fixed on the transition from $|F = 1, m_F = 0\rangle$ to $F' = 1, m_{F'} = 0$. In Fig. 3.10 the number of detected photons is plotted against the pump laser detuning with respect to the cavity frequency. Each data point contains the averaged number of photons emitted from three dropped atomic clouds. Here, both fibers were open to collect as much photons as possible, regardless of their polarization. Note that in this measurement the pump laser frequency is not alternated, all pump pulses have the same frequency.
For pump laser pulses that are linearly polarized perpendicular to the cavity axis the pump laser couples to σ^+ and σ^- transitions. Three resonances are observed: The largest resonance is found for zero detuning between pump laser and cavity. This is much larger than the other resonances, because a cycling transition can be driven, resulting in multiple photons from a single atom. The two other resonances are found symmetric to zero. One resonance is found at a pump laser frequency of $-2\Delta_B = -28\,\mathrm{MHz}$. There the pump laser drives a transition from $|-\rangle$ to $|+\rangle$ resulting in the production of a σ^- photon (see inset). As the initial and final state are different, each atom can only emit one photon. A second resonance is found at a pump pulse frequency of $2\Delta_B = +28\,\mathrm{MHz}$. Then a transition from $|+\rangle$ to $|-\rangle$ is

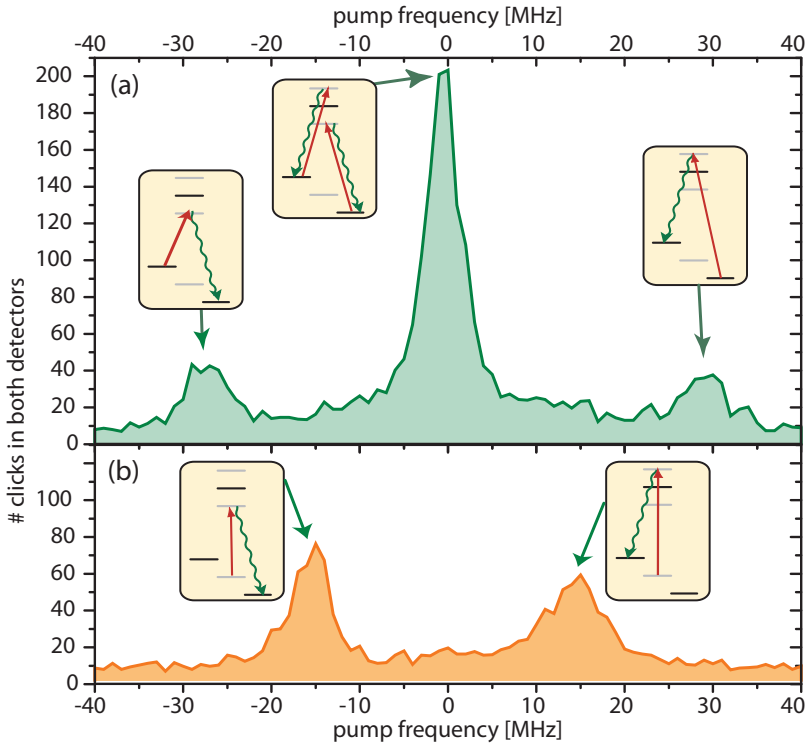

Figure 3.10: **Number of photons as a function of pump laser-cavity detuning.** When the polarization of the pump beam is chosen perpendicular to the cavity axis (a) three resonances are observed. The largest resonance is at zero detuning where cycling transitions are induced. The other two are the Raman resonances at $\pm 2\Delta_B = \pm 28\,\mathrm{MHz}$ where a transition from $|\pm\rangle$ to $|\mp\rangle$ takes place and a σ^+/σ^- photon is generated. With a polarization of the pump beam parallel to the cavity axis (b), two resonances are found at $\pm\Delta_B = \pm 14\,\mathrm{MHz}$. All resonances are well-resolved and can hence be addressed individually.

driven which results in a σ^+ photon emission. These resonances are well-resolved, so they are individually addressable by choosing the appropriate pump laser frequency.

For pump laser pulses that are linearly polarized parallel to the cavity axis, the pump laser couples only to π transitions. Therefore we only find resonances when the atom starts in the $|0\rangle$ state and the pump laser is detuned by $\pm\Delta_B$ from the cavity. Indeed, resonances are found at $-14\,\mathrm{MHz}$, where a transition from $|0\rangle$ to $|+\rangle$ is driven and σ^- photons can be generated and at $+14\,\mathrm{MHz}$ where a transition from $|0\rangle$ to $|-\rangle$ is driven and σ^+ photons can be generated. From the fact that no resonance is observed at zero pump laser detuning, we can conclude that the polarization of the pump beam is well defined, since otherwise cycling transitions would be induced there.

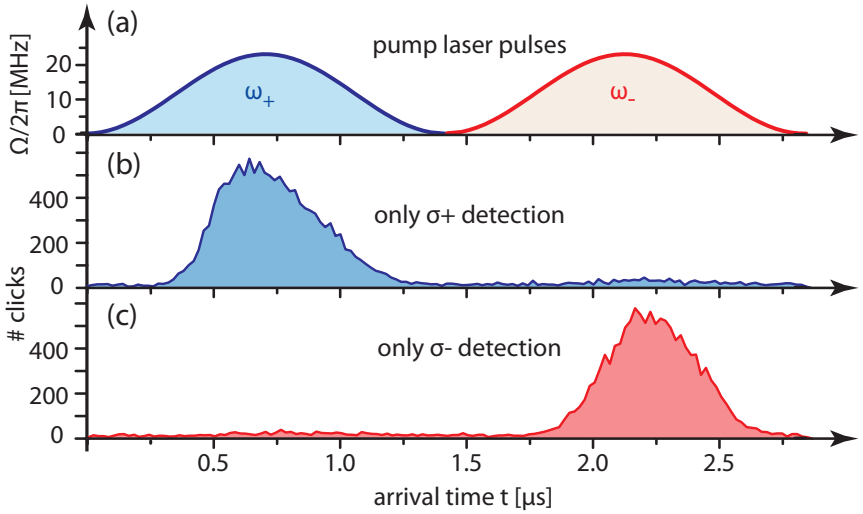

Figure 3.11: **Detection time distribution.** Photon characteristics observed with only one path to the NPBS open. (a) Pump pulse sequence. The first pulse labelled ω_+ has a detuning of $\Delta_{pc}/2\pi = 28\,\mathrm{MHz}$, the second ($\omega_-$) $\Delta_{pc}/2\pi = -28\,\mathrm{MHz}$. (b)/(c) Photon detection time distribution for σ^+/σ^- photons, showing they are predominately detected during the corresponding ω_+/ω_- pulses.

3.3.2 Experimental sequence

The positions of the Raman resonances have been determined experimentally and since they appear at the expected position, we could conclude that the Raman processes are driven as predicted. But from the measurement above no information is revealed over the polarization of the emitted photons. It is left to be shown, that the frequency of the pump laser pulse determines the direction of the Raman process, and therefore the polarization of the emitted photons. To demonstrate this, the detection time distribution of photons of the two circular polarizations is observed separately. Figure 3.11(a) shows the repeated sequence of pump laser pulses of alternating frequency. The detunings of the pump pulses are chosen to be $\Delta_{pc} = \pm 2\Delta_B$. The pulses are labelled ω_+ and ω_- indicating that the laser frequency is such that a σ^+ or σ^- photon should be emitted, respectively. The envelope of the pump pulses follows an $\Omega_0 \sin^2(\pi t/t_p)$ function with parameters $(\Omega_0/2\pi, t_p) = (24\,\mathrm{MHz}, 1.42\,\mu\mathrm{s})$.
To be able to separately observe the two polarizations, the long fiber is closed, and only photons passing through the short fiber are detected. By rotating the wave plates after the cavity we can direct only σ^+ or only σ^- polarized photons into the short fiber. In figure 3.11(b) the wave plate is oriented such that only σ^+ photons are detected, in figure 3.11(c) only σ^-. It can be clearly seen that the number of σ^+ photons generated during the ω_+ pulse is much larger ($\sim$ 20 times) than during the ω_- pulse. Similarly

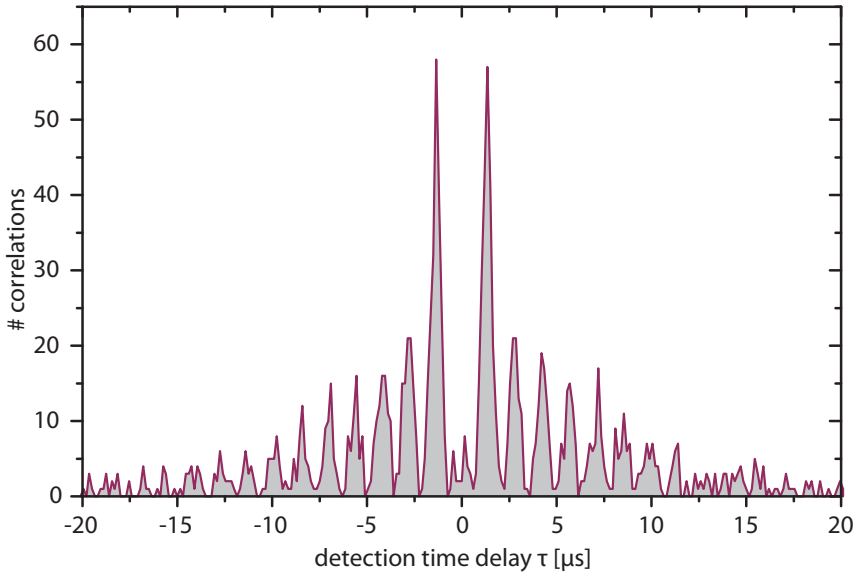

Figure 3.12: **Autocorrelation of the photon stream.** Measurement of the intensity correlation between the two detectors (both polarizations are detected). The missing peak at $\tau = 0$ results from the single photon nature of the source. Data are binned in 150 ns intervals.

for σ^- photons, the number of detected photons during the ω_- pulse is ~ 30 times larger than during the ω_+ pulse. In both cases approximately the same number of atoms pass through the cavity and the total numbers of detected photons are similar.

3.3.3 Photon statistics

To prove that only single photons are generated, an intensity correlation measurement is performed. For this measurement photons of both polarizations have to be detected, so the wave plate after the cavity is oriented such that the PBS acts as a 50:50 beam splitter for each polarization. Only the short fiber is opened now and after the fiber the NPBS randomly distributes the photons among the two avalanche photodiodes. Figure 3.12 shows the number of coincidences in the two detectors recorded as a function of the time delay τ between the detections. The comb-like structure reflects the periodicity of the driving pump laser pulses, whereas the width of the comb is a consequence of the limited interaction time of a falling atom with the cavity mode. But the most interesting feature in the correlations is that the peak at time $\tau = 0$ is missing, proving that a single photon source has been realized. The probability of obtaining multiple photons is 2.5% that of single photons. This includes the contributions related to dark counts and to the fact that more than one atom could be present in the cavity. From the

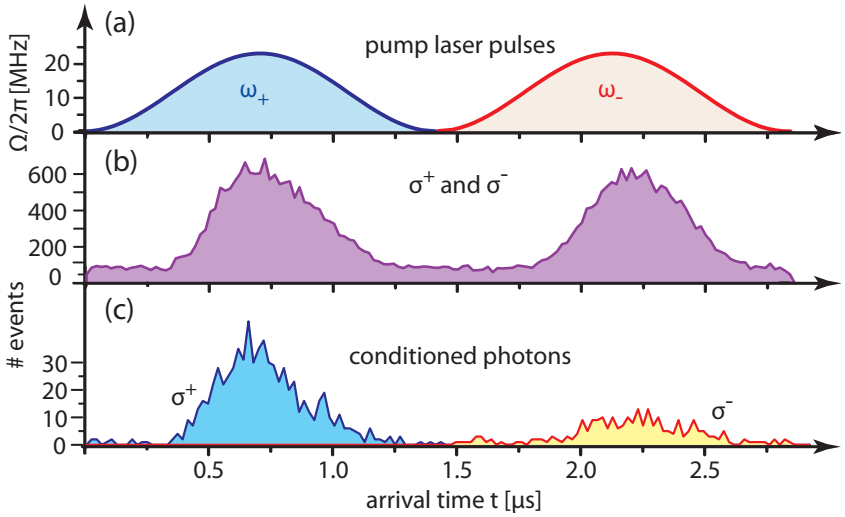

Figure 3.13: **Arrival time distribution.** Photon characteristics observed with only one path to the beam splitter open. (a) Pump pulse sequence as in Fig. 3.11. (b) Detection time distribution of all photons through the short fiber. (c) Detection time distributions for photons conditioned on a detection during the previous pulse. The probability of detecting a σ^+ photon after a σ^- photon is much larger than the probability of the opposite case.

correlation measurement, the atomic flux through the cavity can be deduced (122; 118). In the measurement shown above, a flux of about 2 atoms/ms has been found. That means most (93.2%) of the time the cavity is empty, in about 6.5% of the time only one atom is found in the cavity and in 0.3% of the time more than one atom is present in the cavity. Therefore, the many-atom contribution is sufficiently small.
Another interesting feature in Fig. 3.12 is that the peaks at $\tau = \pm 1.42\,\mu$s are at least 2.5 times higher than all the others. It seems that a pair of subsequent photons is more likely to be obtained than three or more photons in a row. To understand this, the conditioned efficiencies have to be considered.

3.3.4 Conditioned efficiencies

A measure of the efficiency of the photon generation process can be obtained by considering the probability for a photon emission given that a photon was detected during the previous pump pulse. This condition ensures that an atom is coupled to the cavity and that it is in the correct internal state to emit a photon in the subsequent pulse. The measurement described in subsection 3.3.3 has been analyzed in this sense. Hence, a click in one of the detectors can be attributed with 67% probability to the presence of an atom, which is deduced from the amount of background photons and of dark

counts in both detectors.
In Fig. 3.13 (b) the detection time distribution is shown relative to the pump pulse sequence (a), when 50% of each polarization is directed through the short fiber. In (c) conditioned detection time distributions are presented: Displayed are the detection time distributions of photons detected during the ω_+ pump pulse ($t < 1.42\,\mu$s), given that a photon was detected during the previous ω_- pulse, and the detection time distributions of photons detected during the ω_- pulse ($t > 1.42\,\mu$s), given that a photon was detected during the previous ω_+ pulse. Immediately obvious is the large difference in the number of these conditioned σ^+ and σ^- photons. Taking into account the dark count rate and the overall photon detection efficiency, two conditional probabilities for generating a photon inside the cavity are obtained: $p(\sigma^+|\sigma^-) = 41\%$ for generating a σ^+ photon after a σ^- photon, and $p(\sigma^-|\sigma^+) = 13\%$ for generating a σ^- photon after a σ^+ photon.
The large difference in these conditional probabilities explains why in the autocorrelation in Fig. 3.12 the pair of peaks at $\pm 1.42\,\mu$s are more pronounced than the other peaks. The back and the forth process depend on each other. For example, after generating a σ^+/σ^- photon, there is a 13%/41% probability to generate a σ^-/σ^+ photon. In contrast, to generate another σ^+/σ^- photon in the next but one pulse, a σ^-/σ^+ photon must be emitted beforehand.
This asymmetry between the two polarizations occurs already in the simulations. But, the simulations that take the effect of additional levels into account show an asymmetry in the opposite sense (see Fig. 3.4, vertical line at $F' = 1$). As the atoms are not fixed in the cavity, the coupling of a given atom to the cavity and pump laser cannot be specified, but are at most Ω_0 and $g_{\max}$. However, for all reasonable coupling values σ^- photons are supposed to be produced with a higher efficiency than σ^+ photons, contrary to the measurement.
In addition to the large difference between the conditional probabilities, the envelopes of the two photons of different polarizations differ from each other in the experiment (Fig. 3.11) and in the simulation. In the measurement, the peak of the σ^+ envelope occurs earlier in the pump laser pulse than the peak of the σ^- envelope which is more symmetric and follows more the shape of the pump pulse. This asymmetry is also visible in the simulations. Even though the simulations shown in Fig. 3.5 were done at a different atom cavity detuning where the efficiencies are equal, one can see that the envelopes are not necessarily the same. For parameters used in the experiment this effect is even more pronounced. There, the peak of the σ^- photon occurs earlier than the peak of the σ^+ photon with respect to the pump laser pulses.

3.3.5 Experiment versus simulations

As discussed above, the results of the experiment and of the simulations differ very much from another. We have put a large effort to find a systematic error in the experiment or in the simulations. It was checked that the lasers for stabilizing the cavity and for the pump pulses were running on the desired frequencies. The definition of σ^+ or σ^- polarization was done regarding the polarization that was emitted from the atom when applying a $\pm 2\Delta_B$ detuned pump laser pulse, respectively. The detection efficiency of the setup was controlled to be the same for both polarizations. In a measurement where the magnetic field was flipped to the opposite direction so that the $|+\rangle$ and $|-\rangle$ levels are shifted in the opposite sense, inverted conditional efficiencies have been observed: Now σ^- photons are more efficiently generated than σ^+ photons. Since the detection setup thereby had not been changed, it proves that the different efficiencies are really related to the level scheme of ^{87}Rb in the magnetic field. Also in the simulation, we could not find an error. One can understand the result of the simulations qualitatively from the signs of the Clebsch-Gordon coefficients. There seems to be an effect that is not included in the simulations that leads to this experimental result. Apart from the discrepancy to the simulations, we could experimentally demonstrate a single photon source that emits single photons of well defined polarization with a very high efficiency.

3.4 Time-resolved two-photon interference

Many quantum information processing (QIP) applications of a single-photon source require indistinguishable photons (33; 80; 97; 98; 123). So far, only the envelopes of the σ^+ and σ^- photons have been regarded, Fig. 3.11 (b&c). But the similarity in the envelopes does not tell anything about the spectral properties of the photons. To test for the indistinguishability of the produced σ^+ and σ^- photons a time-resolved two-photon interference experiment (36; 77; 124) has to be performed. Two photons that simultaneously enter different entrance ports of a 50:50 beam splitter will always leave through the same output port if they are indistinguishable (35; 102; 103; 73). The degree of indistinguishability is determined by measuring the number of coincidences obtained when the photon pairs have parallel polarization compared to the case when they have perpendicular polarization and are thus completely distinguishable.
In this section, the basic idea of the time resolved two photon interference is first reviewed briefly in subsection 3.4.1. Then in subsection 3.4.2 it is discussed how the two photons are superimposed on the beam splitter. The results of the two photon interference are shown in subsection 3.4.3 supplemented by a detailed discussion on the influence of the photon duration and of the pump pulse peak Rabi frequency. The quantum beat experiment in

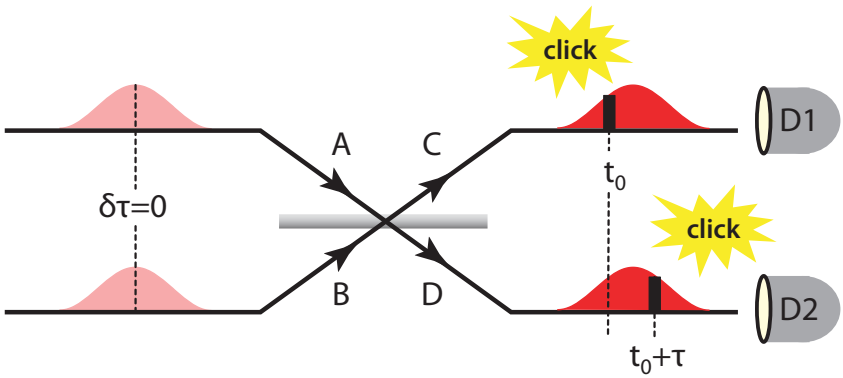

Figure 3.14: **Time-resolved two-photon interference.** The two photons arrive with no time delay ($\delta\tau = 0$) on the beam splitter. In each output port a detector can register a photon with a time resolution that is much faster than the photon duration. The time between the two detections in the different outputs is τ.

subsection 3.4.4 demonstrates that not only the polarization, but also the frequency of the emitted photons can be controlled.

3.4.1 Principle

A time-resolved two-photon interference is only possible when the photons are long compared to the time resolution of the detectors and it can be measured at what time instants within the photon duration the *clicks* occur. This allows now to investigate the two-photon interference as a function of the detection time difference τ of the two photons instead of the time delay between them $\delta\tau$ as in usual Hong-Ou-Mandel (HOM) experiments (35). In our measurements, photons always arrive simultaneously on the beam splitter - the time delay between them is $\delta\tau = 0$. This corresponds to a measurement at the bottom of the HOM dip.
The theory describing the time-resolved two-photon interference can be found in detail in (36; 106; 124) and will only be described briefly here. Let us assume two photons impinging simultaneously on a beam splitter through the input ports A and B, as is shown in Fig. 3.14. The initial state of the system is $|\Psi_{ini}\rangle = |1_A, 1_B\rangle$. The detection process of the photons is quantum mechanically described by annihilation operators. These annihilation operators in the output modes of the beam splitter C and D are linked to corresponding annihilation operators in the two input ports of the beam splitter:

$$\begin{aligned} \hat{a}_C &= \hat{a}_B + \hat{a}_A \\ \hat{a}_D &= \hat{a}_B - \hat{a}_A, \end{aligned} \tag{3.10}$$

where $\hat{a}_A$ and $\hat{a}_B$ are operators that remove photons from inputs A and B respectively.

The detection of a single photon in detector C or D at time t_0 that reveals no which way information projects the system into a superposition state

$$|\Psi_\pm(t_0)\rangle = \hat{a}_{C,D}\,|1_A, 1_B\rangle = (|1_A, 0_B\rangle \pm |0_A, 1_B\rangle)/\sqrt{2} \tag{3.11}$$

depending on which detector clicks. This superposition state now evolves in time until the second photon is detected at a time $t_0+\tau$. If the two photonic modes A and B have a slightly different time evolution, the superposition state will accumulate a relative phase $\varphi(\tau)$. This can happen for example, when the two photons have a frequency difference Δ: In this case the relative phase will evolve as $\varphi(\tau) = \Delta \cdot \tau$ and the new state reads

$$|\Psi_\pm(t_0+\tau)\rangle = (|1_A, 0_B\rangle \pm e^{i\varphi(\tau)}\,|0_A, 1_B\rangle)/\sqrt{2}. \tag{3.12}$$

Since it depends on the phase $\varphi(\tau)$ which detector clicks, this state can be monitored by the subsequent photon detection. The probabilities that the second photon is found in detector C or D are given by

$$\begin{aligned} \langle\Psi_\pm|\,\hat{a}_C^\dagger \hat{a}_C\,|\Psi_\pm\rangle &= \tfrac{1}{2}(1 \pm \cos\varphi(\tau)) \\ \text{and } \langle\Psi_\pm|\,\hat{a}_D^\dagger \hat{a}_D\,|\Psi_\pm\rangle &= \tfrac{1}{2}(1 \mp \cos\varphi(\tau)). \end{aligned} \tag{3.13}$$

In a photon correlation experiment this relative phase $\varphi(\tau)$ can be observed in the number of coincidences in detectors C and D as a function of the detection time delay τ. A few examples for Gaussian shaped single-photon wave-packets of duration δt (half-width at $1/e$ maximum, HW1/eM) are shown in Fig. 3.15. As a reference the coincidene probability expected for two completely distinguishable photons

$$P_\perp(\tau) = \frac{1}{2\sqrt{\pi}} e^{-\tau^2/T_1^2} \tag{3.14}$$

is shown in grey, e.g. for photons with perpendicular polarizations. The grey peak has a width of $T_1 = \delta t$ (HW1/eM). For indistinguishable photons, the two modes A and B experience the same time evolution and the relative phase is zero for all detection time differences ($\varphi(\tau) = 0$). Therefore, from Eq. (3.13) we conclude, that if the first photon has been detected in detector C or D, then the second photon will always be detected in the same detector, i.e. C or D, respectively. That means the coincidence probability is zero for all τ. In contrast, when the two superimposed photons have a frequency difference $\Delta = 3\pi/\delta t$ an oscillation of the coincidence probability will be observed with frequency Δ, see Fig. 3.15 (b). Note that the oscillation always has a minimum at the center $\tau = 0$, it follows from the relation

$$P_\parallel(\tau) = P_\perp(\tau) \cdot [1 - \cos(\Delta \cdot \tau)]. \tag{3.15}$$

In Fig. 3.15 (c) and (d) examples are shown where the Fourier transform-limited single-photon wave-packets have a Gaussian distribution of their

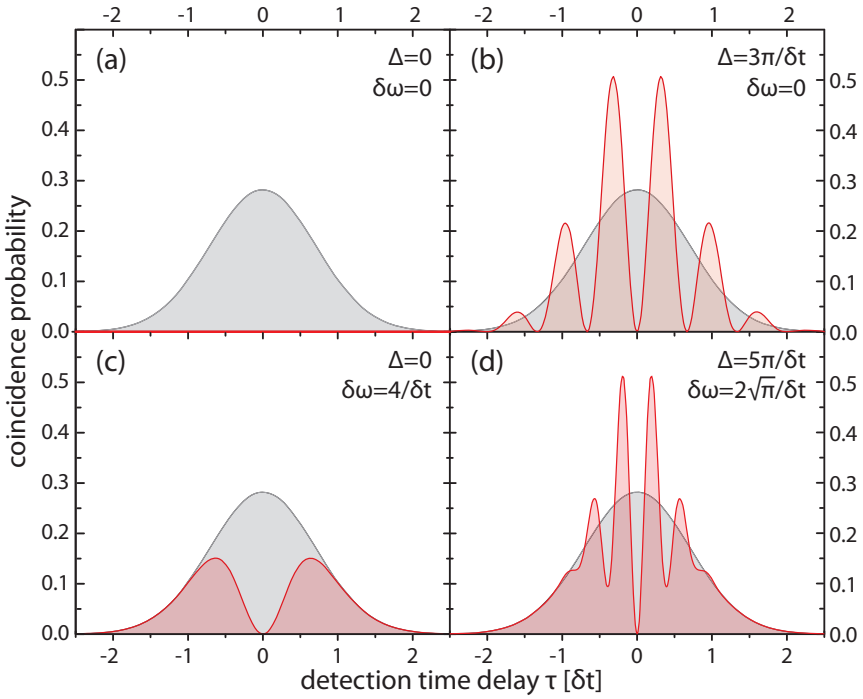

Figure 3.15: **Calculated coincidence probability.** As a reference the expected signal for distinguishable photons with Gaussian envelopes of duration δt are shown in grey. (a) For indistinguishable photons, the relative phase of the modes is always zero, no coincidences occur, see red line. (b) If photons have a frequency difference $\Delta = 3\pi/\delta t$, then the coincidence probability oscillates with $[1 - \cos(\Delta \cdot \tau)]$. (c) A jitter in the difference frequency with a width of $\delta\omega = 4/\delta t$ leads to a dephasing of the two photons. A dip of the width $T_2 = 2/\delta\omega$ occurs that reflects the mutual coherence time of the two photons. (d) If photons have different midfrequencies ($\Delta = 5\pi/\delta t$) in addition to their frequency jitter ($\delta\omega = 2\sqrt{\pi}/\delta t$), the coincidence probability oscillates within the dip. Note that at $\tau = 0$ the coincidence probability is always zero.

midfrequencies of width $\delta\omega$. In (c), both photons have the same midfrequency but it jitters with $\delta\omega = 4/\delta t$. Therefore, two photons meeting at the beam splitter can have different frequency differences $\Delta(\delta\omega)$, and for each frequency difference $\Delta(\delta\omega)$ one expects an oscillation as in (b). Integrated over the frequency distribution, these oscillations wash out. However, a dip in the center remains, since all the oscillations have a minimum in the center. One finds a coincidence probability of

$$P_{\parallel}(\tau) = P_{\perp}(\tau) \cdot [1 - \cos(\Delta \cdot \tau) e^{-\tau^2/T_2^2}]. \tag{3.16}$$

Here, the width of this dip T_2 is defined as the mutual coherence time of the photons $T_2 \equiv t_{coh}$, which depends on the frequency jitter $t_{coh} = 2/\delta\omega$ and describes the time after which their phase relation is random. In Fig. 3.15 (d),

in addition to the frequency jitter $\delta\omega = \pi/\delta t$, the two photons also differ in their midfrequencies $\Delta = 5\pi/\delta t$. In all cases, the coincidence probability is zero around $\tau = 0$.
Note that the same results in the coincidence probabilities as in Fig. 3.15 can be obtained in a different model if we assume a jitter in the emission time distribution rather than in the frequency of the photons. Consider transform-limited Gaussian single-photon wave-packets with duration δt that have a fixed midfrequency ($\delta\omega = 0$), so that their mutual coherence time should be infinite, but their emission time distribution jitters with a Gaussian distribution of width $\Delta\tau$. Then, the width of the coincidence probability for distinguishable photons is not simply given by the duration of the photon but by $T_1 = \sqrt{\delta t^2 + \Delta\tau}$. For indistinguishable photons one finds that the dip in Fig. 3.15 (c)+(d) has a width of $T_2 = T_1\delta t/\Delta\tau$ depending on the photon duration and the emission time jitter.
Here, in the time-resolved two-photon interference we define the two-photon visibility V_{2ph} as the reduction of the coincidence probability compared to the case where the photons are completely distinguishable. The two-photon visibility then reads

$$V_{2ph} = 1 - \frac{\int P_{\parallel}(\tau)d\tau}{\int P_{\perp}(\tau)d\tau} \tag{3.17}$$

and is equivalent to the reduction of the coincidence rate at $\delta\tau = 0$ in an usual HOM experiment.

3.4.2 Overlapping two photons on the beam splitter

With the 3 m and 270 m long fibers in the two output ports of the polarizing beam splitter (PBS) open (Fig. 3.7), pairs of subsequently generated photons are superposed on a beam splitter. Since the photons have well-defined polarizations, they can be directed into either the long or the short fiber using the wave plates behind the cavity and the PBS. In the following paragraph it is discussed which photon should be send along which path to maximize the number of two photon events. Afterwards it is explained how a good temporal overlap of the two photons has been achieved.

Directing photons

The possibility to direct photons of opposite polarizations along different paths using a polarizing beam splitter (PBS) is a useful tool as it allows to optimize the number of coincidences. In a two-photon interference experiment, two subsequently emitted photons that are randomly distributed between the two paths will meet in only 1/4 of the cases at the beam splitter (NPBS)[(v.)]. In a chain of photons the probability for each photon to

[(v.)] In the other cases, (1) both photons take the short fiber, (2) both photons take the long fiber, (3) the first photon takes the short path and the second photon the long path.

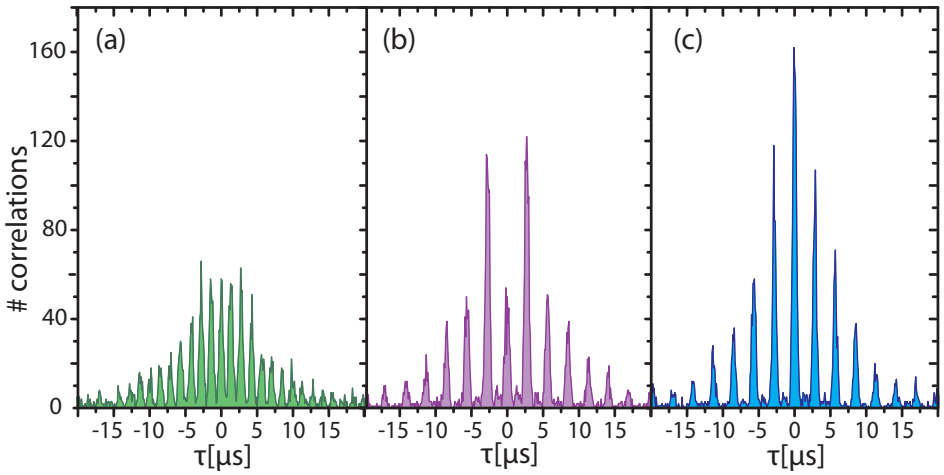

Figure 3.16: **Directing Photons through the long and short fiber:** The PBS acts as simple 50:50 beam splitter for both polarizations, (a) the photons are randomly distributed among the fibers. (b) σ^+ photons are directed through the long fiber and σ^- through the short. (c) σ^- photons are send through the long and σ^+ through the short. About the same number of photons has been detected for all the cases.

meet the previous (or subsequent) photon is 1/4, to meet the previous or the subsequent is 1/2. But if one can direct subsequent photons of opposite polarization, each photon will meet the previous or the subsequent photon at the beam splitter. This method increases the overall efficiency by a factor of two. One simply has to decide whether σ^+ or σ^- polarized photons have to take the long path. The opposite polarization will then automatically be directed along the short path since a polarizing beam cube is used to separate the polarizations.

At first thought, it appears equally efficient to send the σ^+ or the σ^- photons through the long fiber, because in any case both photons are required, so the generation probabilities just multiply. However, this is not the case when there is a large difference in the conditional emission probabilities in comparison to the overall emission of σ^+ and σ^- photons. While the total number of σ^+ and σ^- photons is about the same (Fig. 3.13 (b)), the conditioned efficiencies differ (Fig. 3.13 (c)). Therefore it is preferred to use a σ^- photon as conditioning photon and produce a σ^+ photon with a high conditional efficiency in the next pulse.

The experiment directly proves that this choice is advantageous as seen in Fig. 3.16. With a wave plate behind the long fiber, the polarizations of the two photons are chosen perpendicular to each other such that no interference appears in this measurement. Similar to the measurement of the autocorrelation of the photon stream, the number of coincidences is observed as a

function of the detection time delay between two photons. When the PBS acts as a 50:50 beam splitter for σ^+ and σ^- photons, they are randomly distributed among the two fibers. Figure 3.16 (a) shows the result: Photons arrive at the same time, which constitutes in the peak that appears at $\tau = 0$. This peak in the center is about at the same height as the neighboring peaks. In (b) σ^+ photons are sent through the long fiber and σ^- photons through the short fiber. Now every second peak is missing, since all photons are always detected in every second shot only. The central peak has not gained in height compared to the random splitting. In contrast, the peaks at $\pm 2.84\,\mu$s have risen by a factor of two. Part (c) shows the reversed case where σ^- photons are delayed and σ^+ photons are sent directly onto the NPBS. Again every second peak is missing, but now the number of correlations in the central peak has risen by about a factor of three compared to the other two cases. This difference reflects the strong asymmetry of the conditioned generation probabilities of $p(\sigma^+|\sigma^-) = 41\%$ and $p(\sigma^+|\sigma^-) = 13\%$ in comparison to the overall emission probability of the photons which is about equal. This demonstrates that skillfully directing the photons can significantly raise the number of two photon events.

Timing the sequence

The attentive reader might have noticed, that the run-time difference of the long to the short fiber of $1.34\,\mu$s, does not match the time separation of the pump pulses which has been chosen to be $1.42\,\mu$s. The reason for the choice of a larger separation of the pump pulses is that the midpoint of the σ^+ photon comes earlier with respect to the pump pulse than the midpoint of the σ^- photon. As discussed before, it is advantageous to delay the σ^- photon to maximize the number of two photon events. Therefore, to optimize the overlap of the pulse areas of the two photons the pump pulse separation had to be lengthened. In a detection time distribution measurement where only the long or the short fiber was opened the sequence length has been adjusted. Figure 3.17 shows the resulting temporal overlap of the two photons. This is what we considered as simultaneous arrival used to proceed with the two-photon interference experiment.

3.4.3 Interference

Now both fibers are open and a wave plate at the exit of the long fiber is used to set the relative polarization of the two photons. We count the number of coincidences as a function of the detection time difference, τ. The measurement of photons of perpendicular polarization serves as a reference such that measurements of parallel and perpendicular polarization can be normalized to the number of coincidences in the peaks at $\pm 2.8\,\mu$s.
A typical result is shown in Fig. 3.18. The curves represent the number

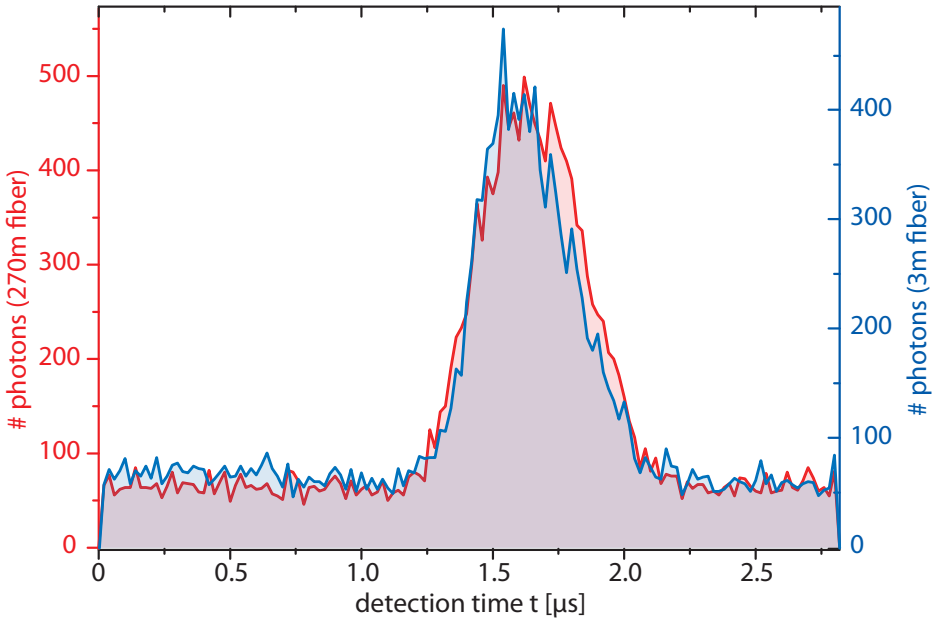

Figure 3.17: **Overlapping the photons in the temporal mode.** The red curve shows the detected photons which are send through the long fiber, i.e. the σ^- photons, whereas the blue curve shows the detected photons which are send through the short fiber only, i.e. the σ^+ photons. The length of the pump pulse sequence of 2.84 μs was chosen such that the midpoint of the photons arrive at the same time.

of coincidences versus τ where the two photons have either parallel or perpendicular polarization at the beam splitter. The dip in the number of coincidences for parallel polarizations around $\tau = 0$ shows that the spatial mode matching of the two interfering photons is good, with the minimum of the dip being consistent with the measured single-photon interferometer visibility of 98%: The visibility is influenced by both the temporal and spatial mode-matching of the two photons at the beam splitter. The combination of the interferometer visibility and the slightly non-identical photon envelopes results in a maximum possible visibility $V_{max} = 94\%$, which would be obtained for the interference of single-photon wave packets with identical temporal evolution.
The two-photon interference visibility is calculated from Eq. (3.17) as $V_{2ph} = 1-(C_{\mathrm{par}}/C_{\mathrm{perp}}) = 0.77$ where $C_{\mathrm{par}}(C_{\mathrm{perp}})$ is the total number of coincidences for $|\tau| < t_p$ when the photons hit the beam splitter with parallel (perpendicular) polarization, respectively. The same information can be obtained from a standard Hong-Ou-Mandel measurement (35) without detection time resolution from the minimum of the *HOM-dip*, but here, more information about the photons is gained. The measurement for perpendicular polarization serves to deduce the time constant $T_1 = 0.18\,\mu$s from Eq. (3.14)

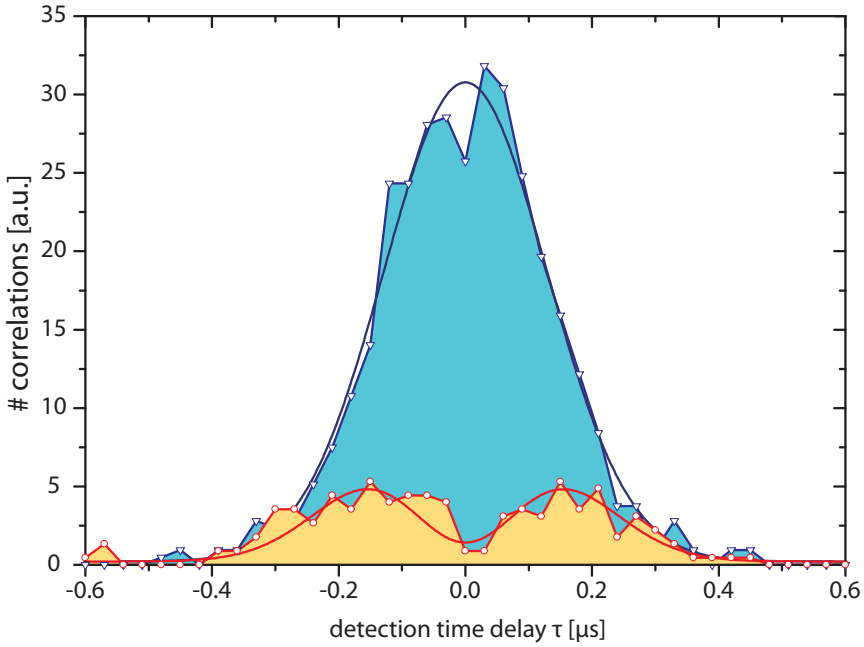

Figure 3.18: **Two-photon interference** for pump pulses of $t_p = 0.71\,\mu$s and $\Omega_0/2\pi = 12\,$MHz. Shown are the normalized number of coincidences as a function of detection time delay τ. The peak area for parallel photons (yellow) is strongly reduced compared to the peak area for perpendicular polarized photons (blue), the two photon visibility is $V = 77\%$. From the fits to the data (blue and red lines), the time constants T_1 and T_2 are obtained.

and from the coincidence probability for parallel polarized photons one can deduce the time constant $T_2 = 0.27\,\mu$s from Eq. (3.16). From the models discussed in subsection 3.4.1 these values of T_1 & T_2 can lead to the conclusion that either the photon duration is $\delta t = 0.18\,\mu$s and the photons have a frequency jitter of $\delta\omega = 2\pi \cdot 1.2\,$MHz or the photons have only a duration $\delta t = 0.15\,\mu$s and their emission time jitters with $\Delta\tau = 0.1\,\mu$s. From the measurement result we can not decide which of the models applies to our photons, most probably they will have both, and the values for frequency jitter and emission time delay lie somewhere inbetween.
This visibility was measured for photons generated with a range of different peak Rabi frequencies Ω_0, and pulse lengths t_p, the results of which are shown in Fig. 3.19. The visibility increases with reduced Ω_0 and shorter pulse durations t_p, with a maximum measured visibility of $V_{2ph} = 77\%$ for $\Omega_0/2\pi = 12\,$MHz and $t_p = 0.71\,\mu$s, see Fig. 3.18 for time resolution.
There are several processes that might affect the photon generation in a way that would make the photons more distinguishable. As discussed before, the atom is more complex than a three-level system, with additional

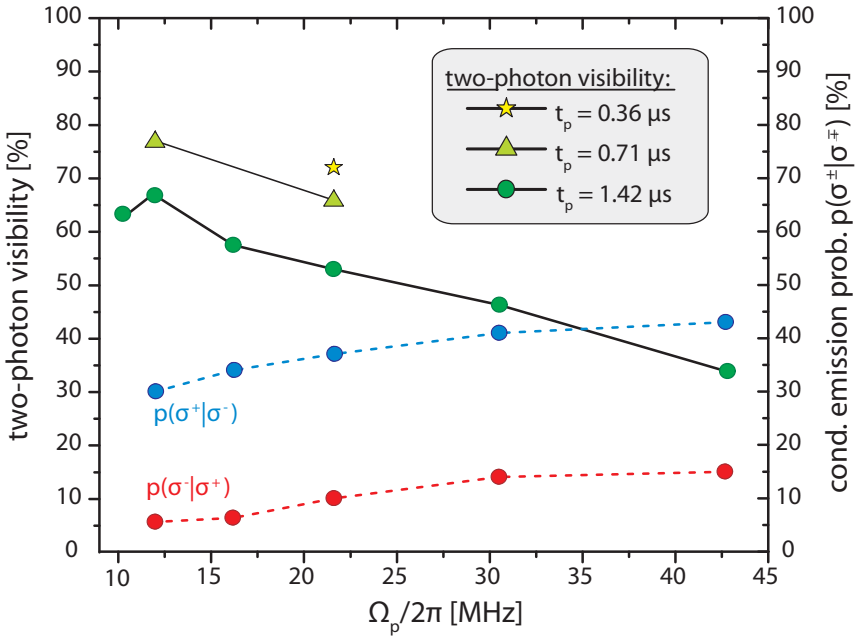

Figure 3.19: **Exploring the parameter space:** visibility and conditioned photon-generation efficiency as a function of pump laser peak Rabi frequency Ω_0 and for various pulse durations t_p. The green/yellow symbols refer to the integrated visibility V of the two photon interference with different symbol shapes encoding different pulse durations. V increases with lower Ω_0 and shorter t_p. The blue and red circles show the conditional probabilities $p(\sigma^+|\sigma^-)$ and $p(\sigma^-|\sigma^+)$, respectively, for generating photons with a pulse duration $t_p = 1.42\,\mu$s.

levels in both the excited and ground states. Off-resonant transitions to these levels lead to frequency broadening with increasing Rabi frequency. In contrast, shorter photons show a better visibility as they have less time to dephase (124). As expected and shown in Fig. 3.19, the conditional probabilities for generating a photon also change with the peak Rabi frequency Ω_0 and pump pulse duration t_p. Unfortunately, conditions which lead to higher visibilities result in lower probabilities for the generation of photon pairs. This reduces the rate at which the source could be used in quantum information processing applications. Of course, it is always possible to increase the visibility by post-selecting only those pairs of coincidences that occur within the dip around $\tau = 0$.

3.4.4 Quantum beat

We have seen that the properties of the generated photons are well controlled. The spatial mode of the photons is defined by the cavity mode and the temporal mode by the shape of the pump laser pulses. In addition it is also possible to control the frequency of the emitted photons to some extent.

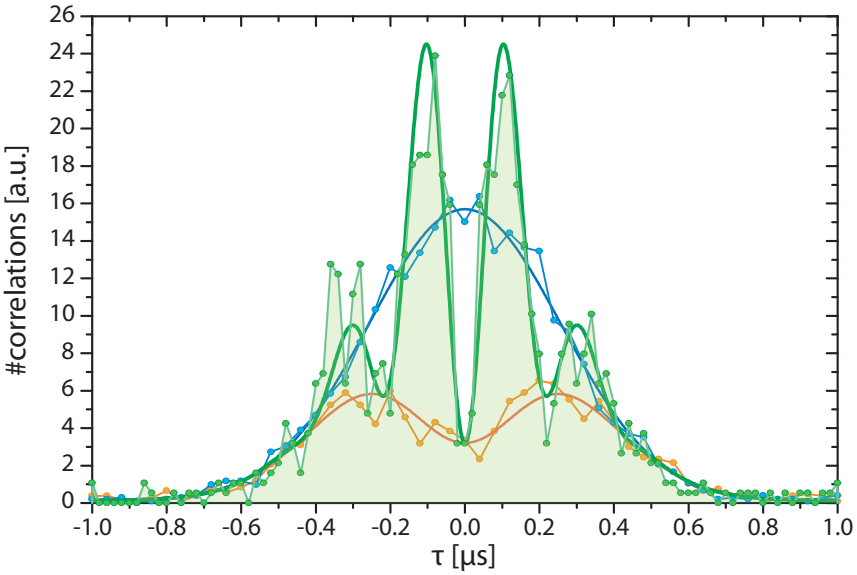

Figure 3.20: **A quantum beat is observed** for two photons that have different frequencies (green). The results from a measurement with photons without frequency difference serve as a reference. The blue curve is measured with photons of perpendicular polarization, the red curve for photons with parallel polarization. Unfortunately in this measurement the second order visibility of the interferometer is reduced caused by a dust particle on one of the mirrors.

Since the photons have to fit into the cavity, the accessible frequency range lies within the cavity linewidth. To produce photons with a frequency difference Δ the pump laser frequency for generating σ^+ and σ^- photons must be detuned by $\pm\Delta/2$ from Raman resonance with the cavity. The frequency of the photons is then defined by energy conservation rules. The initial and final states are the Zeeman substates $|F = 1, m_F = \pm 1\rangle$. If a photon from the pump laser is absorbed, and a photon is emitted into the cavity, this photon has the energy

$$\hbar\omega_{photon} = E_{|initial\rangle} - E_{|final\rangle} + \hbar\omega_{pump}. \tag{3.18}$$

The frequency of the cavity affects the frequency of the emitted photon only in the sense that it will be very unlikely to emit a photon into the cavity mode if the frequency of the photon is far detuned.
The frequency shift of the photons is observed in a time resolved two photon interference experiment, where the frequency difference manifests itself in an oscillation in the number of coincidences depending on the detection time difference τ, (Eq. (3.13)). Here, we have chosen a frequency shift between the photons of $\Delta = 5.1\,\mathrm{MHz}$. In Fig. 3.20 the result of the measurement is shown. No frequency shift is applied to the photons for the blue points and the orange points, which are shown as a reference. The lines are fits to the

data. For the blue curve the polarizations of the photons are chosen to be perpendicular to each other and hence no interference occurs, whereas in the orange curve polarizations are chosen to be parallel. Unfortunately on the day the measurement was taken, the interferometer had a strongly reduced second order visibility[(vi.)] due to a dust particle on one of the mirrors in the interferometer. Therefore the interference does not fully go down to zero at the center. The green curve shows the interference pattern of photons with a frequency difference. From a fit on the data we obtain a measured frequency difference between the photons of 4.5 MHz. The time constants $T_1 = 0.36\,\mu$s and $T_2 = 0.31\,\mu$s were already obtained from the fits to the measurements without frequency difference between the two photons (blue and orange curves), hence the only free parameter for the fit of the green curve is the frequency difference between the photons. The reason for the discrepancy of about 0.6 MHz between measured and induced frequency is not clear. Nonetheless, it is shown that also frequency manipulation is possible in this system.

3.5 Conclusion

In this chapter a scheme for the generation of polarization-controlled single-photons was introduced. First simulations were presented that the implementation in with ^{87}Rb in our cavity setup should produce a stream of photons of alternating polarization. Indeed the experiment has shown, that we can control the polarization of the single photons. The single photon source has reached an efficiency of more than 40% for the production of σ^+ photons. In a time resolved two photon interference experiment we demonstrated that the emitted photons have a very good overlap and lead to a two photon visibility of 77%. A systematic study of the parameter space showed that shorter photons lead to a better two-photon visibility, whereas high peak Rabi frequencies of the pump laser reduce the two-photon visibility.

[(vi.)] The second-order visibility of the interferometer of only 0.9 was obtained from a fit to the data for parallel polarized photons without frequency difference, orange curve in Fig. 3.20.

Chapter 4

Atom-photon entanglement and state mapping

This chapter describes the successful observation of atom-photon entanglement and subsequent state mapping. The triggered emission of a first photon entangles the internal state of the atom and the polarization state of the photon. In contrast to other experiments that observed atom-photon entanglement (70; 72; 125), the atomic state is not examined by using a shelving technique and detecting fluorescence photons. Instead, our scheme maps the atomic state onto the state of a second single photon. Such a state mapping is feasible since the atom-cavity system generates single photons very efficiently in a well defined mode, which outside the cavity can easily be coupled to an optical fiber and focused onto a detector. As a result of the state mapping a pair of entangled photons is produced, one emitted after the other into the same mode. The state of the two photons is analyzed by polarization state tomography, which also probes the prior entanglement between the atom and the first photon.
In this chapter, first, the principle of the scheme is explained in section 4.1. Section 4.2 describes the experimental setup, followed by the presentation and characterization of the experimental sequence (section 4.3). In section 4.4 the entanglement results are discussed. Lastly, the achievements of this chapter are summarized made in a conclusion (section 4.5).

4.1 Scheme

The basic idea of the experimental scheme is explained in subsection 4.1.1, followed by an extension of the description taking into account time dependent atomic or photonic states in subsection 4.1.2. How the entanglement can be observed is discussed in subsection 4.1.3 and in subsection 4.1.4 different entanglement measures are introduced.

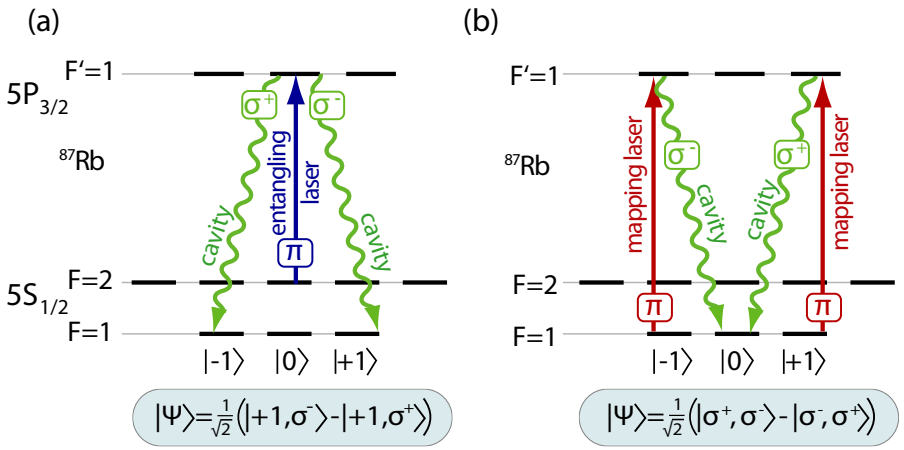

Figure 4.1: **Entanglement and state mapping.** Together with the cavity, laser pulses drive vacuum-stimulated Raman adiabatic passages, first (a) creating an entanglement between the atom and the emitted photon, and then (b) mapping the atomic state onto the polarization state of a second photon. After the pulse sequence, entanglement is now shared between two flying photons, with the atom disentangled.

4.1.1 Basic idea

The entanglement scheme is depicted in Fig. 4.1. A single ^{87}Rb atom is coupled to an optical cavity and prepared in the $|F = 2, m_F = 0\rangle$ state of the $5S_{1/2}$ ground level. With the cavity axis as quantization direction, the cavity supports circularly polarized σ^+ and σ^- polarization modes. A π-polarized laser (resonant with the transition from $F = 2$ to $F' = 1$ of the excited $5P_{3/2}$ level) together with the cavity (resonant with the transition from $F = 1$ to $F' = 1$) drives a vacuum-stimulated Raman adiabatic passage to the $|F = 1\rangle$ state of the electronic ground level, see Fig. 4.1 (a). Two different paths are possible, one to state $|+1\rangle \equiv |F = 1, m_F = +1\rangle$ resulting in the generation of a σ^- photon, and one to state $|-1\rangle \equiv |F = 1, m_F = -1\rangle$ resulting in the generation of a σ^+ photon. After photon emission, the system is in the entangled state

$$|\Psi_{atom,photon1}\rangle = \frac{1}{\sqrt{2}}(|+1, \sigma^-\rangle - |-1, \sigma^+\rangle), \tag{4.1}$$

where the coefficients of the superposition are defined by the transition amplitudes from the $|F = 2, m_F = 0\rangle$ state to the $|+1\rangle$ and $|-1\rangle$ states, which have the same value but opposite signs (121). To map the atomic state onto a second photon a π-polarized laser resonant with the transition from $F = 1$ to $F' = 1$ together with the cavity drives a second Raman adiabatic passage, see Fig. 4.1 (b). The population in state $|+1\rangle$ is transferred to $|0\rangle \equiv |F = 1, m_F = 0\rangle$ and a σ^+ photon is emitted, while the population

in $|-1\rangle$ is also transferred to $|0\rangle$, but in this case a σ^- photon is emitted. The atom-photon entanglement is therefore converted into a polarization entanglement between two photons,

$$|\Psi_{photon2,photon1}\rangle = \frac{1}{\sqrt{2}}(\left|\sigma^+,\sigma^-\right\rangle - \left|\sigma^-,\sigma^+\right\rangle), \tag{4.2}$$

while the atom is disentangled from the photons.
To observe the generated entanglement, the polarization state of the two-photon state has to be analyzed. Since the two photons in our scheme are produced one after the other and they have never interacted, the entanglement between them can only arise from mediation by the atom inside the cavity. This means that verifying the entanglement shared between the two photons also probes the prior entanglement between the atom and the first photon.

4.1.2 Time dependence of the entangled state

As mentioned above, the generated entanglement will be observed via a polarization analysis of the two subsequently emitted photons. Typically, the photons emitted from the atom-cavity system are relatively long single-photon wave-packets with length δt controlled by the duration of the pump laser pulses. They are produced one after the other and hence they will also be detected one after the other. For example, with a polarization analyzer placed behind the cavity, the polarization of the first photon is observed at time t_0 and the polarization of the second photon at time $t_0 + \tau$. This measurement will only give a conclusive result for the two-photon state at time t_0 if neither the remaining atomic nor the photonic state changes after the detection of the first photon during the time τ until the second photon is detected. Such a change can happen when for example, the first detection projects the atom into a superposition state where the two components have different energies and thus evolve differently in time. Note that in this special case the time evolution can be suppressed by detecting the two photons at the same time (τ=0). This could be realized by delaying the first photon using an optical fiber as was implemented in the experiment described in chapter 3.
One important source causing a time evolution is a magnetic field. How it influences the atomic and photonic state will be discussed in the following paragraphs.

B-field parallel to the cavity

When applying a constant magnetic field B along the cavity axis, the degeneracy of the atomic states $|+1\rangle$ and $|-1\rangle$ is lifted by an amount $-\hbar\Delta_B$ and $+\hbar\Delta_B$, respectively. The value of the Zeeman shift Δ_B is given in Eq. (3.1)

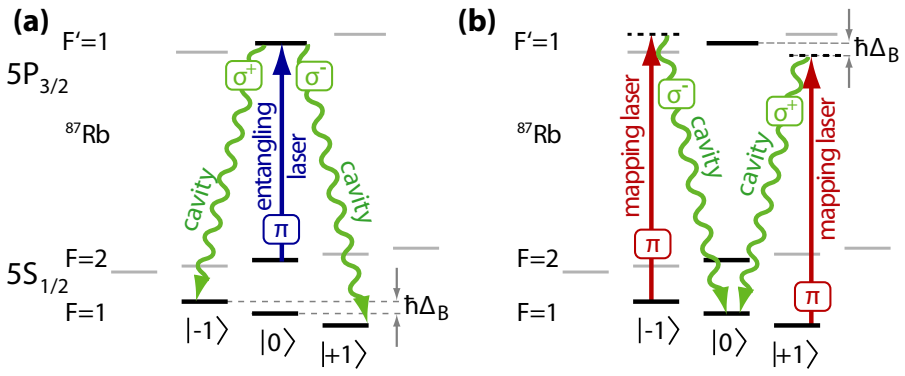

Figure 4.2: **Entanglement and state mapping in the presence of a magnetic field along the cavity.** (a) Entangling and (b) mapping transition. The atomic levels are shifted by the Zeeman effect and the emitted photons have different frequencies corresponding to their polarization. The levels are shifted opposite to the frequencies of the photons. Hence, the entangled state is not influenced because both product states contributing to the superposition have the same total energy.

and is proportional to the magnetic field strength B. Our scheme then generates photons with frequencies linked to their polarizations, see Fig. 4.2. Specifically, σ^- photons have higher frequencies than σ^+ photons. Nonetheless, this has no consequence for the time evolution of the entangled state, Eq. (4.1), since both parts of the superposition state have the same total energy - the frequency difference of the photons matches the (frequency) shift of the atomic states in such a way that they cancel each other. This holds true after the mapping process, since in addition to the state of the atom which is mapped onto the polarization of the second photon, the information about the energy of the atomic state is transferred onto the photon. Again the σ^- photons have higher frequencies than the σ^+ photons.
However, a frequency insensitive detection of the first photon at time t_0 in a basis consisting of a combination of σ^+ and σ^- e.g. with linear diagonal polarization $|D\rangle \equiv \frac{1}{\sqrt{2}}(|\sigma^+\rangle + i\,|\sigma^-\rangle)$, projects the atomic state into a superposition of $|+1\rangle$ and $|-1\rangle$. The energy difference of the atomic levels then leads to a different time evolution of the two states. For instance, if the photon is measured to be in state $|D\rangle$, then the atom is projected into the state

$$|\Psi_{atom}(t)\rangle = \frac{1}{\sqrt{2}}(e^{i\Delta_B t}\,|+1\rangle - ie^{-i\Delta_B t}\,|-1\rangle). \tag{4.3}$$

Subsequent state mapping transfers this state into the photonic state

$$|\Psi_{photon2}(t)\rangle = \frac{1}{\sqrt{2}}(e^{i\Delta_B t}\,|\sigma^+\rangle - ie^{-i\Delta_B t}\,|\sigma^-\rangle), \tag{4.4}$$

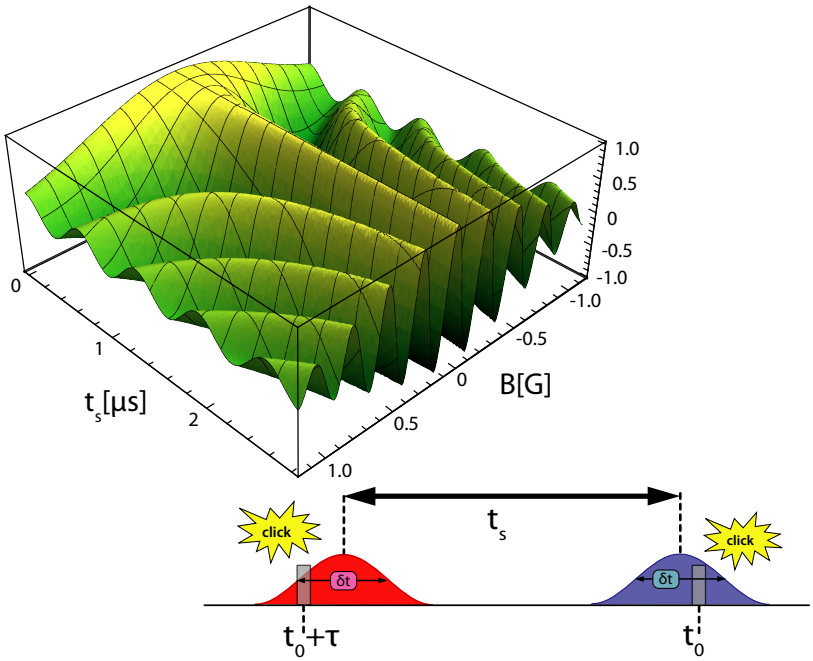

Figure 4.3: **Calculated contrast** C_{DA} for photons pairs measured in the D/A-basis as a function of the time distance between entangling and mapping pulse t_s and the magnetic field strength B. Single photon wave-packets are considered to have Gaussian shaped envelopes with $\delta t = 0.3\,\mu$s (FWHM).

which continues rotating until the second photon is detected at a time $t_0+\tau$. The total rotation angle depends on the time separation between the two photon detections τ and the Zeeman splitting Δ_B. The time τ can be influenced by adjusting the time separation between the entangling and the mapping pulses t_s. However, the photon wave-packets have a finite duration of δt, and the measurement process will collapse these wave packets onto a certain time instant which can not be controlled. Thus the detection time delay can only be post-selected. Alternatively, for a given time separation t_s and a given photon duration δt, the time evolution can be set with the magnetic field strength.
The state rotation can be observed in the contrast, which is defined as

$$C_{XY} \equiv (P_{|XY\rangle} + P_{|YX\rangle}) - (P_{|XX\rangle} + P_{|YY\rangle}), \tag{4.5}$$

with $P_{|XX\rangle}$ denoting the probability to detect both photons as X polarized (and analogous for $P_{|YY\rangle}$ etc.) in the X/Y-basis. In the diagonal/antidiagonal basis (D/A-basis) one expects a $\cos(2\Delta_B t_s)$ dependence in C_{DA} as is shown in Fig. 4.3, where the calculated contrast is plotted as a function of the magnetic field B and the separation between entangling and mapping pulses t_s. It is considered that the single photon wave-packets have Gaussian en-

velopes with $\delta t = 0.3\,\mu$s (FWHW) duration. The oscillatory behavior of the calculated contrast C_{DA} with varying B-field is a manifestation of the phase rotating at twice the Larmor frequency Δ_B. For increasing field magnitude, the envelope of the oscillation decreases due to the length of the single-photon wave-packets δt - the time interval between two photon detections τ covers a range of possible values and thus the superposition state can evolve by differing amounts during these times.

B-field perpendicular to the cavity

When the magnetic field does not point along the cavity axis but is perpendicular to it, the description of the scheme gets more complex. If we consider the quantization axis to be still along the cavity axis, which is convenient since the detection takes place along this axis, the atomic states defined above are not stationary anymore but precess around the axis of the magnetic field. Specifically, taking into account the rotation matrices (126) one finds that population in $|F = 1, m_F = \pm 1\rangle$ can be transferred into the $|F = 1, m_F = 0\rangle$ state, which is dark, so no second photons will be emitted. In addition, the state preparation by optical pumping would not work efficiently, since the atoms in $|F = 2, m_F = 0\rangle$ are redistributed among the other Zeeman substates by Larmor precession. Therefore, the initial state is not well defined and will lead to false first photon events. In an even worse case the preparation of the initial state $|F = 2, m_F = 0\rangle$ fails and the state $|F = 1, m_F = 0\rangle$ is populated accidentally, e.g. by a transition from $|F = 2, m_F \pm 1\rangle$ to $|F = 1, m_F = 0\rangle$ with a σ^-/σ^+ photon emission. Then the population of the $|F = 1, m_F = 0\rangle$ state can be transferred to the other m_F states leading to false second photons. In all such cases, the population transfer takes place between the states with the Larmor frequency Δ. Therefore the entanglement should be restored after a full rotation.
To summarize, while a magnetic field along the cavity axis can be used to rotate the atomic state in a controlled way, magnetic fields perpendicular to the cavity must be avoided since they vastly complicate the entanglement scheme.

4.1.3 Observing entanglement

This subsection describes in detail how the entanglement of the polarization states of two photons can be observed. Methods from experiments with entangled photons from parametric down-conversion are adopted to our experiment (127; 128). The down-conversion community has dealt with such problems for many years and they have developed techniques how to quantify the observed entanglement and investigated possible sources of errors.
As mentioned previously, one possibility is to make a full quantum state tomography of the polarization state of the photon pair to reconstruct the

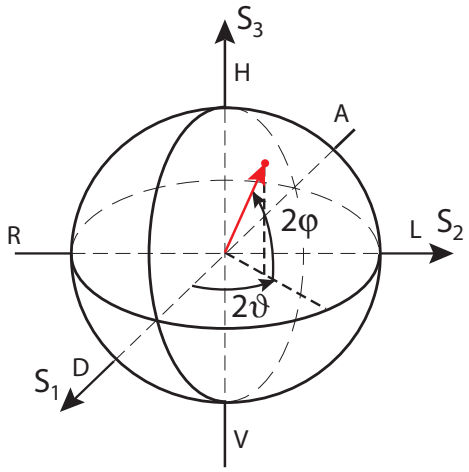

Figure 4.4: **Poincaré sphere:** a point within the sphere represents the polarization state of the light. The radius of the sphere is the total intensity I, the distance of the point from the origin is the degree of polarization p.

density matrix of the two-photon state (129; 130). Other possibilities to verify the entanglement are, for example, measuring non-classical correlations (131) in two different bases or demonstrating the violation of Bell inequalities (132; 133; 134; 135). Performing a full quantum state tomography is a method that requires by far the most measuring time and effort, but only this method will provide the observer with complete information about the two-photon state. Therefore, it is the preferred method here.
The following paragraphs first give a definition of the polarization state of a photon, and then focus on the problem of a polarization measurement of a single photon. Afterwards the full characterization of the polarization state of a single photon is explained, before the discussion is expanded to a two-photon state.

Photon polarization

The polarization state of light can be described by a Stokes vector $u \equiv 1/S_0 \cdot [S_1, S_2, S_3]$ which defines a point in the Poincaré sphere, see Fig. 4.4, where

$$\begin{aligned} S_0 &= I & S_1 &= Ip\cos 2\vartheta \cos 2\varphi \\ S_2 &= Ip\sin 2\vartheta \cos 2\varphi & S_3 &= Ip\sin 2\varphi \end{aligned} \tag{4.6}$$

are the so-called Stokes parameters. The value I is the total intensity of the light, and p is the degree of polarization, $(0 \leq p \leq 1)$. For a single photon the intensity is normalized $(I = 1)$.

Determining the polarization state of a single photon

A polarization measurement projects the photon state onto a certain preselected basis. If this basis is for example horizontal/vertical polarization (H/V), a photon will always be detected with either horizontal or vertical polarization. If its polarization is diagonal or circular, the outcome is horizontally or vertically with equal probability. The measurement only gives a binary result and therefore only reveals partial information about the polarization state of the photon. To get more information about the photon state, one needs more copies of that photon in order to perform multiple measurements in different bases. The precision to which we can specify the state is increasing as more measurements are made. Therefore the polarization state of a single photon can only be estimated from the result of many measurements of an ensemble of identical copies of this photon with different polarizer settings. The Stokes parameters are linked directly to these measurement results:

$$\begin{aligned} S_0 &= P_{|H\rangle} + P_{|V\rangle}, \\ S_1 &= P_{|D\rangle} - P_{|A\rangle} = P_{\frac{1}{\sqrt{2}}(|H\rangle+|V\rangle)} - P_{\frac{1}{\sqrt{2}}(|H\rangle-|V\rangle)} \\ S_2 &= P_{|L\rangle} - P_{|R\rangle} = P_{\frac{1}{\sqrt{2}}(|H\rangle+i|V\rangle)} - P_{\frac{1}{\sqrt{2}}(|H\rangle-i|V\rangle)} \\ S_3 &= P_{|H\rangle} - P_{|V\rangle}, \end{aligned} \tag{4.7}$$

where $P_{|X\rangle}$ is the probability to detect the photon in state X. H/V represents horizontal/vertical polarization, D/A stands for diagonal/antidiagonal polarization and L/R denotes left/right-handed circular polarization.
The state of the photon might not be in a pure state, so it has to be represented by density matrix,

$$\hat{\rho} = \frac{1}{2}\sum_{i=0}^{3} S_i \hat{\sigma}_i. \tag{4.8}$$

The σ_i Pauli spin matrices are:

$$\begin{aligned} \sigma_0 &\equiv \begin{pmatrix} 1 & 0 \\ 0 & 1 \end{pmatrix}, \qquad \sigma_2 \equiv \begin{pmatrix} 0 & -i \\ i & 0 \end{pmatrix}, \\ \sigma_1 &\equiv \begin{pmatrix} 0 & 1 \\ 1 & 0 \end{pmatrix}, \qquad \sigma_3 \equiv \begin{pmatrix} 1 & 0 \\ 0 & -1 \end{pmatrix}. \end{aligned} \tag{4.9}$$

By normalization S_0 is always set equal one. For pure states $\sum_{i=1}^{3} {S_i}^2 = 1$; for completely mixed states $\sum_{i=1}^{3} {S_i}^2 = 0$.
From $P_{|X\rangle} + P_{|X_\perp\rangle} = 1$, with $\mathrm{X/X_\perp} \in \{\mathrm{H/V, D/A, R/L}\}$, the relation $P_{|X\rangle} - P_{|X_\perp\rangle} = 2P_{|X\rangle} - 1$ follows and the polarization state of an ensemble of single photons can be determined in a set of four measurements: First, to normalize the measurements the overall photon-rate n_0 has to be measured. In the following measurements, only H-, D- or R-polarized photons are measured

during the same time interval with the help of wave plates and polarizers, thereby fixing $P_{|X\rangle} = n_X/n_0$.
If instead of a simple polarizer, a polarization dependent beam splitter is used, $P_{|X\rangle}$ and $P_{|X_\perp\rangle}$ are measured simultaneously and the normalization measurement is not needed. Then the measurement is more robust against fluctuations in the photon rate.

Determining the polarization state of two photons

Again, the polarization state of two photons can only be evaluated from an ensemble of identical photon pairs. The polarization state is represented by density matrix

$$\hat{\rho} = \frac{1}{4} \sum_{i,j=0}^{3} S_{i,j}\ \hat{\sigma}_i \otimes \hat{\sigma}_j, \tag{4.10}$$

where $S_{i,j} \equiv S_i \otimes S_j$ are the two-photon Stokes parameters, e.g. $S_{1,3} = (P_{|D\rangle} - P_{|A\rangle}) \otimes (P_{|H\rangle} - P_{|V\rangle}) = P_{|DH\rangle} - P_{|DV\rangle} - P_{|AH\rangle} + P_{|AV\rangle}$. To determine all $S_{i,j}$, the photons have to be measured in all combinations of combined bases, resulting in 3×3 different settings of the measurement bases.
By definition the density matrix is a Hermitian matrix, so it is diagonalizable. In the diagonalized form the eigenvalues λ_i stand for probabilities to detect the photon in the pure state the respective eigenvector represents. Therefore, the eigenvalues must all be positive to represent a physical state. If $\hat{\rho}$ has negative eigenvalues, it is possible to find the most *likely* physical state (128) leading to the measured data.

4.1.4 Entanglement measures for a pair of qubits

A pair of photons in a *pure* state is entangled, if the two photons are not separable - if this state is unfactorizable. Examples of maximally entangled pure states are the Bell states:

$$\begin{aligned} \left|\Phi^+\right\rangle &\equiv (|HH\rangle + |VV\rangle)/\sqrt{2}, \quad & \left|\Psi^+\right\rangle &\equiv (|HV\rangle + |VH\rangle)/\sqrt{2}, \\ \left|\Phi^-\right\rangle &\equiv (|HH\rangle - |VV\rangle)/\sqrt{2}, \quad & \left|\Psi^-\right\rangle &\equiv (|HV\rangle - |VH\rangle)/\sqrt{2}. \end{aligned} \tag{4.11}$$

Mixed states are entangled, if they can not be represented as a mixture of factorizable pure states. However, in order to determine the amount of entanglement present in the system, we have to apply some entanglement measure. In the following three of those entanglement measures are introduced.

Fidelity

The fidelity is a measure of overlap between the observed density matrix $\hat{\rho}_\Psi$ and a reference $\hat{\rho}_1$:

$$F(\hat{\rho}_1, \hat{\rho}_\Psi) = (\mathrm{Tr}\{\sqrt{\sqrt{\hat{\rho}_1}\hat{\rho}_\Psi\sqrt{\hat{\rho}_1}}\})^2. \tag{4.12}$$

The fidelity is not a direct measure for entanglement. It is only valid if the density matrix $\hat{\rho}_\Psi$ reconstructed from measured data is physical (127; 128). If the referenced density matrix $\hat{\rho}_1$ represents a maximally entangled state, a fidelity $F \geq 0.5$ proves that entanglement is present (48), whereas a fidelity $F = 1$ signals that the two states are identical.
Note that the fidelity depends on the state the reconstructed density matrix is compared with. For example, the fidelity of two maximally entangled states $|\Phi^+\rangle$ and $|\Phi^-\rangle$ is zero, since they are orthogonal to each other.

Concurrence

In contrast to the fidelity, the concurrence is a direct measure of the non-classical properties of the quantum state under observation. It was first defined by Hill and Wootters (136; 137). For two qubits (127), first a non-Hermitian matrix $\hat{R}$ is defined by

$$\hat{R} = \hat{\rho}\hat{\Sigma}\hat{\rho}^T\hat{\Sigma} \quad \text{with} \quad \hat{\Sigma} = \begin{pmatrix} 0 & 0 & 0 & -1 \\ 0 & 0 & 1 & 0 \\ 0 & 1 & 0 & 0 \\ -1 & 0 & 0 & 0 \end{pmatrix}, \tag{4.13}$$

where $\hat{\rho}^T$ is the transpose of $\hat{\rho}$ and $\hat{\Sigma}$ is the spin flip matrix. If the eigenvalues of $\hat{R}$ are arranged in decreasing order, $(r_1 \geq r_2 \geq r_3 \geq r_4)$ then the concurrence is defined as

$$C = \mathrm{Max}\{0, \sqrt{r_1} - \sqrt{r_2} - \sqrt{r_3} - \sqrt{r_4}\}. \tag{4.14}$$

A value $C > 0$ proves that entanglement is present, the closer C is to 1, the more entanglement is contained in the system under observation. $C = 1$ represents a maximally entangled state.

Entanglement of formation

Like the concurrence, the entanglement of formation (136; 137) is a direct measure for entanglement. They are monotonically related to each other, the entanglement of formation is calculated as

$$E = h(\frac{1 + \sqrt{1 - C^2}}{2}) \tag{4.15}$$

where $h(x) = -x \log_2 x - (1-x)\log_2(1-x)$. Again, the system under observation is entangled if $0 < E \leq 1$, and $E = 1$ represents a maximally entangled state ($C = 1$). The entanglement of formation "*...is intended to quantify the resources needed to create a given entangled state.*" (137).

4.2 Setup

The setup of our experiment has been described previously in section 2.2. The main parts of the setup have remained, changes had to be made on the laser system, (subsection 4.2.1) and on the detection setup (subsection 4.2.2). In addition to the moderate changes on the laser system, the whole detection had to be rebuilt to enable the polarization analysis of the photons. All the relevant experimental parameters are the same, i.e. the maximum atom-cavity coupling constant $g_{\max}/2\pi = 3.1\,\mathrm{MHz}$, the cavity-field decay rate $\kappa/2\pi = 1.25\,\mathrm{MHz}$ and the dipole decay rate of the atom $\gamma/2\pi = 3.0\,\mathrm{MHz}$ have not changed.

4.2.1 Laser system

The laser setup is very similar to the one used for the polarized single-photons, (subsection 3.2.2). Again the *DLX110* laser covers all frequencies needed starting from the $F = 2$ ground state and the *DL100* covers all frequencies starting from $F = 1$ ground state. In Fig. 4.5 all laser beams that are necessary to realize the scheme are drawn. In contrast to the scheme for polarized photons where the pump laser only came from the *DL100*, here the entangling beam is derived from the *DLX110* and the mapping beam from the *DL100*. In addition, repump and optical pumping beams also have to be sent to the cavity. Hence, four beams have to be superimposed before they are delivered through the same fiber to the cavity to illuminate the atoms from the side. All of these beams are polarized linearly along the cavity axis.

4.2.2 Detection setup

The detection setup is depicted in Fig. 4.6. To explain each element in the setup, the path of a photon emerging from the cavity through the detection setup to the detector is tracked chronologically.

Rotate σ^+/σ^- polarization into H/V polarization

Photons emitted from the cavity are circularly polarized, however, we choose to rotate them into the linear horizontal/vertical (H/V) basis. This has the simple reason that historically the $\lambda/4$ and $\lambda/2$ wave plates to do so were already adjusted from the experiment with the polarized single photons,

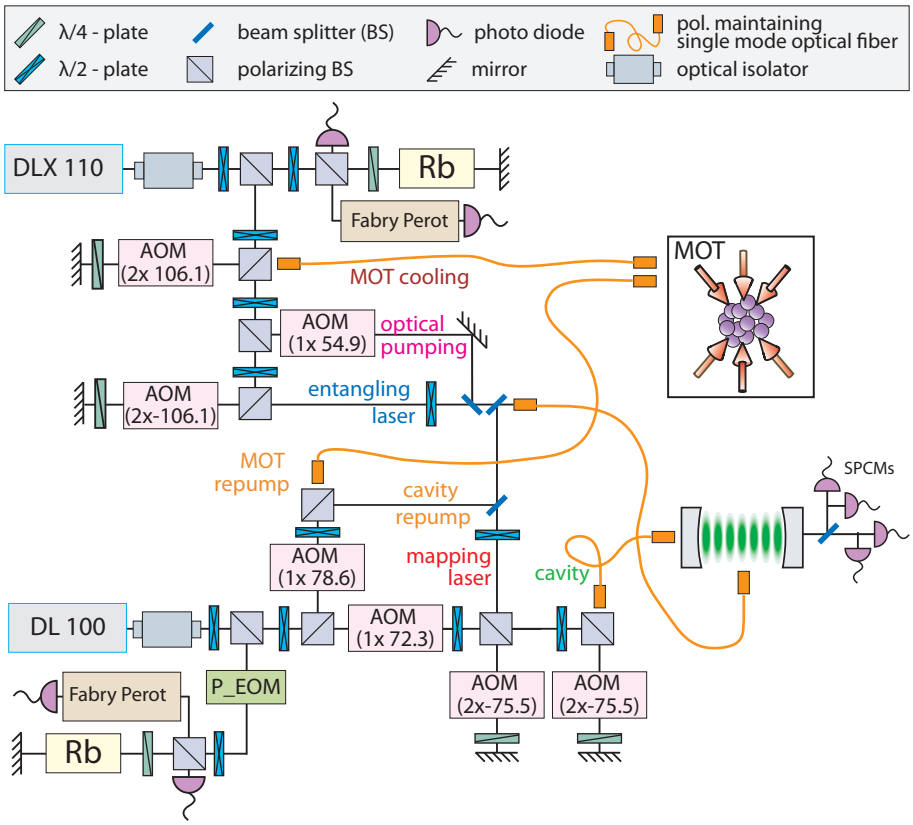

Figure 4.5: **Overview of the laser system.** The two diode lasers provide all beams necessary for the scheme. All beams that are applied on the atoms while in the cavity are superimposed on beam splitters and sent to the experiment through only one fiber. More details are given in the text.

(see subsection 3.2.4). Also, the H/V basis is the canonically used when discussing states of photons. The two wave plates not only change the basis from circular to linear, they also compensate for birefringence in the windows of our vacuum chamber and for polarization rotations from mirrors in the optical path.

Single mode fiber and fiber polarization control

To guide the photons towards the detection setup, a single-mode optical fiber is used. A polarization maintaining (PM) single mode optical fiber is not suitable since it typically has different refraction indices along its fast and slow axis (138). This means that a photon with polarization components along both axes (as we expect to generate) is not maintained because of a relative phase shift along the two axes. Additionally, due to the different refraction indices along the two axes the polarization of the output of a PM fiber is very sensitive to temperature fluctuations. Such fluctuations

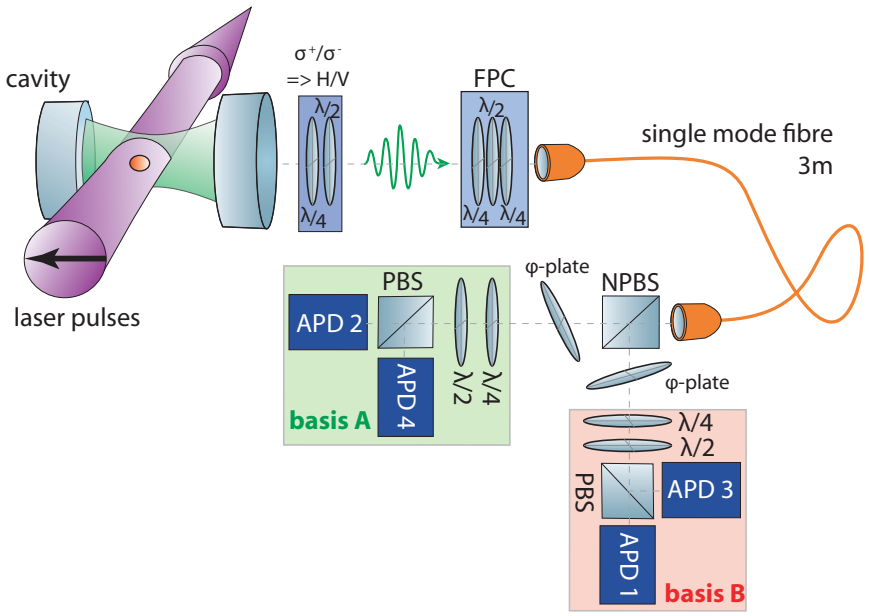

Figure 4.6: **Detection setup.** Behind the cavity the polarization of the emitted σ^+/σ^- photons is rotated to linear horizontal/vertical (H/V). The photons are then directed through a single-mode optical fiber (with fiber polarization controller FPC) towards the detection area. There they are randomly distributed with a non-polarizing beam splitter (NPBS) towards two detection setups (basis A/B) for measurements in different polarization bases. Phase plates (φ-plate) correct for possible phase shifts in the NPBS. Single photons are detected with avalanche photodiodes (APDs).

will lead to different variations in the optical path length along these two axes resulting in phase fluctuations between the two polarization components and makes polarization controllability very difficult. In contrast, a non-polarization maintaining single mode fiber is made from isotropic material and therefore temperature fluctuations should influence both axes the same.

Stress induced by bending the fiber change the outcoming polarization. To keep this constant, the fiber is fixed on the table. The residual stress induced polarization rotation is therefore constant and can be corrected with a set of wave plates forming the fiber polarization control (FPC). A combination of $\lambda/4$, $\lambda/2$ and $\lambda/4$ plates in the appropriate settings correct for any polarization change. This is tested by the correct transmission of H/V-polarized light and of light polarized in a direction that has both H and V polarization components. Only then can one be sure that the phase shift induced by the fiber is also compensated and all polarizations are preserved.

Non-polarizing beam splitter

The non-polarizing beam-splitter (NPBS) is the heart of the detection setup. As in the setup with the polarized single photons described before in subsection 3.2.4, it allows us to do a Hanbury Brown & Twiss measurement, or to superimpose photons coming from different fibers, maybe even from different atom-cavity systems. Here, it is used to direct the photons emerging from the cavity randomly towards two polarization analyzing setups. This enables the measurement of subsequent photons in different bases making a full quantum state tomography possible.
In contrast to downconversion experiments, the photons are separated in time, so that they can be distinguished by their arrival times even if they are emitted in the same spatial mode and are detected by one and the same detector. This enables us to measure in four different bases at once with only one combination of wave plate settings in basis A and B: Both photons could be directed towards basis A, both to basis B, the first photon to A and the second to B, or the first photon to B and the second to A. Hence, with appropriate settings of the wave-plates, only three different settings are sufficient to get all the necessary information for reconstructing the density matrix. These three settings are: First, one of the setups measures in horizontal/vertical (H/V) basis, the other one in the diagonal/antidiagonal (D/A) basis; second, one setup in H/V-basis, the other one in right-/left-circular (R/L) basis; third, one setup in D/A, the other in R/L.
Even though three measurement settings are sufficient, it is sometimes useful to do the measurement with more than just these settings. For example, in a measurement with 16 different wave plate settings one mimics the case where only one detector is present in each output port of the NPBS. This measurement can be used to gain information about the relative quantum efficiencies of the detectors (125). In the following measurements with fewer settings, this information can be used to correct for eventual unbalanced quantum efficiencies of the detectors. On the other hand, adjusting the wave plates by hand is also a source of imprecisions and systematic errors. Therefore it is advantageous to rotate them only when necessary.
Since the NPBS induces a phase shift between the horizontal and vertical polarization components, it has to be corrected with a birefringent material like a birefringent crystal acting as a phase plate (φ-plate). Here, a multiorder wave-plate was used for this purpose. To do so, first the axes of the crystal are aligned with respect to the horizontal and vertical, so that the polarization of the H and V do not change. Then it is tilted such that also the D/A component is conserved. This has to be done for the reflected and transmitted part of the light separately, since the phase shift will be different for each.

$\lambda/4$	$\lambda/2$	transmitted	reflected
0°	0°	H	V
0°	22.5°	R	L
45°	22.5°	D	A

Table 4.1: Transmitted and reflected polarization components for different setting of the wave plates in each of the polarization analyzing setups.

Polarization analyzing setup

As discussed in subsection 4.1.3, the setup for polarization measurements consists of a $\lambda/4$ and a $\lambda/2$ wave plate to adjust the measurement basis, a polarizing beam splitter (PBS) and one detector in each output port of the PBS. For defined positions of the wave plates, certain measurement bases are chosen. For both wave plates at 0° (the fast axis vertical), the wave plates do not rotate the measurement basis and H-polarized light is transmitted through the PBS, whereas V-polarized light is reflected. Table 4.1 shows the appropriate wave plate settings for measurements in the D/A or L/R-basis. To detect the photons, avalanche photodiodes (APDs) of the type *SPCM-AQR-16* are used as in the experiment with the polarized photons. The four APDs build in the setup have an average quantum efficiencies of about 45%.

Detection efficiency

The coupling into and the transmission through the optical fiber is 72%. The NPBS and each of the PBSs have about 2% losses, whereas losses from all other optical elements are negligible. With the quantum efficiency of the avalanche photodiodes of 45% this leads to an overall detection efficiency for photons emitted from the cavity of 31%. Compared to single photon sources with atoms in free space (70; 71; 72; 73), where the detection efficiency is about 10^{-3} this is an improvement of two orders of magnitude.

Data acquisition

Since in this experiment four detectors are used, all inputs of the *FAST ComTec P7888* data acquisition card are used for data inputs and no channel is free to record the timing information as it has been done for the polarized photons (subsection 3.2.4). Therefore the timing information is added electronically onto one of the input channels. The trigger for the timing is shaped such that it can be well discriminated from the signal resulting from the photons detected with the APDs. The APDs that were used have typically a dead-time of $\sim 60\,\mathrm{ns}$ after a photo-detection. This means that two photons cannot be detected with the same detector if their separation in

time is smaller and hence an APD never sends a second signal pulse sooner than this dead-time. To set the timing information, in each sequence of optical pumping, entangling and mapping pulses, a signal consisting of two 20 ns long TTL pulses with a separation of only 20 ns is added onto one channel. This signal is filtered from the photons by the evaluation software, which otherwise deduces all correlations between first and second photon in all detectors.

4.3 Sequence

During the pump-pulse sequence, the atoms are first prepared in the desired initial state, and then the entanglement and the mapping laser pulses are applied. The pump-pulse sequence is drawn in Fig. 4.7. In the following subsections (4.3.1 and 4.3.2) details about the pump pulses are given. In the detection time distribution measurement discussed in subsection 4.3.3, it is shown that the experiment is running as expected. Then a correlation measurement (subsection 4.3.4) demonstrates that only single photons are emitted during entangling and mapping pulses. The efficiency of the scheme is determined from the conditioned efficiencies described in subsection 4.3.5. Note that for the experimental results shown in this section, the magnetic field inside the cavity needs to be compensated, as will be described in subsection 4.4.1.

4.3.1 Preparing the atoms

Preparation of the initial state $|F = 2, m_F = 0\rangle \equiv |2, 0\rangle$ is achieved by optical pumping with a π-polarized laser resonant with the transition from $F = 2$ to the excited $F' = 2$ level, see Fig. 4.7. Since the transition from state $|2, 0\rangle$ to state $|F' = 2, m_{F'} = 0\rangle$ is forbidden, $|2, 0\rangle$ is a dark state. To avoid pumping into the F=1 ground level, an additional laser couples the $F = 1$ and $F' = 2$ levels. When writing this thesis we noticed that in this configuration one might have the problem of coherent population trapping (139; 140; 141), but both lasers are applied simultaneously for 2.8 μs and have constant Rabi frequencies of about $\Omega/2\pi = 22$ MHz ($F = 2$ to $F' = 2$) and $\Omega/2\pi = 28$ MHz ($F = 1$ to $F' = 2$), respectively.
Note that failure of the optical pumping does not reduce the measured entanglement fidelity. This is because our protocol described in subsection 4.1.1 guarantees that an atom in a wrong initial state can only emit a photon in either the first or the second pulse, but never in both. For example, if the atom is accidently pumped into state $|F = 2, m_F = \pm 1\rangle$, the atom-cavity system can emit a first photon. Thereby the atom is transferred into state $|F = 1, m_F = 0\rangle$, which is a dark state for a transition from $F = 1$ to $F' = 1$ and no second photon can be produced. After false preparation in the states $|F = 2, m_F = \pm 2\rangle$ or in $F = 1$, not even a first photon can be emitted from

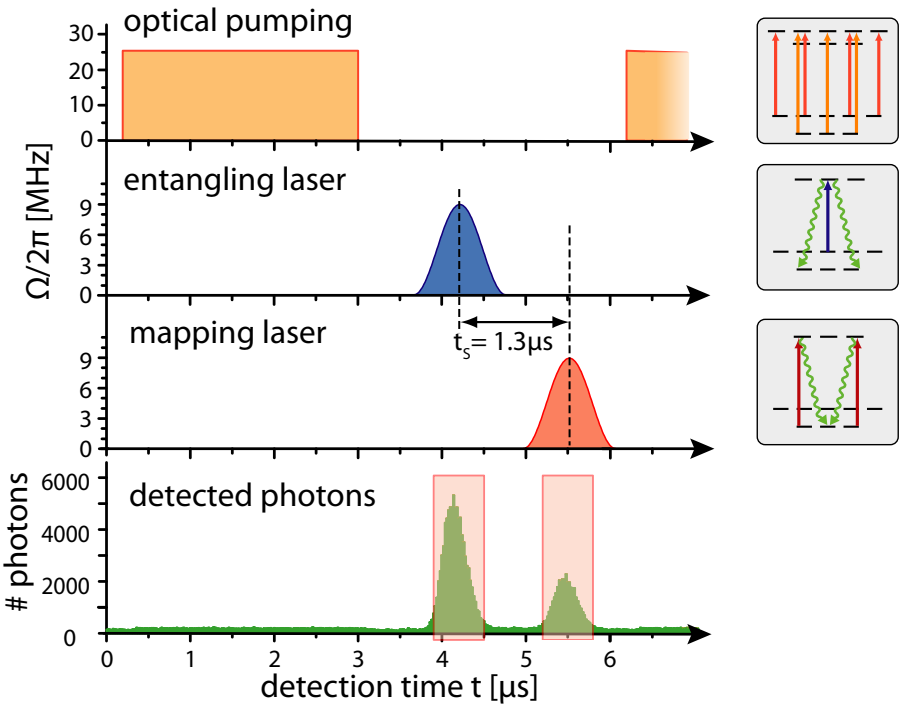

Figure 4.7: **Experimental sequence.** Laser-pulse sequence and the arrival-time distribution of the photons. The atom is prepared by optical pumping. Then a laser pulse entangles the atom and the first photon. After a time delay t_s, a second laser pulse maps the atomic state onto a second photon. As shown in the arrival time distribution, the duration of the photon wave packets produced by the adiabatic passage technique is about 300 ns (FWHM). The time windows considered in the evaluation procedure are also shown.

the system.

Of course, a good probability of preparation in the favored state is essential for driving the scheme efficiently, because only then a pair of entangled photons is emitted. To experimentally determine how long the optical pumping takes, a measurement was done where the optical pumping duration was varied. In Fig. 4.8 the number of photon pairs per number of MOTs (triangles) and per number of first photons (circles) is plotted against the duration of the optical pump pulse. Both numbers are important. The number of photon pairs per MOT monitors the overall rate of photons which reflects the measuring time needed, whereas the number of pairs per 1st photon is a measure how efficiently the scheme works and how well the atom is prepared in state $|2,0\rangle$. Both signals increase for longer pump pulse duration, but saturate after about 2.8 μs (dashed vertical line) which therefore is a good compromise for the duration of the optical pumping to get as many pairs as possible in a preferably short sequence.

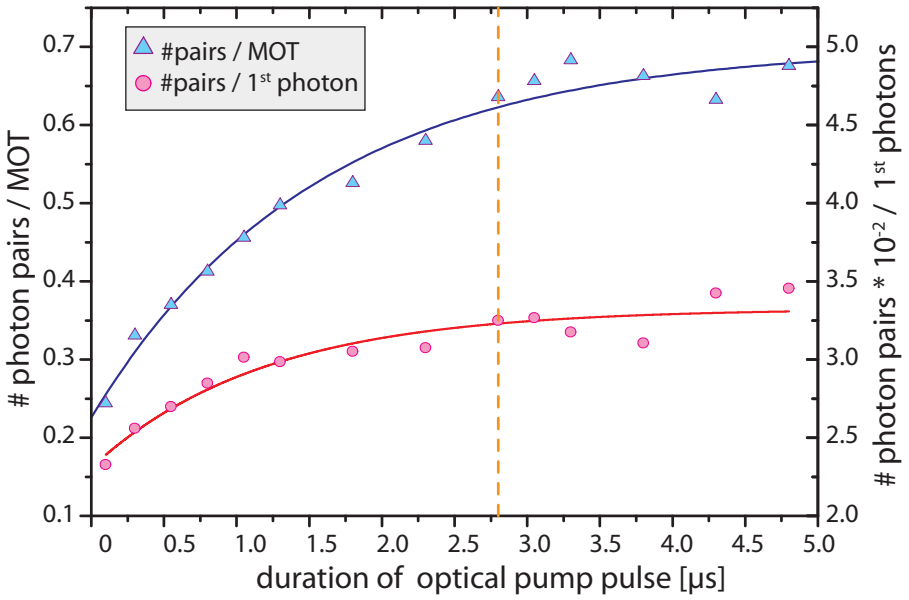

Figure 4.8: **Number of photon pairs versus optical pump duration.** To determine the ideal optical pump pulse duration, the number of photon pairs per number of MOTs and per number of first photons is investigated. After a duration of more than 2.8 μs the number of pairs saturate, which is therefore a good compromise for the duration of the optical pumping to get as many pairs as possible.

4.3.2 Entangling and mapping pulses

The laser pulses used for entangling and mapping have a $\sin^2(\omega t/t_p)$ time dependence with duration $t_p = 1.1\,\mu$s and their peak Rabi frequency is about $\Omega/2\pi = 9\,$MHz. Note that to ensure equal Rabi frequencies, the illuminated power of entangling and mapping pulses have to be very different because the relative strength of the transitions are unequal. The entangling laser is acting on a transition with a strength of only 4/60 whereas the mapping laser is acting on a transition with a strength of 25/60, see Appendix A.
The values for these peak Rabi frequencies were set experimentally from measurements of the contrast C_{HV}, Eq. (4.5), which for an ideal Ψ^- state would have a value of +1. In Fig. 4.9 the contrast C_{HV} is shown as a function of the peak Rabi frequency of the entangling (dark dots) and of the mapping pulse (light triangles). For increasing Rabi frequencies the contrast reduces for both. The main reason for this decrease is the increasing probability to emit two photons during the same pump pulse. For the mapping pulse this can be explained by the fact that once the atom is in the state $|F = 1, m_F = 0\rangle$ (either after the successful entangling and mapping or after a *wrong* entangling photon) it can undergo a transition via $F' = 0$. Indeed, $F' = 0$ is far (72 MHz) from the $F' = 1$ state, but the mapping laser and cavity are on Raman resonance. For high Rabi frequencies this possi-

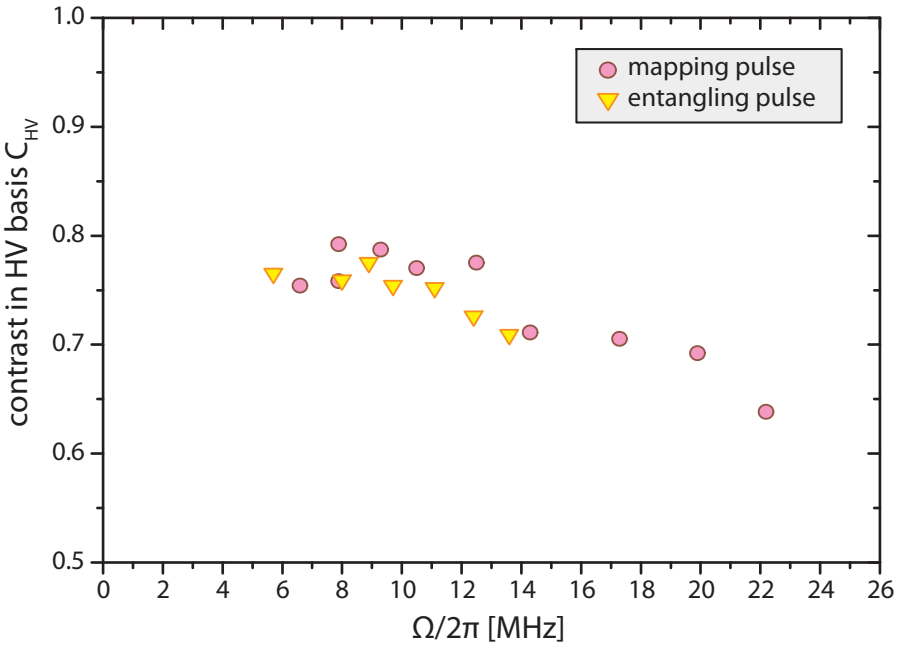

Figure 4.9: **Contrast in HV-basis versus pump pulse Rabi frequency.** As shown, the contrast C_{HV} reduces for increasing peak Rabi frequencies for both entangling and mapping pulses.

ble transition becomes problematic and the probability of getting a second photon per mapping pulse increases.
Another explanation could be that the polarization of the pump pulses is not pure, so that by increasing the pump laser Rabi frequency, $\sigma^{\pm}$ transitions could also be driven. This would lead to *false* photon events in both entangling and mapping pulses reducing the contrast C_{HV}.

4.3.3 Arrival time distribution

To show that the sequence is running properly, the arrival time distribution is deduced from the measured photon stream. As can be seen in Fig. 4.7, almost no photons are detected during the optical pumping since both lasers drive transitions to $F' = 2$ and the cavity is on the $F = 1$ to $F' = 1$ transition. The constant signal observed during that time can be attributed to dark counts and a few background photons. Only during the entangling and mapping pulses are photons detected. Both photons approximately follow the envelope of the pump pulses and have a duration of 300 ns (FWHM). Even though the entangling and mapping pulses have the same Rabi frequency, more photons are detected during the entangling pulse. The reason for this is that the atoms are initially prepared in the $F = 2$ ground state during optical pumping, and a photon generation during the mapping pulse

is only possible when the atom is in the $F = 1$ ground state. With a good state preparation, an emission during the mapping pulse can only happen after a successful first emission during the entangling pulse. Only if the state preparation fails and the atom ends up in one of the $|F = 1, m_F = \pm 1\rangle$ states, an emission during the mapping pulse could happen without previous emission during the entangling pulse.
The entangling and mapping pulses are temporally well separated from each other by an adjustable time interval t_s so that the detected photons can clearly be assigned to the first or the second laser pulse. Figure 4.7 also displays the time windows considered for the evaluation of the polarization state of the photons.

4.3.4 Source of single photons

One essential requirement to make the scheme work is that the atom-cavity system acts like a real single-photon source during the entanglement and mapping pulses. Therefore, a Hanbury Brown & Twiss measurement proves that only single photons emerge from the cavity (see subsection 3.3.3). This is done by calculating the correlations between photon detections in basis A and in basis B without taking notice of their polarization. The signals of the two APDs in basis A (and in basis B) are simply added. The resulting correlation function is shown in Fig. 4.10. Compared with Fig. 3.12, it again shows a Gaussian envelope that reflects the atom cavity interaction time and a comb-like structure. Here, each comb-line consists of a group of three peaks which results from correlations between two pairs of photons[(i.)]. The most important information obtained from this measurement is that the peak in the center is largely suppressed, showing that only single photons are emitted. The remaining peak at $\tau = 0$ has about the same height as the peaks at large detection time differences ($\tau > 40\,\mu$s), therefore it can mostly be attributed to other atoms passing through the cavity at the same time (122). To assure that the peak in the center is small, first, the atom flux through the cavity has to be set low enough that the probability to have two atoms in the cavity at the same time is very low; second the probability for an atom to emit two photons during the same pump pulse needs to be negligible.

The atom flux through the cavity

Similar to subsection 2.3.2, the atom flux can be adjusted by the loading time of the MOT and by the detuning of the MOT cooling laser during

[(i.)] Since the sequence is repeated every $6\,\mu$s, correlations between photons from subsequent entangling laser pulses as well as from subsequent mapping laser pulses appear at this detection time delay. At $\tau = 6\,\mu\text{s} \mp t_s$ correlations between photons emitted during the mapping laser (entangling laser) and during the subsequent entangling laser (mapping laser) are expected, respectively.

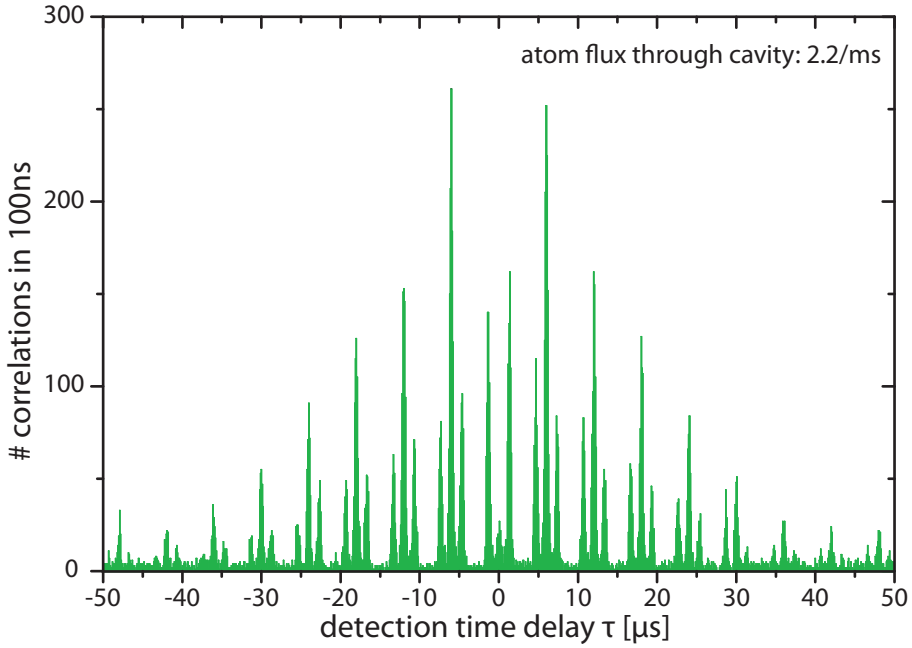

Figure 4.10: **The autocorrelation of the photon stream** is evaluated in a configuration that mimics a Hanbury Brown & Twiss setup. The most important feature here is that the probability of getting two clicks at the same time ($\tau = 0$) is very small. Hence, single-photons are emitted from the system.

the optical molasses after switching off the magnetic quadrupole field. The MOT loading time affects the number of atoms in the atomic cloud, whereas the detuning of the cooling laser determines the temperature of the atomic cloud and therefore its expansion when the cloud falls through the cavity mode. From the correlation measurement shown in Fig. 4.10, the atomic flux can be estimated using the total number of correlations. Multiple atom contributions and the number of background detections can also be estimated; for details see (122). Here, the atomic flux of about 2.2 atoms/ms is so low, that the probability to find more than one atom during the transit time of 35 μs inside the cavity is only 0.4%. Most of the time (92.6%) the cavity is empty and in 7.0% exactly one atom is present.

Probability to detect two photons per pulse

From the autocorrelation measurement of the photon stream in Fig. 4.10 one can deduce the probability to get two photons per pump pulse. This probability depends on the Rabi frequencies of the entangling and mapping laser. With increasing pump laser power, especially for the mapping laser, the probability to find a second photon in the same pump pulse increases. This can be explained by the fact that during the entangling pulse, the atom

undergoes a transition from one hyperfine ground state to the other, whereas the mapping laser induces transitions between Zeeman sublevels of one and the same hyperfine level. In the first case the system is out of resonance when the photon has left the cavity. This is not the case when pump laser and cavity have the same frequency as in the second case, where mapping laser and cavity are both resonant to the transition from $F = 1$ to $F' = 1$. Then cavity and mapping laser are always in Raman resonance, which could lead to a transition via the $F' = 0$ level which is about 72 MHz apart. Or a small polarization deviation of the linear polarization of the pump laser can induce transitions between state $|0\rangle$ and $|F' = 1, m_F = \pm 1\rangle$. By choosing a deliberately low mapping pulse Rabi frequency, both problems can be largely suppressed.
As a result, for the conditions chosen in the later measurements, where the peak Rabi frequencies of entangling and mapping laser are about $\Omega/2\pi = 9$ MHz (subsection 4.3.2), we observe a second photon in the same pulse after detecting a first photon with a probability of only 0.6%.

4.3.5 Efficiency of the process

The efficiency of entangling and mapping process has to be calculated conditioned on a first photon detection, since we never know if there is an atom inside the cavity, see subsection 3.3.4: After a first photo-detection occurs during the entangling pulse, we know from the ratio between signal clicks to background clicks that an atom is present in the cavity with a probability of 93%. After this trigger event, the number of photons is counted for the subsequent entangling or mapping pulse. The population in the $F = 2$ hyperfine ground state is ideally restored during the state preparation, whereas a photon during the mapping laser pulse only occurs after previous emission of a photon in the entangling laser pulse. Therefore, we only condition on a detection during the entangling laser pulse. The efficiency of an emission during the entangling laser pulse conditioned on a photon detection during the previous entangling pulse is 14.8%. The efficiency of emitting a photon during the mapping pulse conditioned on a detection during the preceding entangling pulse is found to be 8.8%.
As a result, the overall probability for an emission of a photon pair is 1.3% when an atom is present inside the cavity. This efficiency includes random positions of the atom in the cavity mode and hence random atom-cavity coupling constants. Therefore, this number is a lower limit for the expectation of the efficiency one could get with a deterministically coupled atom.

4.4 Results

In the previous section it was shown, that the atom-cavity system emits pairs of single photons in the entangling and mapping pulses. Here, the

entanglement between the photon pair is observed by a polarization analysis of the two photons, also proving the successful state mapping from the atom onto the photon and the prior atom-photon entanglement. But first, the magnetic field has to be compensated. In subsection 4.4.1, it is described how the magnetic field perpendicular to the cavity axis is compensated. The magnetic field along the cavity axis is then used to change the phase of the atomic superposition state. In subsection 4.4.2 a full quantum state tomography is presented. Finally, the coherence properties of the generated superposition state of the atom are discussed in 4.4.3.

4.4.1 Compensating the magnetic field

As discussed in subsection 4.1.2, a magnetic field along the cavity can be used to rotate the atomic state in a controlled way between the two photon detections, whereas a magnetic field perpendicular to the cavity axis leads to a mixture of the atomic Zeeman substates which may result in *wrong* second photon emission. Therefore the magnetic field perpendicular to the cavity must be compensated.

Magnetic fields perpendicular to cavity axis

To compensate the magnetic field perpendicular to the cavity axis the contrast C_{HV} given in Eq. (4.5) is measured as a function of the magnetic field. Remember that behind the cavity, the $\sigma^{\pm}$ polarized photons are rotated into H/V polarization. Therefore, measuring in the H/V basis is not phase sensitive, and we observe the number of correlations between the photon polarizations in this unrotated basis. The magnetic field is varied with the current in the large coils in Helmholtz configuration surrounding the whole experimental setup, which were build to compensate the earth magnetic field (142). In Fig. 4.12, the contrast C_{HV} is plotted against the current in the compensation coils for the vertical (z) and the horizontal (x) B-field components. The magnetic field in the center of the coils is calculated from the current to be 370 mG/A. As described in subsection 4.1.2, the contrast reduces when a magnetic field is present, so that the point of zero magnetic field can be attributed to the maximal contrast. The uncertainty of the position of maximal contrast is about 0.01 A in the current running through the coils, which leads to an accuracy of the magnetic field compensation of about 4 mG. In the following experiments the currents in the coils were set such that the magnetic field perpendicular to the cavity axis is compensated.

Magnetic field along the cavity axis

Analogous to the discussion in subsection 4.1.2 with a magnetic field along the cavity axis, a frequency insensitive detection after the fiber of the first photon with, e.g. right circular polarization $|R\rangle \equiv \frac{1}{\sqrt{2}}(|H\rangle - i\,|V\rangle)$, projects

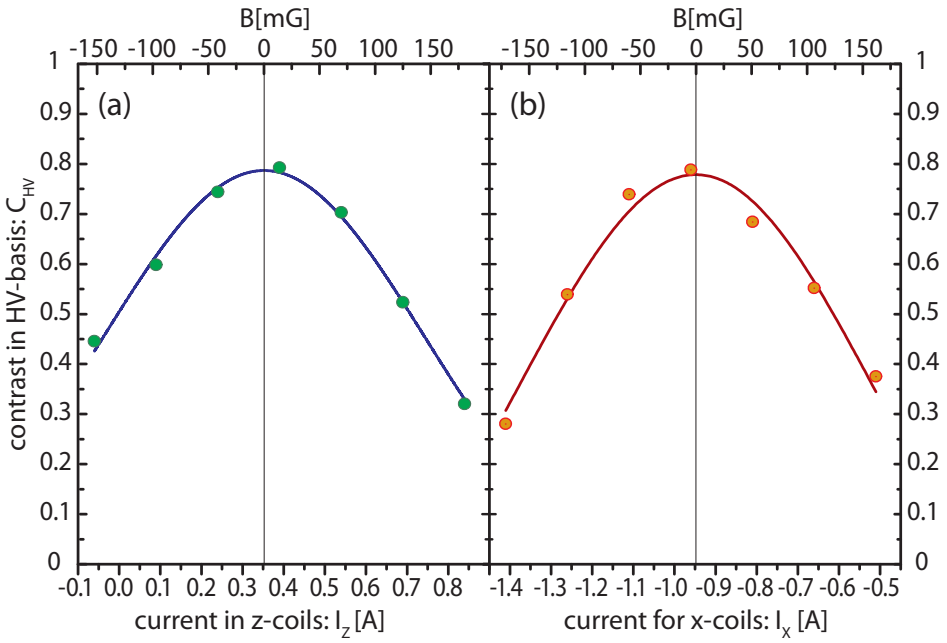

Figure 4.11: **Compensating the magnetic field perpendicular to the cavity axis,** (a) along the z-axis and (b) along the x-axis. The contrast in the HV-basis C_{HV} is plotted against the current in the compensation coils. The corresponding magnetic field amplitude is calculated, whereas the zero field is attributed to the maximal contrast derived from a Gauss fit. Time distance between the entangling and mapping pulse is $t_s = 1.3\,\mu$s.

the atomic state into a superposition of $|+1\rangle$ and $|-1\rangle$ with equal amplitudes. The Zeeman splitting of the atomic levels then leads to a relative phase shift of these states, see Eq. (4.3). Subsequent state mapping transfers this onto the photonic state (Eq. (4.4)) which continues rotating until the second photon is detected. The total rotation angle depends on the time difference between the two photon detections τ which in the experiment can only be adjusted to some extent because of the finite duration of the photons δt. Partially, τ can be controlled by the separation between entangling and mapping pulses t_s (Fig. 4.3). Alternatively, for a given time separation, t_s, the time evolution of the superposition state can be adjusted by the magnetic field strength as it is shown in Fig. 4.12. There, the contrast C_{RL} is shown as a function of the current in the Helmholtz coils in the direction of the cavity. This measurement was done for different two time separations between entangling and mapping pulse: $t_s = 1.3\,\mu$s and $t_s = 2.8\,\mu$s. One expects a $\cos(2\Delta t_s)$ dependence. The oscillatory behavior is a manifestation of the phase rotating at twice the Larmor frequency. For increasing field magnitude, the envelope of the oscillation decreases. This is due to the envelope of the long photon wave packets produced in our

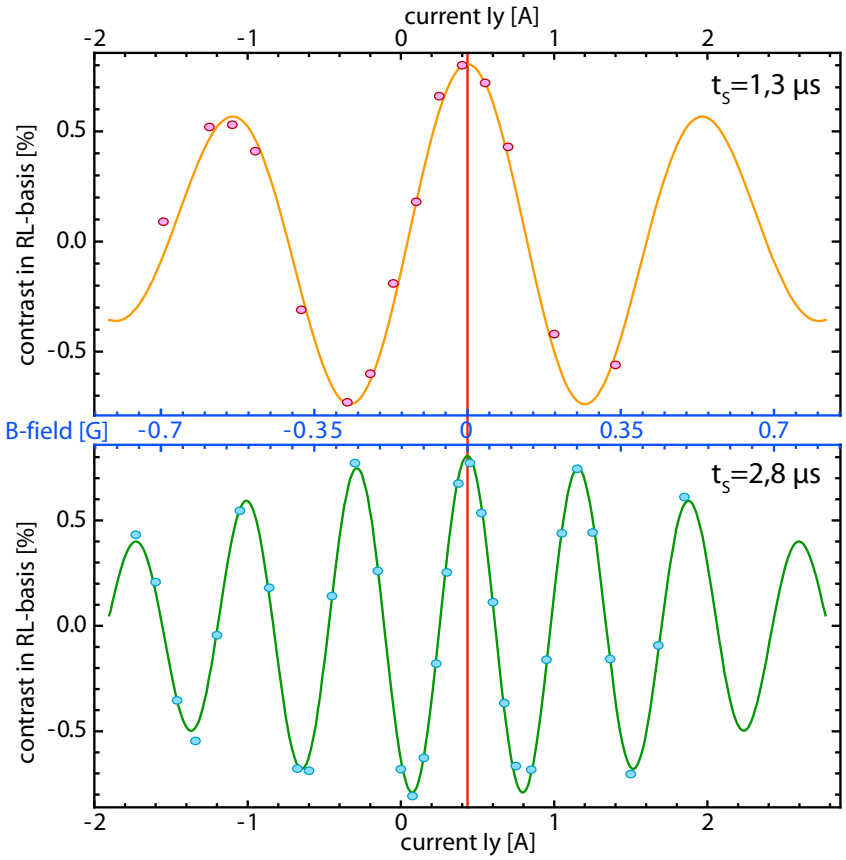

Figure 4.12: **Atomic state rotation.** After detecting a first photon in the R/L basis the atom is projected into a superposition state that is time dependent when a magnetic field along the cavity is applied. Displayed is the contrast C_{RL} as a function of the applied current in the compensation coils in y-direction. In (a) the time distance between entangling and mapping pulse was $t_s = 1.3\,\mu$s in (b) $t_s = 2.8\,\mu$s. A model described in the text fits the data nicely.

scheme, see Fig. 4.7. As a result, there is a range of possible time intervals between two photon detections and thus phases of the superposition: The average over this range of phases reduces the contrast for larger magnetic fields. Therefore, the maximum of the envelope is at zero magnetic field. This is supported by the fact that both curves for $t_s = 1.3\,\mu$s and $t_s = 2.8\,\mu$s have their center at the same current of the coils. They both show a coinciding maximal contrast, which is the point where the phase evolution starts. Together both measurements are nicely fit by the theory described in subsection 4.1.2. Here, only cuts through the planes of interest at $t_s = 1.3\,\mu$s and $t_s = 2.8\,\mu$s are shown, not the whole 3D-plot shown in Fig. 4.3. The single-photon wave-packets were assumed to have a Gaussian envelope with duration 300 ns (FWHM), and the only free parameters are the conversion of

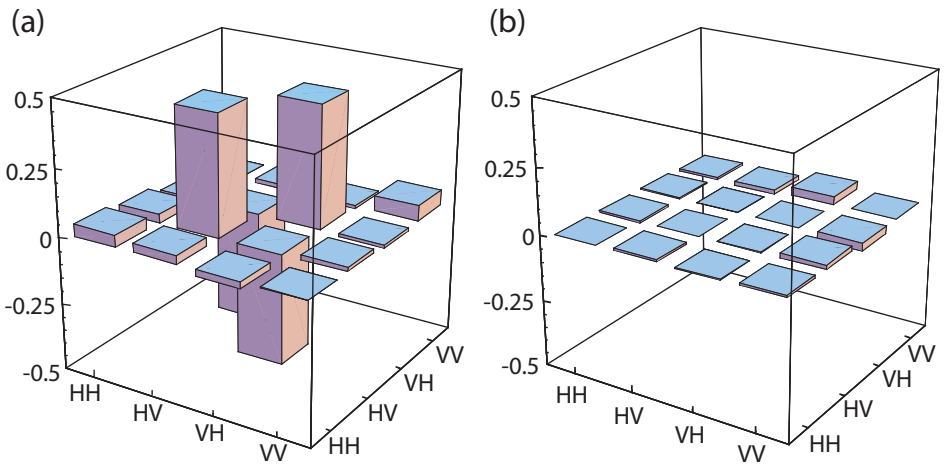

Figure 4.13: **Density matrix of the measured two-photon polarization state.** (a) shows the real and (b) the imaginary part of the density matrix deduced by state tomography of the two photons emitted one after the other from the atom-cavity system.

current into magnetic field strength, which is 360 mG/A in good agreement with (142) and the offset current for the zero magnetic field point.
In principle one could post-select two photon events with a well defined detection time delay τ from the data. Then no decrease in the contrast should be visible for increasing magnetic field strength B. However, this would require a lot more data than the measurement shown here.

4.4.2 State tomography

Once the parameters such as pump laser Rabi frequencies and magnetic field have been optimized using techniques sensitive to the entanglement, the density matrix of the two photons is obtained via state tomography.

Zero magnetic field

The density matrix of the entangled state given in Eq. (4.2) is obtained from a full quantum state tomography for zero magnetic field. In this case no time evolution occurs between the two photon detections. Figure 4.13 shows the measured density matrix reconstructed from the two-photon Stokes parameters, determined by measuring two-photon events in the four detectors. The measurement was done with nine different settings of wave plates and about 2200 events were accumulated per setting. The resulting density matrix (see appendix B.1) has only positive eigenvalues and therefore represents a physically possible state. Its fidelity with respect to the expected Bell state, $|\Psi^-\rangle$ of Eq. (4.2), is $F = 86.0(4)\%$. From the density matrix we also derive

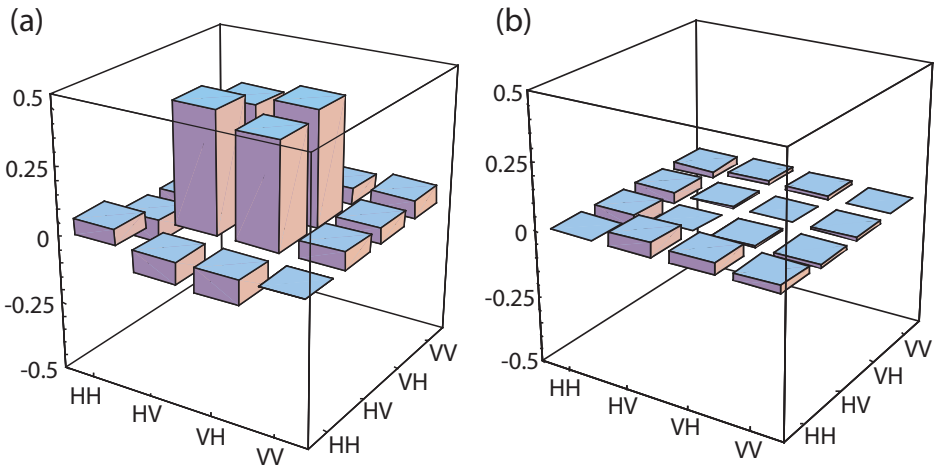

Figure 4.14: **Density matrix of the measured two-photon polarization state with magnetic field $B = -0.13\,\mathrm{G}$.** The outcome of a state tomography measurement of the two photons emitted one after the other from the atom-cavity system.

a concurrence Eq. (4.14) of $C = 0.73(7)$ and an entanglement of formation Eq. (4.15) of $E = 0.63(9)$. Due to technical imperfections, (polarizers in the detection setups, etc.) the observed entanglement measures set a lower bound for the entanglement achieved at the cavity output.

Non-zero magnetic field along the cavity axis

Similar measurements were done with a magnetic field along the cavity axis of $B = -0.13\,\mathrm{G}$ and a separation between entangling and mapping pulses of $t_s = 2.8\,\mu\mathrm{s}$. For these parameters, as one can read off Fig. 4.12, the atomic superposition state accumulates a relative phase shift of the components of π. Therefore, a density matrix corresponding to the Bell state $|\Psi^+\rangle$, see Eq. (4.11), is expected. This is indeed observed in a measurement with six different wave plate settings and about 1800 events/setting. The experimental data shown in Figure 4.14 exhibit a fidelity of 82.9(6)% with respect to $|\Psi^+\rangle$, a concurrence of $C = 0.72(13)$ and an entanglement of formation of $E = 0.62(16)$. (See also appendix B.2.) Note that the state evolves between the two photon detections due to the constant magnetic field and therefore the $|\Psi^+\rangle$ state actually never existed. As discussed in subsection 4.1.2, if the two photons are detected at the same time, e.g. by implementing a delay line, one would always observe a $|\Psi^-\rangle$ state.

Discussion

Both state tomographies show that our system is clearly entangled. The degree of the entanglement is similar to the results obtained by other groups

(70; 72; 125) that observed entanglement between an atom and a photon. Different to other experiment, where the state of the atom is directly measured with a shelving technique, here we study two processes, first the entanglement itself and then the mapping, which are probed at once with this measurement. Unfortunately, we could not at the time make an estimation of the fidelity of the single processes. However, the fidelity of the combined process can be higher or lower than each of the single processes. Only if one can prove, that there is no possibility to get the entangled state via a different quantum mechanical path, is the achieved fidelity the product of the fidelities of the single processes.
Still, the non-perfect fidelity makes us think about possible errors. Here, the main problem is the possibility of having a second atom inside the cavity which may emit a second photon. Calculating the conditioned efficiencies we found, that about 5% of the second photons come from a different atom than the first photons, which will give a random result for the second photon (white noise, limits maximal fidelity to 96.3%). Additionally, correlations with dark counts play a role. Both effects can not fully explain the deviation from a maximally entangled state. Nonetheless, in an experiment with a single atom fixed in a cavity these problems will be solved, since one can be sure that only one atom is present and the measurement duration only depends on how long the atom stays inside the cavity. The signal to noise ratio will therefore increase.
Even though only in 7% of the measuring times an atom is present in the cavity, the overall detection rate of entangled photon-pairs is about 2 events/second. This event rate is on the same order of magnitude as the reported atom-photon entanglement observation rate (70; 72; 125), where the atom was permanently trapped and only one photon needed to be detected. This demonstrates that a cavity has a great impact on the efficient implementation of quantum networks.

4.4.3 Coherence time of the atomic superposition

In this chapter, entanglement between two subsequently emitted photons was demonstrated as well as the quantum state transfer from a single atom onto a single photon and therefore also atom-photon entanglement. For the use of the atom-cavity system as quantum memory it would be interesting to know how long the information can be stored in the atomic qubit state. To test the phase decoherence of the atomic superposition we have done a measurement of the contrast C_{HV} and C_{RL} simultaneously for different waiting times between the entangling and mapping laser pulses t_s. The result of the measurement is shown in Fig. 4.15. The first photon is detected immediately after its emission from the cavity and projects the atom into a certain state. When detecting the first photon in the HV-basis, the atom will be projected either in state $|-1\rangle$ or $|+1\rangle$, when detecting the photon

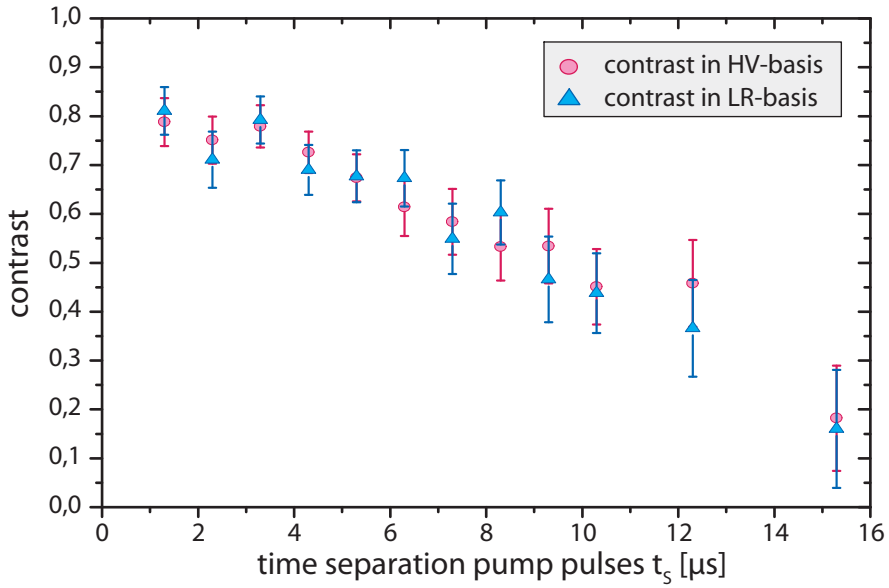

Figure 4.15: **Contrast as a function of pump pulse time separation.** When measuring C_{RL}, the first photon detection will project the atom into a superposition of $|F = 1, M_F \pm 1\rangle$. The contrast is then a measure of the phase coherence of this superposition. For the C_{HV}, the first detection projects the atom into one of the $|F = 1, M_F \pm 1\rangle$ states. This state naturally experiences no dephasing, therefore the fact that both contrasts decrease in the same manner is an indication that the phase decoherence is not the limiting factor.

in the RL-basis, the atom will be projected into a superposition of these states. For such an atom, phase decoherence can occur, whereas for an atom in one of the hyperfine ground states phase, decoherence plays no role in the result. In C_{RL}, the phase coherence of the two states is tested and every phase shift will lead to a reduction in contrast. Typically this should occur with a different time constant than for the contrast in HV-basis. There, e.g. a magnetic field could mix the different Zeeman levels leading to a reduced contrast. The observation that for both C_{HV} and C_{RL} the contrast reduces at the same time scale is an indication that other processes are responsible for this reduction. Comparing the reduction of the contrast with the reduction of number of photon pairs per MOT (Fig. 4.16), we see that this may be the primary source of loss of contrast. Obviously, for large pump pulse separations, the two detected photons will not origin from the same atom, their polarization state will be in a completly mixed state and the contrast is zero for both C_{HV} and C_{RL}.
Therefore, it seems that the limiting factor in this measurements was more the reduced number of photon pairs than the decoherence itself. Doing such a measurement for a setup with a fixed atom, where the atom could

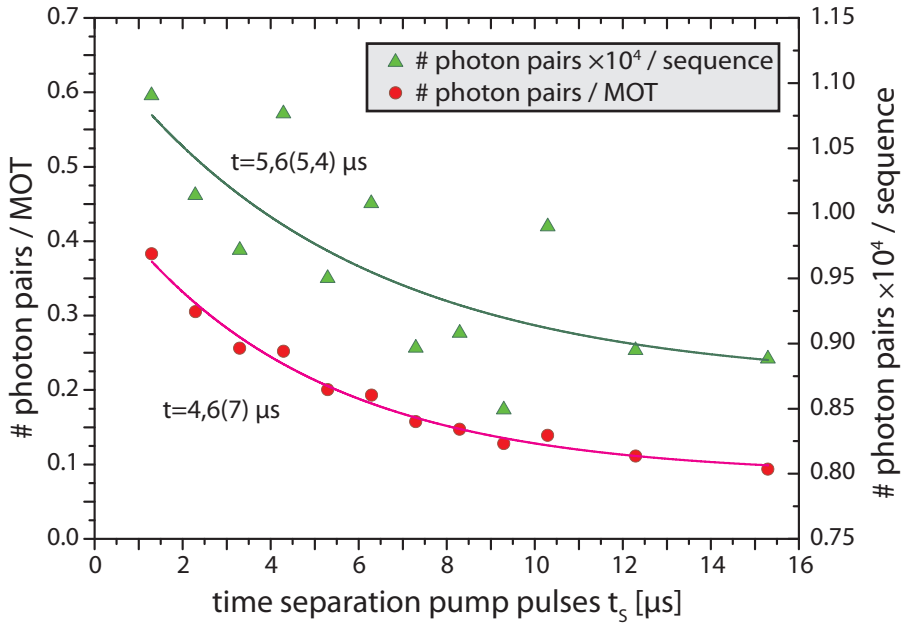

Figure 4.16: **The number of photon pairs per MOT and the number of pairs per sequence** decrease faster than the contrast in Fig. 4.15. This decrease signalizes that the atom is not well coupled to the cavity any more after $t_s \geq 5\,\mu$s and the probability of generating the second photon is getting smaller.

be observed for many seconds (143), would eliminate this effect and allow probing of the decoherence over much longer timescales.

4.5 Conclusion

In this chapter we have described the realization of atom-photon entanglement and the subsequent state mapping of the atomic state onto a second photon which results in an entangled photon pair. In a state tomography of the two-photon state it was shown that indeed entanglement was present in the system. From the measured density matrix we obtained a concurrence $C = 0.73(7)$ and an entanglement of formation $E = 0.63(9)$. The overlap with the desired Bell state $|\Psi^-\rangle$ was reached with a fidelity $F = 86.0(4)\%$. Using a constant magnetic field we have also demonstrated a state rotation of the atomic state, depending on the magnetic field strength and the time between the photon detections. With this method the atomic state was manipulated such that a density matrix was obtained resembling a $|\Psi^+\rangle$ Bell state with fidelity $F = 82.9(6)\%$. Again, the entanglement was clearly observed with a concurrence $C = 0.72(13)$ and an entanglement of formation $E = 0.62(16)$. For an atom in a superposition state no phase decoherence

was found during the atom-cavity interaction time in comparison to an atom in one of the hyperfine states. In our experiment, even though the atom has a limited interaction time with the cavity, the rate of entangled photon pairs (2 events/seconds) is on the order of the rate of detected entanglement events in other experiments which work in free space with trapped atoms. This shows the importance of a cavity for the efficient implementation of quantum networks.

Chapter 5

Outlook

This thesis establishes an atom-cavity system with the ability to generate single photons as a versatile toolbox for quantum information processing in a distributed network (80), since it provides an interface between stationary (atoms) and flying (photons) qubits. Single atoms are ideal quantum memories because they have long coherence times (91; 90), whereas single photons are well suited to transmit quantum information between distant nodes of a quantum network.
With our system we have produced a stream of polarization-controlled single photons (chapter 3). These photons show their mutual coherence in a time-resolved two photon interference experiment, proving that the generation process is well under control. Moreover, entanglement between an atom and an emitted photon has been created where the atomic state was further mapped onto a second photon resulting in a pair of entangled photons (chapter 4). The schemes presented here are intrinsically deterministic since atom-cavity systems are in principle able to generate single photons with unity efficiency (75). Furthermore, the photons are emitted into a well-defined spatio-temporal mode which can easily be manipulated, e.g. guided in fibers, overlapped on beam splitters and focused onto a detector.
Our scheme of two entangled photons can in the future be extended to generate three or more entangled photons. For example, partial driving of the Raman transition in combination with atomic state manipulation should allow one to produce time-bin entangled multi-photon states (144; 145). Polarization-entangled multi-photon states are also feasible with two possible schemes depicted in Fig. 5.1. The key for the implementation of these schemes is, after entangling the atomic substates with the polarization of the emitted photon, to manipulate the atomic superposition state symmetrically on isolated paths such that each component can only emit photons of a defined polarization. Accordingly, the degeneracy of the Zeeman states has to be lifted at least partially to separately address only certain transitions between specific sublevels. One of the schemes presented here relies

on the Stark effect (146), the other on the Zeeman effect (147).
In Fig. 5.1 (a), a π-polarized laser field with a frequency close to the $F = 2$ to $F' = 2$ transition of the D_1-line of ^{87}Rb (at 795 nm) shifts the Zeeman levels differently dependent on the coupling strength to the excited level. To first approximation, the shift of the $|F = 2, m_F = 0\rangle$ state will be zero since this state does not couple to the $|F' = 2, m_F = 0\rangle$ state. Initially the atom is prepared in state $|F = 1, m_F = 0\rangle$ and the cavity is fixed on the transition from $F = 2$ to $F' = 2$. **Step 1:** Atom-photon entanglement is created by driving a transition to states $|-1\rangle$ and $|+1\rangle$ while a $\sigma^{\pm}$ photon is emitted, respectively. **Step 2:** The pump laser frequency is chosen to be in Raman resonance with the cavity only for the transition from $|F = 2, m_F = \pm 1\rangle$ to $|F = 2, m_F = \pm 2\rangle$, resulting in an emission of a $\sigma^{\mp}$ photon, respectively. The transition to $|F = 2, m_F = 0\rangle$ is far from resonance. **Step 3:** Finally, a laser pulse polarized perpendicular to the cavity axis is applied. Its frequency is chosen such that together with the cavity, the Raman resonance condition is fulfilled for the transition from $|F = 2, m_F = \pm 2\rangle$ to $|F = 2, m_F = 0\rangle$, thereby emitting a $\sigma^{\pm}$ photon, respectively. This scheme results in the atom disentangled from the light and the generation of a three-photon entangled state.
In Fig. 5.1 (b) the degeneracy of the Zeeman substates is lifted by applying a magnetic field along the cavity axis. Initially the atom is prepared in the $|F = 2, m_F = 0\rangle$ state and the cavity is tuned to the $F = 1$ to $F' = 2$ transition. **Step 1:** Laser and cavity drive a transition to the $|F = 1, m_F = \pm 1\rangle$ levels while a $\sigma^{\mp}$ photon is emitted, respectively. **Step 2:** Microwave transitions map the population in the $|F = 1, m_F = \pm 1\rangle$ levels onto the $|F = 2, m_F = \pm 2\rangle$ levels, respectively. From there, laser and cavity drive a transition back to the $|F = 1, m_F = \pm 1\rangle$ levels while emitting $\sigma^{\pm}$ photons. Step 2 can be repeated as often as wanted to generate a chain of entangled photons. **Step 3:** Starting from the $|F = 1, m_F = \pm 1\rangle$ levels, the atom is finally disentangled from the light by applying a laser that together with the cavity drives a transition to the $|F = 1, m_F = 0\rangle$ state while a $\sigma^{\pm}$ photon is emitted, respectively.
Both schemes have their advantages and drawbacks. On the one hand scheme (a) can be performed very rapidly, since it is only based on optical transitions, whereas (b) also involves microwave transitions which are typically slower. On the other hand, in scheme (a) the atom can lose its coherence when absorbing a photon from the Stark-shift laser, whereas the coherence of the Zeeman states can be controlled by stabilizing the magnetic field. While scheme (b) can emit more than three entangled photons, an extension of the scheme would allow the same for scheme (a). Both schemes can in principle be implemented with the setup used in this thesis analogous to the atom-photon interface demonstrated. However, because the current setup has a limited interaction time between atom and cavity, our group has set up two new atom-cavity systems, akin to each other, where

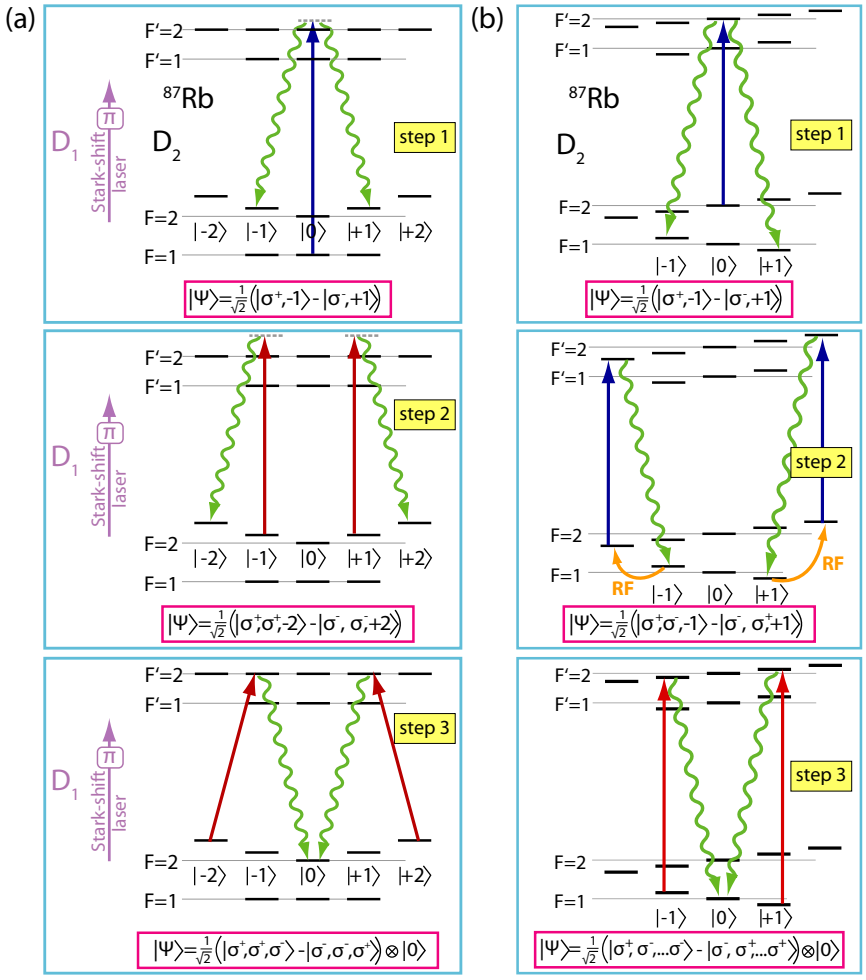

Figure 5.1: **Generation of multi-photon entangled states.** (a) This scheme relies on the AC-Stark shift which is induced by a laser field which is close to the resonance from $F = 2$ to $F' = 2$ of the D_1-line. Therefore, one can address certain transitions between Zeeman substates without driving unwanted or even multiple transitions with the same pump laser pulse. (b) This scheme relies on the Zeeman effect that lifts the degeneracy between the substates. This allows to individually address microwave transitions between the $|F = 1, m_F = \pm 1\rangle$ and $|F = 2, m_F = \pm 2\rangle$ states, respectively. More details on both schemes are given in the text.

the atom is fixed inside the cavity within a standing wave dipole trap (143). By applying cavity-cooling forces (148; 149) the atom can be stored in the cavity for several seconds (150; 151; 152). The technique of cavity cooling was successfully combined with the generation of single-photons, and one of the systems demonstrated its operation as a single photon server with ^{85}Rb (78; 153).

The next step will be to demonstrate atom-photon entanglement with each of these systems and combine the two. By measuring two photons (each coming from one of the systems) in a Bell state, the remaining atoms are entangled, as was recently demonstrated with ions in free-space using photons carrying frequency qubits (92) and photons carrying polarization qubits (154). This technique allows to entangle atom-cavity systems at very large distances and opens the possibility to perform a loophole-free Bell measurement (155) as a test for quantum theory.

Two (or more) such systems operated in parallel are well suited for teleportation and entanglement experiments in a quantum network (100; 99; 98; 156) as well as for quantum gate operations in a distributed quantum computer (157; 158; 159). Altogether, an atom-photon interface opens many possibilities in multiple directions of quantum information processing.

Appendix A

Rubidium energy levels

A.1 Level scheme of the D_2-line

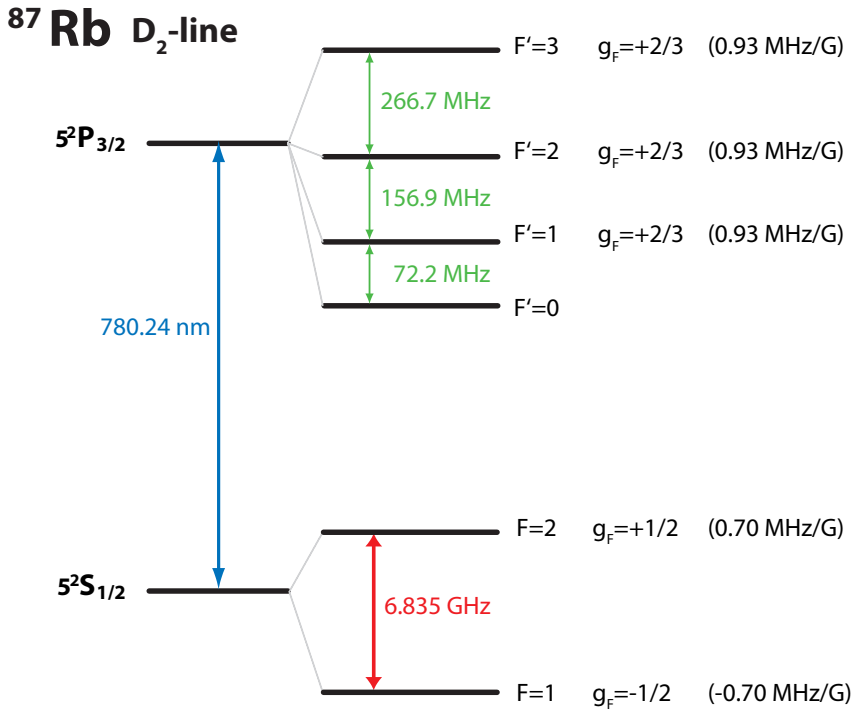

Figure A.1: **D_2-line of Rubidium 87.** All values are taken from (121)

.

A.2 Coupling strengths of the D_2-line

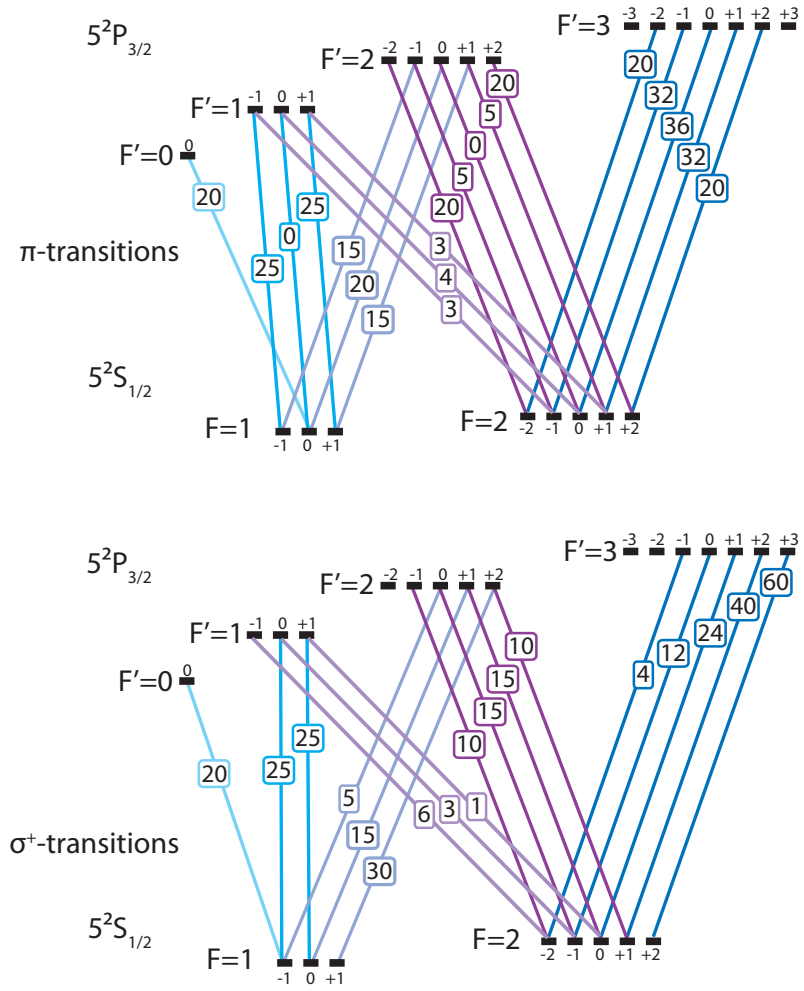

Figure A.2: **Coupling strength of the D_2-line of Rubidium 87.** In the upper part the relative coupling strength for π-transitions are given, below the relative coupling strength for all σ^+-transitions. The coupling strengths are taken from (120) for atoms with nuclear spin I=3/2 like Rubidium 87.

Appendix B

Density matricies

B.1 Reconstructed $|\Psi^-\rangle$ density matrix

$$\begin{pmatrix} 0.045 & 0.031 - 0.007i & -0.026 + 0.003i & -0.001 - 0.008i \\ 0.031 + 0.007i & 0.449 & -0.410 + 0.001i & 0.015 - 0.0156i \\ -0.026 - 0.003i & -0.410 - 0.001i & 0.452 & -0.011 + 0.031i \\ -0.001 + 0.008i & 0.015 + 0.016i & -0.011 - 0.031i & 0.055 \end{pmatrix}$$

The data that served for reconstructing the density matrix was taken at zero magnetic field. In each of nine different wave plate settings about 2200 entanglement events were recorded.

B.2 Reconstructed $|\Psi^+\rangle$ density matrix

$$\begin{pmatrix} 0.061 & -0.077 - 0.050i & -0.087 - 0.042i & -0.002 - 0.026i \\ -0.077 + 0.050i & 0.449 & 0.393 - 0.004i & 0.062 + 0.014i \\ -0.087 + 0.042i & 0.393 + 0.004i & 0.424 & 0.056 + 0.009i \\ -0.002 + 0.026i & 0.062 - 0.014i & 0.056 - 0.009i & 0.067 \end{pmatrix}$$

The data that served for reconstructing the density matrix was taken with a magnetic field along the cavity axis with $B = -0.13\,\mathrm{G}$. In each of six different wave plate settings about 1800 entanglement events were recorded.

Bibliography

[1] C. Cohen-Tannoudji, B. Diu, and F. Laloë. *Quantenmechanik* (Walter de Gruyter &Co., Berlin, 1997).

[2] A. Einstein, B. Podolsky, and N. Rosen. *Can Quantum-Mechanical Description of Physical Reality Be Considered Complete?* Phys. Rev. **47**, 777 (1935).

[3] D. Bohm. *Quantum Theory* (Dover Publ., New York, repr. 1989).

[4] M. A. Nielsen and I. L. Chuang. *Quantum Computation and Quantum Information* (Cambridge University Press, 2000).

[5] T. Beth and G. Leuchs, (editors) *Quantum Information Processing* (Wiley-VCH, Berlin, 2003).

[6] P. Zoller, T. Beth, D. Binosi, R. Blatt, H. Briegel, D. Bruss, T. Calarco, J. I. Cirac, D. Deutsch, J. Eisert, A. Ekert, C. Fabre, N. Gisin, P. Grangier, M. Grassl, S. Haroche, A. Imamoglu, A. Karlson, J. Kempe, L. Kouwenhoven, S. Kröll, G. Leuchs, M. Lewenstein, D. Loss, N. Lütkenhaus, S. Massar, J. E. Mooij, M. B. Plenio, E. Polzik, S. Popescu, G. Rempe, A. Sergienko, D. Suter, J. Twamley, G. Wendin, R. Werner, A. Winter, J. Wrachtrup, and A. Zeilinger. *Quantum information processing and communication.* The European Physical Journal D - Atomic, Molecular and Optical and Plasma Physics **36**, 203 (2005).

[7] C. H. Bennett and P. W. Shor. *Quantum information theory.* IEEE Transactions on Information Theory **44**, 2724 (1998).

[8] N. Gisin, G. Ribordy, W. Tittel, and H. Zbinden. *Quantum Cryptography.* Rev. Mod. Phys. **74**, 145 (2002).

[9] A. Steane. *Quantum Computing.* Rep. Prog. Phys. **61**, 117 (1998).

[10] S. L. Braunstein, H.-K. Lo, and P. Kok, (editors) *Scalable Quantum Computers: Paving the Way to Realisation* (Wiley-VCH Weinheim, 2001).

[11] B. Schumacher. *Quantum coding.* Phys. Rev. A **51**, 2738 (1995).

[12] P. Benioff. *The computer as a physical system: A microscopic quantum mechanical Hamiltonian model of computers as represented by Turing machines.* Journal of Statistical Physics **V22**, 563 (1980).

[13] R. Feynman. *Simulating physics with computers.* Int. J. Theor. Phys. **21**, 467 (1982).

[14] D. Deutsch. *Quantum Theory, the Church-Turing Principle and the Universal Quantum Computer.* Proc R. Soc. Lond. **400**, 97 (1985).

[15] D. Deutsch. *Quantum Computational Networks.* Proc R. Soc. Lond. **425**, 73 (1989).

[16] D. P. DiVincenzo. *Two-bit gates are universal for quantum computation.* Phys. Rev. A **51**, 1015 (1995).

[17] D. Gottesman and I. L. Chuang. *Demonstarting the Viability of Universal Quantum Computation Using Teleportation and Single-Qubit Operators.* Nature **402**, 390 (1999).

[18] D. Deutsch and R. Jozsa. *Rapid Solution of Problems by Quantum Computation.* Proc R. Soc. Lond. **439**, 553 (1992).

[19] L. K. Grover. *A fast quantum mechanical algorithm for database search.* Proc. 28 Annual ACM Symposium on the Theory of Computing 212 – 219 (1996).

[20] L. K. Grover. *Quantum Computers Can Search Arbitrarily Large Databases by a Single Query.* Phys. Rev. Lett. **79**, 4709 (1997).

[21] P. W. Shor. *Polynomal-time algorithms for prime factorization and discrete logarithms on a quantum computer.* SIAM Review **41**, 303 (1997).

[22] D. P. DiVincenzo. *The Physical Implementation of Quantum Computation.* Fortschr. Phys. **48**, 771 (2000).

[23] N. A. Gershenfeld and I. L. Chuang. *Bulk Spin-Resonance Quantum Computation.* Science **275**, 350 (1997).

[24] L. M. Vandersypen, M. Steffen, G. Breyta, C. S. Yannoni, R. Cleve, and I. L. Chuang. *Experimental Realization of an Order-Finding Algorithm with an NMR Quantum Computer.* Phys. Rev. Lett. **85**, 5452 (2000).

[25] L. M. Vandersypen, M. Steffen, G. Breyta, C. S. Yannoni, M. H. Sherwood, and I. L. Chuang. *Experimental realization of Shor's quantum factoring algorithm using nuclear magnetic resonance.* Nature **414**, 883 (2001).

[26] D. Loss and D. P. DiVincenzo. *Quantum computation with quantum dots.* Phys. Rev. A **57**, 120 (1998).

[27] A. Imamoglu, D. D. Awschalom, G. Burkard, D. P. DiVincenzo, D. Loss, M. Sherwin, and A. Small. *Quantum Information Processing Using Quantum Dot Spins and Cavity QED.* Phys. Rev. Lett. **83**, 4204 (1999).

[28] A. Badolato, K. Hennessy, M. Atature, J. Dreiser, E. Hu, P. M. Petroff, and A. Imamoglu. *Deterministic Coupling of Single Quantum Dots to Single Nanocavity Modes.* Science **308**, 1158 (2005).

[29] I. Chiorescu, Y. Nakamura, C. J. P. M. Harmans, and J. E. Mooij. *Coherent Quantum Dynamics of a Superconducting Flux Qubit.* Science **299**, 1869 (2003).

[30] T. Yamamoto, Y. Pashkin, O. Astafiev, Y. Nakamura, and J. S. Tsai. *Demonstration of conditional gate operation using superconducting charge qubits.* Nature **425**, 941 (2003).

[31] A. Wallraff, D. I. Schuster, A. Blais, L. Frunzio, R. S. Huang, J. Majer, S. Kumar, S. M. Girvin, and R. J. Schoelkopf. *Strong coupling of a single photon to a superconducting qubit using circuit quantum electrodynamics.* Nature **431**, 162 (2004).

[32] M. Steffen, M. Ansmann, R. C. Bialczak, N. Katz, E. Lucero, R. McDermott, M. Neeley, E. M. Weig, A. N. Cleland, and J. M. Martinis. *Measurement of the Entanglement of Two Superconducting Qubits via State Tomography.* Science **313**, 1423 (2006).

[33] E. Knill, R. Laflamme, and G. J. Milburn. *A scheme for efficient quantum computing with linear optics.* Nature **409**, 46 (2001).

[34] T. C. Ralph, A. G. Witte, W. J. Munro, and G. J. Milburn. *Simple scheme for efficient linear optics quantum gates.* Phys. Rev. A **65**, 012314 (2001).

[35] C. K. Hong, Z. Y. Ou, and L. Mandel. *Measurement of Subpicosecond Time Intervals between Two Photons by Interference.* Phys. Rev. Lett. **59**, 2044 (1987).

[36] T. Legero, T. Wilk, A. Kuhn, and G. Rempe. *Time-Resolved Two-Photon Quantum Interference.* Appl. Phys. B **77**, 797 (2003).

[37] T. B. Pittman, M. J. Fitch, B. C. Jacobs, and J. D. Franson. *Experimental controlled-NOT logic gate for single photons in the coincidence basis.* Phys. Rev. A **68**, 032316 (2003).

[38] J. L. O'Brien, G. J. Pryde, A. G. White, T. C. Ralph, and D. Branning. *Demonstration of an all-optical quantum controlled-NOT gate.* Nature **426**, 264 (2003).

[39] S. Gasparoni, J.-W. Pan, P. Walther, T. Rudolph, and A. Zeilinger. *Realization of a Photonic Controlled-NOT Gate Sufficient for Quantum Computation.* Phys. Rev. Lett. **93**, 020504 (2004).

[40] J. I. Cirac and P. Zoller. *Quantum Computations with Cold Trapped Ions.* Phys. Rev. Lett. **74**, 4091 (1995).

[41] A. S. Sørensen and K. Mølmer. *Quantum Computation with Ions in Thermal Motion.* Phys. Rev. Lett. **82**, 1971 (1999).

[42] C. Monroe, D. M. Meekhof, B. E. King, W. M. Itano, and D. J. Wineland. *Demonstration of a Fundamental Quantum Logic Gate.* Phys. Rev. Lett. **75**, 4714 (1995).

[43] D. Leibfried, B. DeMarco, V. Meyer, D. Lucas, M. Barrett, J. Britton, W. M. Itano, B. Jelenkovic, C. Langer, T. Rosenbrand, and D. J. Wineland. *Experimental demonstration of a robust, high-fidelity geometric two ion-qubit phase gate.* Nature **422**, 412 (2003).

[44] F. Schmidt-Kaler, H. Häffner, M. Riebe, S. Gulde, G. P. T. Lancaster, T. Deuschle, C. Becher, C. F. Roos, J. Eschner, and R. Blatt. *Realization of the Cirac-Zoller controlled-NOT quantum gate.* Nature **422**, 408 (2003).

[45] J. Chiaverini, J. Britton, D. Leibfried, E. Knill, M. D. Barrett, R. B. Blakestad, W. M. Itano, J. D. Jost, C. Langer, R. Ozeri, T. Schaetz, and D. J. Wineland. *Implementation of the Semiclassical Quantum Fourier Transform in a Scalable System.* Science **308**, 997 (2005).

[46] J. Chiaverini, D. Leibfried, T. Schaetz, M. D. Barrett, R. B. Blakestad, J. Britton, W. M. Itano, J. D. Jost, E. Knill, C. Langer, R. Ozeri, and D. J. Wineland. *Realization of quantum error correction.* Nature **432**, 602 (2004).

[47] Q. A. Turchette, C. S. Wood, B. E. King, C. J. Myatt, D. Leibfried, W. M. Itano, C. Monroe, and D. J. Wineland. *Deterministic Entanglement of Two Trapped Ions.* Phys. Rev. Lett. **81**, 3631 (1998).

[48] C. A. Sackett, D. Kielpinski, B. E. King, C. Langer, V. Meyer, C. J. Myatt, M. Rowe, Q. A. Turchette, W. M. Itano, D. J. Wineland, and

C. Monroe. *Experimental Entanglement of Four Particles.* Nature **404**, 256 (2000).

[49] D. Leibfried, E. Knill, S. Seidelin, J. Britton, R. B. Blakestad, J. Chiaverini, D. B. Hume, W. M. Itano, J. D. Jost, C. Langer, R. Ozeri, R. Reichle, and D. J. Wineland. *Creation of a six-atom "Schrödinger cat" state.* Nature **438**, 639 (2005).

[50] H. Häffner, W. Hänsel, C. F. Roos, J. Benhelm, D. Chek-Al-Kar, M. Chwalla, T. Körber, U. D. Rapol, M. Riebe, P. O. Schmidt, C. Becher, O. Gühne, W. Dür, and R. Blatt. *Scalable multiparticle entanglement of trapped ions.* Nature **438**, 643 (2005).

[51] D. Kielpinski, C. R. Monroe, and D. J. Wineland. *Architecture for a Large-Scale Ion-Trap Quantum Computer.* Nature **417**, 709 (2002).

[52] M. A. Rowe, A. Ben-Kish, B. Demarco, D. Leibfried, V. Meyer, J. Beall, J. Britton, J. Hughes, W. M. Itano, B. Jelenkovic, C. Langer, T. Rosenband, and D. J. Wineland. *Transport of Quantum States and Separation of Ions in a Dual RF Ion Trap.* Quant. Inf. Comput. **4**, 257 (2002).

[53] D. Stick, W. K. Hensinger, S. Olmschenk, M. J. Madsen, K. Schwab, and C. Monroe. *Ion trap in a semiconductor chip.* Nature Phys. **2**, 36 (2006).

[54] W. K. Hensinger, S. Olmschenk, D. Stick, D. Hucul, M. Yeo, M. Acton, L. Deslauriers, C. Monroe, and J. Rabchuk. *T-junction ion trap array for two-dimensional ion shuttling, storage, and manipulation.* Appl. Phys. Lett. **88** (2006).

[55] S. Wiesner. *Conjugate coding.* SIGACT News **15**, 78 (1983).

[56] C. H. Bennett and G. Brassard. *Quantum cryptography: Public-key distribution and coin tossing.* Proc. IEEE Int. Conf. Computers, Systems and Signal Processing 175–179 (1984).

[57] A. Ekert. *Quantum Cryptography Based on Bell's Theorem.* Phys. Rev. Lett. **67**, 661 (1991).

[58] D. Stucki, N. Gisin, O. Guinnard, G. Ribordy, and H. Zbinden. *Quantum key distribution over 67 km with a plug&play system.* New J. Phys. **4**, 41 (2002).

[59] C. Gobby, Z. L. Yuan, and A. J. Shields. *Quantum key distribution over 122 km of standard telecom fiber.* Appl. Phys. Lett. **84**, 3762 (2004).

[60] C. Z. Peng, T. Yang, X. H. Bao, J. Zhang, X. M. Jin, F. Y. Feng, B. Yang, J. Yang, J. Yin, Q. Zhang, N. Li, B. L. Tian, and J. W. Pan. *Experimental Free-Space Distribution of Entangled Photon Pairs Over 13 km: Towards Satellite-Based Global Quantum Communication.* Phys. Rev. Lett. **94** (2005).

[61] R. Ursin, F. Tiefenbacher, T. Schmitt-Manderbach, H. Weier, T. Scheidl, M. Lindenthal, B. Blauensteiner, T. Jennewein, J. Perdigues, P. Trojek, B. Omer, M. Furst, M. Meyenburg, J. Rarity, Z. Sodnik, C. Barbieri, H. Weinfurter, and A. Zeilinger. *Entanglement-based quantum communication over 144 km.* Nature Phys. **3**, 481 (2007).

[62] H.-J. Briegel, W. Dür, J. I. Cirac, and P. Zoller. *Quantum Repeaters: The Role of Imperfect Local Operations in Quantum Communication.* Phys. Rev. Lett. **81**, 5932 (1998).

[63] W. K. Wootters and W. H. Zurek. *A single quantum cannot be cloned.* Nature **299**, 802 (1982).

[64] M. Oxborrow and A. G. Sinclair. *Single-Photon Sources.* Cont. Physics **46**, 173 (2005).

[65] C. Kurtsiefer, S. Mayer, P. Zarda, and H. Weinfurter. *Stable Solid-State Source of Single Photons.* Phys. Rev. Lett. **85**, 290 (2000).

[66] R. Brouri, A. Beveratos, J.-P. Poizat, and P. Grangier. *Photon Antibunching in the Fluorescence of Individual Color Centers in Diamond.* Opt. Lett. **25**, 1294 (2000).

[67] P. Michler, A. Kiraz, C. Becher, W. V. Schoenfeld, P. M. Petroff, L. Zhang, E. Hu, and A. Imamoglu. *A Quantum Dot Single Photon Turnstile Device.* Science **290**, 2282 (2000).

[68] C. Santori, M. Pelton, G. Solomon, Y. Dale, and Y. Yamamoto. *Triggered Single Photons from a Quantum Dot.* Phys. Rev. Lett. **86**, 1502 (2001).

[69] A. Kiraz, M. Ehrl, Th, Ö. E. Müstecaplioğlu, C. Bräuchle, and A. Zumbusch. *Indistinguishable Photons from a Single Molecule.* Phys. Rev. Lett. **94** (2005).

[70] B. B. Blinov, D. L. Moehring, L.-M. Duan, and C. Monroe. *Observation of entanglement between a single trapped atom and a single photon.* Nature **428**, 153 (2004).

[71] B. Darquié, M. P. A. Jones, J. Dingjan, J. Beugnon, S. Bergamini, Y. Sortais, G. Messin, A. Browaeys, and P. Grangier. *Controlled*

single-photon emission from a single trapped two-level atom. Science **309**, 454 (2005).

[72] J. Volz, M. Weber, D. Schlenk, W. Rosenfeld, J. Vrana, K. Saucke, C. Kurtsiefer, and H. Weinfurter. *Observation of Entanglement of a Single Photon with a Trapped Atom.* Phys. Rev. Lett. **96**, 030404 (2006).

[73] P. Maunz, D. L. Moehring, S. Olmschenk, K. C. Younge, D. N. Matsukevich, and C. Monroe. *Quantum interference of photon pairs from two remote trapped atomic ions.* Nature Phys. **3**, 538 (2007).

[74] A. Kuhn, M. Hennrich, and G. Rempe. *Deterministic single-photon source for distributed quantum networking.* Phys. Rev. Lett. **89**, 067901 (2002).

[75] J. McKeever, A. Boca, A. D. Boozer, R. Miller, J. R. Buck, A. Kuzmich, and H. J. Kimble. *Deterministic Generation of Single Photons from One Atom Trapped in a Cavity.* Science **303**, 1992 (2004).

[76] M. Keller, B. Lange, K. Hayasaka, W. Lange, and H. Walther. *Continuous generation of single photons with controlled waveform in an ion-trap cavity system.* Nature **431**, 1075 (2004).

[77] T. Legero, T. Wilk, M. Hennrich, G. Rempe, and A. Kuhn. *Quantum Beat of Two Single Photons.* Phys. Rev. Lett. **93**, 070503 (2004).

[78] M. Hijlkema, B. Weber, H. P. Specht, S. C. Webster, A. Kuhn, and G. Rempe. *A single-photon server with just one atom.* Nature Phys. **3**, 253 (2007).

[79] T. Wilk, S. C. Webster, H. P. Specht, G. Rempe, and A. Kuhn. *Polarization-Controlled Single Photons.* Phys. Rev. Lett. **98**, 063601 (2007).

[80] J. I. Cirac, P. Zoller, H. J. Kimble, and H. Mabuchi. *Quantum State Transfer and Entanglement Distribution Among Distant Nodes in a Quantum Network.* Phys. Rev. Lett. **78**, 3221 (1997).

[81] A. D. Boozer, A. Boca, R. Miller, T. E. Northup, and H. J. Kimble. *Reversible State Transfer between Light and a Single Trapped Atom.* Phys. Rev. Lett. **98** (2007).

[82] L.-M. Duan, M. D. Lukin, J. I. Cirac, and P. Zoller. *Long-distance quantum communication with atomic ensembles and linear optics.* Nature **414**, 413 (2001).

[83] K. Hammerer, K. Mølmer, E. S. Polzik, and J. I. Cirac. *Light-matter quantum interface.* Phys. Rev. A **70**, 044304 (2004).

[84] D. N. Matsukevich and A. Kuzmich. *Quantum State Transfer Between Matter and Light.* Science **306**, 663 (2004).

[85] J. F. Sherson, H. Krauter, R. K. Olsson, B. Julsgaard, K. Hammerer, I. Cirac, and E. S. Polzik. *Quantum teleportation between light and matter.* Nature **443**, 557 (2006).

[86] S. Chen, Y. A. Chen, B. Zhao, Z. S. Yuan, J. Schmiedmayer, and J. W. Pan. *Demonstration of a Stable Atom-Photon Entanglement Source for Quantum Repeaters.* Phys. Rev. Lett. **99** (2007).

[87] C.-W. Chou, J. Laurat, H. Deng, K. S. Choi, H. de Riedmatten, D. Felinto, and J. H. Kimble. *Functional Quantum Nodes for Entanglement Distribution over Scalable Quantum Networks.* Science **316**, 1316 (2007).

[88] B. Julsgaard, J. Sherson, I. Cirac, J. Fiurassek, and E. S. Polzik. *Experimental demonstration of quantum memory for light.* Nature **432**, 482 (2004).

[89] H. de Riedmatten, J. Laurat, C. W. Chou, E. W. Schomburg, D. Felinto, and H. J. Kimble. *Direct Measurement of Decoherence for Entanglement between a Photon and Stored Atomic Excitation.* Phys. Rev. Lett. **97**, 113603 (2006).

[90] N. Davidson, H. Jin Lee, C. S. Adams, M. Kasevich, and S. Chu. *Long Atomic Coherence Times in an Optical Dipole Trap.* Phys. Rev. Lett. **74**, 1311 (1995).

[91] C. Langer, R. Ozeri, J. D. Jost, J. Chiaverini, B. DeMarco, A. Ben-Kish, R. B. Blakestad, D. B. Hume, W. M. Itano, D. Leibfried, R. Reichle, T. Rosenband, T. Schaetz, P. O. Schmidt, and D. J. Wineland. *Long-Lived Qubit Memory Using Atomic Ions.* Phys. Rev. Lett. **95**, 060502 (2005).

[92] D. L. Moehring, P. Maunz, S. Olmschenk, K. C. Younge, D. N. Matsukevich, L. M. Duan, and C. Monroe. *Entanglement of single-atom quantum bits at a distance.* Nature **449**, 68 (2007).

[93] P. W. H. Pinkse, T. Fischer, P. Maunz, and G. Rempe. *Trapping an Atom with Single Photons.* Nature **404**, 365 (2000).

[94] C. J. Hood, T. Lynn, A. C. Doherty, A. S. Parkins, and H. J. Kimble. *The Atom-Cavity Microscope: Single Atoms Bound in Orbit by Single Photons.* Science **287**, 1477 (2000).

[95] J. A. Sauer, K. M. Fortier, M. S. Chang, C. D. Hamley, and M. S. Chapman. *Cavity QED with optically transported atoms.* Phys. Rev. A **69**, 051804(R) (2004).

[96] T. Wilk, S. C. Webster, A. Kuhn, and G. Rempe. *Single-Atom Single-Photon Quantum Interface.* Science **317**, 488 (2007).

[97] C. Cabrillo, J. I. Cirac, P. García-Fernández, and P. Zoller. *Creation of entangled states of distant atoms by interference.* Phys. Rev. A **59**, 1025 (1999).

[98] D. E. Browne, M. B. Plenio, and S. F. Huelga. *Robust Creation of Entanglement between Ions in Spatially Separate Cavities.* Phys. Rev. Lett. **91**, 067901 (2003).

[99] L.-M. Duan and H. J. Kimble. *Efficient Engineering of Multiatom Entanglement through Single-Photon Detections.* Phys. Rev. Lett. **90**, 253601 (2003).

[100] S. Bose, P. L. Knight, M. B. Plenio, and V. Vedral. *Proposal for Teleportation of an Atomic State Via Cavity Decay.* Phys. Rev. Lett. **83**, 5158 (1999).

[101] S. Lloyd, M. S. Shahriar, J. H. Shapiro, and P. R. Hemmer. *Long Distance, Unconditional Teleportation of Atomic States via Complete Bell State Measurements.* Phys. Rev. Lett. **87**, 167903 (2001).

[102] C. Santori, D. Fattal, J. Vučković, G. S. Solomon, and Y. Yamamoto. *Indistinguishable photons from a single-photon device.* Nature **419**, 594 (2002).

[103] J. Beugnon, M. P. A. Jones, J. Dingjan, B. Darquié, G. Messin, A. Browaeys, and P. Grangier. *Quantum interference between two single photons emitted by independently trapped atoms.* Nature **440**, 779.

[104] T. Wilk, H. P. Specht, S. C. Webster, G. Rempe, and A. Kuhn. *Scheme for generating a sequence of single photons of alternating polarization.* J. Mod. Opt. **54**, 1569 (2007).

[105] M. Hennrich. *Kontrollierte Erzeugung einzelner Photonen in einem optischen Resonator hoher Finesse.* Ph.D. thesis, Max-Planck-Institut für Quantenoptik und Technische Universität München (2003).

[106] T. Legero. *Zeitaufgelöste Zwei-Photonen-Interferenz.* Ph.D. thesis, Max-Planck-Institut für Quantenoptik und Technische Universität München (2005).

[107] A. Kuhn, M. Hennrich, T. Bondo, and G. Rempe. *Controlled Generation of Single Photons from a Strongly Coupled Atom-Cavity System.* Appl. Phys. B **69**, 373 (1999).

[108] A. Kuhn and G. Rempe. *Optical Cavity QED: Fundamentals and application as a Single-Photon Light Source.* Proceedings of the Varenna School on 'Experimental Quantum Information' (2001).

[109] K. Bergmann, H. Theuer, and B. W. Shore. *Coherent Population Transfer Among Quantum States of Atoms and Molecules.* Rev. Mod. Phys. **70**, 1003 (1998).

[110] M. Hennrich, T. Legero, A. Kuhn, and G. Rempe. *Vacuum-Stimulated Raman Scattering Based on Adiabatic Passage in a High-Finesse Optical Cavity.* Phys. Rev. Lett. **85**, 4872 (2000).

[111] M. Hennrich, A. Kuhn, and G. Rempe. *Transition from antibunching to bunching in cavity QED.* Phys. Rev. Lett. **94**, 053604 (2005).

[112] S. Chu, J. E. Bjorkholm, A. Ashkin, and A. Cable. *Experimental Observation of Optically Trapped Atoms.* Phys. Rev. Lett. **57**, 314 (1986).

[113] E. Raab, M. Prentiss, A. Cable, S. Chu, and D. E. Pritchard. *Trapping of Neutral Sodium Atoms with Radiation Pressure.* Phys. Rev. Lett. **59**, 2631 (1987).

[114] G. C. Bjorklund, M. D. Levenson, W. Lenth, and C. Ortiz. *Frequency modulation (FM) spectroscopy.* Appl. Phys. B **32**, 145 (1983).

[115] R. Drever, J. Hall, F. Kowalski, J. Hough, G. Ford, A. Munley, and H. Ward. *Laser phase and frequency stabilization using an optical resonator.* Appl. Phys. B **31**, 97 (1983).

[116] E. Black. *An introduction to Pound-Drever-Hall laser frequency stabilization.* American Journal of Physics **69**, 79 (2001).

[117] H. Specht. *Erzeugung von Einzelphotonen alternierender Polarisation.* Diplomathesis, Max-Planck-Institut für Quantenoptik und Technische Universität München (2005).

[118] M. Hennrich, A. Kuhn, and G. Rempe. *Counter-Intuitive Vacuum-Stimulated Raman Scattering.* J. Mod. Opt. **50**, 935 (2003).

[119] M. O. Scully and M. Zubairy. *Quantum Optics* (Cambridge University Press, Cambridge, United Kingdom, 1997).

[120] H. J. Metcalf and P. van der Straten. *Laser Cooling and Trapping* (Springer, New York, 1999).

[121] D. A. Steck. *Rubidium 87 D Line Data.* Los Alamos National Laboratory (2001, revised 2003).

[122] M. Hennrich, T. Legero, A. Kuhn, and G. Rempe. *Photon statistics of a non-stationary periodically driven single-photon source.* New J. Phys. **6**, 86 (2004).

[123] L.-M. Duan, A. Kuzmich, and H. J. Kimble. *Cavity QED and quantum-information processing with "hot" trapped atoms.* Phys. Rev. A **67**, 032305 (2003).

[124] T. Legero, T. Wilk, A. Kuhn, and G. Rempe. *Characterization of single photons using two-photon interference.* Adv. At. Mol. Opt. Phys. **53**, 253 (2006).

[125] D. L. Moehring, M. J. Madsen, B. B. Blinov, and C. Monroe. *Experimental Bell Inequality Violation with an Atom and a Photon.* Phys. Rev. Lett. **93**, 090410 (2004).

[126] A. Edmonds. *Drehimpulse in der Quantenmechanik* (Bibliogr.Inst., 1964).

[127] D. F. V. James, P. G. Kwiat, W. J. Munro, and A. G. White. *Measurement of qubits.* Phys. Rev. A **64**, 052312 (2001).

[128] J. B. Altepeter, E. R. Jeffrey, and P. G. Kwiat. *Photonic State Tomography.* Adv. At. Mol. Opt. Phys. **52**, 105 (2005).

[129] A. G. White, D. F. James, P. H. Eberhard, and P. G. Kwiat. *Nonmaximally Entangled States: Production, Characterization, and Utilization.* Phys. Rev. Lett. **83**, 3103 (1999).

[130] M. Eibl, N. Kiesel, M. Bourennane, C. Kurtsiefer, and H. Weinfurter. *Experimental Realization of a Three-Qubit Entangled W State.* Phys. Rev. Lett. **92** (2004).

[131] P. G. Kwiat, K. Mattle, H. Weinfurter, A. Zeilinger, A. V. Sergienko, and Y. Shih. *New High-Intensity Source of Polarization-Entangled Photon Pairs.* Phys. Rev. Lett. **75**, 4337 (1995).

[132] J. S. Bell. *On the Einstein Podolsky Rosen paradox.* Physics **1**, 195 (1964).

[133] S. J. Freedman and J. F. Clauser. *Experimental Test of Local Hidden-Variable Theories.* Phys. Rev. Lett. **28**, 938 (1972).

[134] A. Aspect, P. Grangier, and G. Roger. *Experimental Realization of Einstein-Podolsky-Rosen-Bohm Gedankenexperiment: A New Violation of Bell's Inequalities.* Phys. Rev. Lett. **49**, 91 (1982).

[135] Z. Y. Ou and L. Mandel. *Observation of Spatial Quantum Beating with Seperated Photodetectors.* Phys. Rev. Lett. **61**, 54 (1988).

[136] S. Hill and W. K. Wootters. *Entanglement of a Pair of Quantum Bits.* Phys. Rev. Lett. **78**, 5022 (1997).

[137] W. K. Wootters. *Entanglement of Formation of an Arbitrary State of Two Qubits.* Phys. Rev. Lett. **80**, 2245 (1998).

[138] C. Hentschel, J. Vobis, L. Stokes, P. Hernday, V. McOmber, D. M. Baney, W. V. Sorin, J. Beller, C. M. Miller, and S. W. Hinch. *Fiber Optic - Test and Measurement* (Prentice Hall PTR, 1998).

[139] G. A. M. L. Alzetta, G. and G. Orriols. *An Experimental Method for the Observation of RF Transitions and Laser Beat Resonances in Oriented Na Vapors.* Nuovo Cimento Soc. Ital. Fis. B **36**, 5 (1976).

[140] E. Arimondo and G. Orriols. *Nonabsorbing atomic coherences by coherent two-photon transitions in a threelevel optical pumping.* Nuovo Cimento Lett. **17**, 333 (1976).

[141] E. Arimondo. *Progress in Optics: Coherent population trapping in laser spectroscopy*, vol. 35 (Elsevier, Amsterdam, 1996).

[142] M. Elbs. *Realisierung einer magnetooptischen Falle.* Diplomathesis, Universität Konstanz (1994).

[143] S. Nußmann. *Kühlen und Positionieren eines Atoms in einem optischen Resonator.* Ph.D. thesis, Max-Planck Institut für Quantenoptik und Technische Universität München, (2005).

[144] C. Schön, E. Solano, F. Verstraete, J. I. Cirac, and M. M. Wolf. *Sequential Generation of Entangled Multiqubit States.* Phys. Rev. Lett. **95**, 110503 (2005).

[145] C. Schön, K. Hammerer, M. M. Wolf, J. I. Cirac, and E. Solano. *Sequential generation of matrix-product states in cavity QED.* Phys. Rev. A **75**, 032311 (2007).

[146] S. C. Webster. *Scheme for generating three-photon entangled state.* private communication (2007).

[147] D. L. Moehring. *Generation of multi-photon entangled state.* private communication (2007).

[148] P. Maunz, T. Puppe, I. Schuster, N. Syassen, P. W. H. Pinkse, and G. Rempe. *Cavity cooling of a single atom.* Nature **428**, 50 (2004).

[149] P. Maunz. *Cavity cooling and spectroscopy of a bound atom-cavity system.* Ph.D. thesis, Max-Planck-Institut für Quantenoptik und Technische Universität München (2004).

[150] S. Nußmann, K. Murr, M. Hijlkema, B. Weber, A. Kuhn, and G. Rempe. *Vacuum-stimulated cooling of single atoms in three dimensions.* Nature Phys. **1**, 122 (2005).

[151] S. Nußmann, M. Hijlkema, B. Weber, F. Rohde, G. Rempe, and A. Kuhn. *Sub-Micron Positioning of Single Atoms in Micro Cavities.* Phys. Rev. Lett. **95**, 173602 (2005).

[152] J. Bochmann and M. Mücke. *Status of Photon Pistol II.* private communication (2007).

[153] M. Hijlkema. *Single photons from a single atom trapped in a high-finesse optical cavity.* Ph.D. thesis, Max-Planck Institut für Quantenoptik und Technische Universität München, (2007).

[154] D. N. Matsukevich, P. Maunz, S. Olmschenk, D. L. Moehring, and C. Monroe. *Remote Ion-Ion Entanglement with Polarized Photons.* private communication (2007).

[155] C. Simon and W. T. Irvine. *Robust Long-Distance Entanglement and a Loophole-Free Bell Test with Ions and Photons.* Phys. Rev. Lett. **91**, 110405 (2003).

[156] X.-L. Feng, Z.-M. Zhang, X.-D. Li, S.-Q. Gong, and Z.-Z. Xu. *Entangling Distant Atoms by Interference of Polarized Photons.* Phys. Rev. Lett. **90**, 217902 (2003).

[157] X. Zou and W. Mathis. *Conditional quantum phase gate using distant atoms and linear optics.* Phys. Rev. A **71**, 042334 (2005).

[158] Y. L. Lim, A. Beige, and L. C. Kwek. *Repeat-Until-Success Linear Optics Distributed Quantum Computing.* Phys. Rev. Lett. **95**, 030505 (2005).

[159] A. Serafini, S. Mancini, and S. Bose. *Distributed Quantum Computation via Optical Fibers.* Phys. Rev. Lett. **96**, 010503 (2006).

Publications

Single-Atom Single-Photon Quantum Interface
T. Wilk, S. C. Webster, A. Kuhn, and G. Rempe.
Science **317**, 488-490 (2007).

Polarization-Controlled Single Photons
T. Wilk, S. C. Webster, H. P. Specht, G. Rempe, and A. Kuhn.
Physical Review Letters **98**, 063601 (2007).

Scheme for generating a sequence of single photons of alternating polarisation
T. Wilk, H. P. Specht, S. C. Webster, G. Rempe, and A. Kuhn.
Journal of Modern Optics **54**, 1569 (2007).

Characterization of single photons using two-photon interference
T. Legero, T. Wilk, A. Kuhn, and G. Rempe.
Advances in Atomic, Molecular and Optical Physics **53**, 253-289 (2006).

Quantum Beat of Two Single Photons
T. Legero, T. Wilk, M. Hennrich, G. Rempe, and Axel Kuhn.
Physical Review Letters **93**, 070503 (2004).

Time-Resolved Two-Photon Quantum Interference
T. Legero, T. Wilk, A. Kuhn, and G. Rempe
Applied Physics B **77(8)**, 797-802 (2003).

Plasmon Resonances in Large Noble-Metal Clusters
C. Sönnichsen, T. Franzl, T. Wilk, G. von Plessen, and J. Feldmann
New Journal of Physics **4**, 93.1-93.8 (2002).

Drastic Reduction of Plasmon Damping in Gold Nanorods
C. Sönnichsen, T. Franzl, T. Wilk, G. von Plessen, J. Feldmann, O. Wilson, and P. Mulvaney
Physical Review Letters **88**, 077402 (2002).

Danke!

Ein derart anspruchsvolles Forschungsprojekt zu verwirklichen ist natürlich nur in Teamarbeit möglich! Meinen herzlichen Dank möchte ich deswegen all jenen aussprechen, die mich während der Durchführung dieser Arbeit unterstützt und begleitet haben. Insbesondere danke ich:

Gerhard Rempe, der mich in seine Gruppe am MPQ aufgenommen hat, und mir so ermöglichte, die hier beschriebenen Experimente an der Photonenpistole durchzuführen. Mit den richtigen Fragen destillierte er die physikalische Essenz aus den Messungen.

Axel Kuhn hat mit seinen Ideen die ausschlaggebenden Impulse für die Experimente in dieser Arbeit gegeben. Auch aus der Ferne (Oxford) kamen per i-chat immer wieder entscheidende Tips!

Simon Webster, Postdoc aus Oxford und unser Sprach-Sheriff. Gemeinsam haben wir die Messungen der polarisierten Photonen und der Verschränkung durchgeführt. Für seine Unterstützung beim Messen, Aufbauen, Auswerten und Paperschreiben danke ich ihm herzlich!

Holger Specht, meinem Muster-Diplomanden, danke ich für die tatkräftige Unterstützung bei der Umstellung der Photonenpistole auf Rubidium 87 und für seine Fähigkeiten als Simulator. Nach der Diplomarbeit hat er zwar ins QGate-Labor gewechselt, aber als Büromitbewohner ist er mir denoch treu geblieben und hat immer ein offenes Ohr für mich.

Markus Hennrich und **Thomas Legero**, meinen Vogängern an der Photonenpistole, denen es zu verdanken ist, dass das Experiment so wenig störanfällig ist. Thomas Legero danke ich insbesondere dafür, dass er mir alle Kniffe der Apparatur beigebracht hat, und für die gute Zusammenarbeit während der Experimente zur Zwei-Photonen-Interferenz.

Patrizia Krok, Diplomandin an der Photonenpistole und während dieser Zeit meine Bürogenossin. Sie ist die Einzige, die ich wenigstens zeitweise von meinem Lieblingssport überzeugen konnte.

Clarice Aiello, Stagiaire an der Photonenpistole, mit der ich zusammen einige Wochen im kalten Labor verbracht habe um die Messzeiten an der Photonenpistole zu verkürzen. Zuletzt wurde es den Atomen in der MOT heißer - Clarice aber umso kälter.

David Moehring, unserem Postdoc aus Michigan, danke ich für inspirierende Diskussionen über ungeladene Ionen, Verschränkung und den ganzen Rest. Dank seiner Bereitschaft diese Arbeit Korrektur zu lesen, bin ich vom Oxfordenglisch zum amerikanischen Englisch konvertiert.

Bernhard Weber und **Peter Maunz**, die sich netterweise um die Implementierung der neuen Messkarte bei uns Pistoleros gekümmert haben. Bernhard Weber war außerdem stets zur Stelle, wenn Maestro mal nicht so wollte wie wir.

Der neuen Pistolero Generation, Jörg Bochmann, Martin Mücke, Christoph Erbel und Gunnar Langfahl danke ich für das reibungslose Zusammenleben im Labor und zusammen mit den **QGates** für diskussionsreiche und vergnügliche Gruppensitzungen.

Unseren Technikern **Josef Bayerl, Helmut Stehbeck, Franz Denk** und unserem Elektroniker **Tom Wiesmaier** für die tolle Unterstützung in all den Jahren der Photonenpistole. Wenn Umbauten anstanden, konnte man sicher sein, dass sie wie von Geisterhand bereits am frühen Morgen erledigt wurden.

Odette Gori danke ich für, ihr Organisationstalent und für den direkten Draht zum Chef.

Allen Mitgliedern der Rempe-Gruppe danke ich für ein äußerst kollegiales Klima in der Gruppe. Skitage und sonstige Ausflüge, Grillabende und Kickerturniere waren immer ein schönes Erlebnis.

Meinen Freunden hier und anderswo, die für Ablenkung vom Laboralltag gesorgt haben. Mit meinen Unterwasserfreunden konnte ich regelrecht aus der Physik abtauchen.

Meiner Familie, die mich während der ganzen Studien- und Promotionzeit in jeder Hinsicht unterstützt hat. Besonders freut mich, dass sie so großen Anteil an meiner Arbeit nehmen und sogar mein Labor besucht haben, um die Faszination einer Wolke kalter Atome mit eigenen Augen zu sehen.

Danke **Thomas**!